An Analysis of the Centrally Produced $\pi^+\pi^-$ System at 450 GeV/c

Keith Laurence Norman

A thesis submitted to the Faculty of Science of the University of Birmingham for the degree of Doctor of Philosophy

Particle Physics Group,
School of Physics and Space Research,
Faculty of Science,
The University of Birmingham

September, 1996.

Synopsis

The WA91 Experiment is designed to study final states formed in the reaction $\mathrm{pp}\longrightarrow\mathrm{p}_f X^0 \mathrm{p}_s$, where the subscripts f and s refer to the fastest and slowest particles in the laboratory frame respectively, and X^0 refers to the central system. Reactions of this type are predicted to be good sources of non-$\mathrm{q\overline{q}}$ final states, such as glueballs.

This thesis presents results on the $X^0 \longrightarrow \pi^+\pi^-$ channel, taken during the 1992 and 1994 experimental runs. A fit to the $\pi^+\pi^-$ mass spectrum has been performed, and it has been found necessary to include a contribution from a state with a mass of ~ 1500 MeV/c^2 and a width of ~ 200 MeV/c^2. A new parameterization of the $\pi^+\pi^-$ angular distribution has been developed, and the partial waves contributing to the $\pi^+\pi^-$ channel have been extracted. A fit to the S-wave using the same formalism as that used for the mass spectrum also finds it necessary to include a state at around 1500 MeV/c^2.

A novel effect is observed if the data are classified by the azimuthal angle between the outgoing protons. Significantly larger signal-to-background ratios of standard $\mathrm{q\overline{q}}$ states are observed for events with a "back-to-back" configuration of the outgoing proton p_T's. This effect is not due to the trigger or experimental acceptance, and suggests that the exchange vertices do not factorize.

Dedicated to the memory of my father,

P.H.R. Norman,

who may not have understood much of this work,

but who would have been proud all the same.

Contents

List of Figures

List of Tables

Acknowledgements

I would like to extend my thanks to PPARC (formerly SERC) for providing financial support for the present work, and Professors George Morrison and John Dowell for the use of research facilities at the University of Birmingham. Special appreciation must be given to the staff and students of the Particle Physics Group, particularly to my supervisor, Dr Orlando Villalobos Baillie, and the WA91 spokesperson, Dr Andrew Kirk. I am indebted to Professor John Kinson, the head of the Omega group in Birmingham, Dr David Evans, and Dr Frank Votruba for some most illuminating conversations. Thanks must also be given to Dr Noel Carney and Bernard French at CERN, and Dr Lawrie Lowe for help with computing problems.

I have received much guidance and friendship from my fellow students, Chris Dodenhoff, Steve Clewer, Jim Clayton, Stuart Robertson, Andy Bayes, Rob Akers, Stuart Clowes, Paul Davies, Paul Newman, Mark Pearce, Ian Brawn, Tim Nicholls, Dave Rigby, Vicki Hudgson, Jim Edwards, Ollie Cooke, Mark Venables, James Bloomer, Kirstee Hewitt, Steve Oglesby, Brian Earl, Adam Connors and Paul Thompson. Gratitude is also due to Drs Lee West, Dave Rees and Steve Hillier.

Special thanks are due to my parents, brother and sister, and to my wife, Kate, all of whom have given me much support (and sleeping space).

K.L.N.

Chapter 1

Introduction

In this thesis, the light meson spectrum will be considered, in particular the $J^{PC} = 0^{++}$ (scalar) sector. It will be shown how it is possible that the lightest glueball state may have been observed in several "glue-rich" reaction mechanisms. A study of the centrally produced $\pi^+\pi^-$ system from the 1992 run of the WA91 experiment shall then be presented, and compared with a similar data set from the WA76 experiment, who found evidence for a state with the characteristics of the lightest scalar glueball. A description of the data selection will be given, and a fit to the WA91 $\pi^+\pi^-$ mass spectrum will be presented. It shall then be shown how a new parameterization of the angular distribution has been developed, and this is used to perform a fit. An analysis of the $\pi^+\pi^-$ system from the 1994 run of the WA91 experiment will be given, where an unexpected new effect has been observed that may suggest vertex factorization breaking. Finally, relevant conclusions will be drawn, and possibilities for further studies discussed.

1.1 The Structure of Matter

According to the Standard Model, all hadronic matter is composed of quarks (q) and gluons (g). Direct experimental evidence for the existence of quarks and gluons comes from the analysis of deep inelastic scattering and studies of jet production [1]. The quantum field theory that describes the interactions of quarks and gluons is Quantum Chromodynamics (QCD) [2]. QCD is expressed mathematically as a non-abelian gauge theory, which we interpret physically as the prediction that the carriers of the strong force (*i.e.*, the gluons) are self-interacting. This implies that it should be possible to observe experimentally new forms of matter which consist either entirely of valence gluons (*i.e.*, gluons which determine the physical characteristics of the state in question), or of combinations of valence gluons and quarks. These are known respectively as "glueballs" and "hybrid states". However, although at present there are candidate glueball and hybrid states, there is no unambiguous evidence that such states have been correctly classified.

1.2 The Colour Force

QCD describes all hadrons as consisting of a mixture of valence quarks (which determine most of the observable properties of the hadron), gluons and a fraction of "sea" quark-antiquark ($q\overline{q}$) pairs. It is observed that the valence quark combinations for hadrons allow them to be classified as being either *mesons* (*e.g.*, π, ρ), consisting of valence $q\overline{q}$ pairs, or *baryons* (*e.g.*, p, n, Λ^0) consisting of 3 valence quarks and no antiquarks [3]. The quantum mechanics of such bound systems leads to discrete energy level spectra corresponding to different modes of excitations, rotations and vibrations of the quarks. Hadrons can be further classified by their spin, J, parity, P, and charge conjugation, C, into *multiplets*, which are described by group theory. Some of the established light meson multiplets are shown in table 1.1, grouped by their isotopic spin, I [4].

Table 1.1: The light meson multiplets.

J^{PC}	$I = 1$	$I = 0$	$I = 0$	$I = \frac{1}{2}$
0^{-+}	π	η	η'	K
1^{--}	ρ	ω	ϕ	$K^*(892)$
1^{+-}	$b_1(1235)$	$h_1(1170)$	$h_1(1380)$	K_{1B}
0^{++}	$a_0(980)$	$f_0(1300)$	$f_0(980)$	$K_0^*(1430)$
1^{++}	$a_1(1260)$	$f_1(1285)$	$f_1(1510)$	K_{1A}
2^{++}	$a_2(1320)$	$f_2(1270)$	$f_2'(1525)$	$K_2^*(1430)$

Radial excitations of a state correspond to other states (at higher masses) with the same J^{PC} .

Quarks carry a property analogous to electric charge known as *colour charge.* As the photon mediates the electromagnetic force between electrically charged particles, so the gluon gives rise to strong (colour) interactions between colour charged particles. However, note that although the photon itself is electrically neutral, the gluon is not colour neutral, that is to say, *the gluon possesses its own colour charge.* Hence gluons can interact with themselves, leading to the possibility of forming gluonic bound states. It is hypothesised that colour is confined (see [3], in particular appendix J), so that gluonic states are overall colour singlets, *i.e.*, they remain colourless under SU(3)(colour) transformations. Thus gluonic states have no net colour, even though the gluons themselves carry colour.

Local gauge invariance (see, for example, [2]) requires that the gluon mass is identically zero. This is not required for quarks and antiquarks, but in the framework of QCD it is assumed that up (u) and down (d) quarks would have negligible mass if it were possible to observe them in a deconfined state. While confined in hadrons, u and d quarks behave as though they have a mass of approximately 300–400 MeV, giving rise to mesonic ground states of ~700 MeV and baryonic ground states of ~1 GeV. This so-called constituent quark mass can be regarded as the effect of the quark being surrounded by a cloud of virtual quarks, antiquarks and gluons. In the same way, it is expected that gluons confined in a bound state such as a glueball would also acquire a constituent mass, producing a massive gluonic state.

1.3 Further mesonic states

In addition to glueballs, QCD also predicts the existence of other mesonic states which are not composed entirely of valence quark-antiquark pairs [5]. *Hybrid states* consist of valence quarks, antiquarks and a number of valence gluons. *4–quark states* are bound states of $q\overline{q}q\overline{q}$. Also, it may be possible to observe loosely bound $K^*\overline{K}$ *molecules*, strongly coupled to final states containing strange quarks.

1.4 Theoretical mass predictions

In the last few years there has been enormous progress in the prediction of the masses of gluonic states. The current predictions are based on lattice gauge theory. This attempts to model the hadron spectrum by linking lines of flux across a 4-dimensional lattice with periodic boundary conditions (but no edges). Typical lattice sizes are 24^4 elements, with the result that $\sim 10^7$-dimensional integrals have to be performed. Glueballs are modelled on the lattice as closed flux loops. The two most recent predictions from the IBM Collaboration [6] and the UKQCD Collaboration [7] of the lowest lying glueball states are

$$\begin{array}{lll}
0^{++} & 1740 \pm 70 \text{ MeV}/c^2 & \text{IBM} \\
 & 1550 \pm 50 \text{ MeV}/c^2 & \text{UKQCD} \\
 & & \\
2^{++} & 2270 \pm 100 \text{ MeV}/c^2 & \text{UKQCD,}
\end{array}$$

with widths in the region of 100–150 MeV/c^2.

Although the two predictions for the 0^{++} state are not identical, it should be borne in mind that as little as 10 years ago, predictions had errors an order of magnitude greater than those given here. Both groups employ the *quenched approximation* in their calculations. This approximation means that there is no coupling introduced between the primitive glueball state and quarks. However, as may be seen from table 1.1, normal $q\overline{q}$ states are observed in the $J^{PC} = 0^{++}$ $I = 0$ sector which have masses comparable to the predictions for the lowest lying gluonic states, and hence it might be expected that there is some mixing between the $q\overline{q}$ and glueball states in this sector. Although this may seem problematic, we shall see that the predictions may in fact support the experimental results.

1.5 Observable characteristics of glueball states

In this section, the possible ways of observing non-$q\overline{q}$ states experimentally are considered.

Up to a few years ago, most hadron spectroscopy had been performed using peripheral reactions where the interactions are dominated by quarks, and it may be that these channels are not sufficiently "glue rich" to produce gluonium states. In glueball searches it is thought to be important to analyse channels where the converse is the case. A resonance which appears in a reaction which is supposed to be glue rich, but is not observed (or at least is suppressed) in a reaction which is supposed to be dominated by other processes, would be a good glueball candidate. Using reactions of this type, new states have been discovered which do not fit well into the standard $q\overline{q}$ multiplets (some of which will be discussed in chapter 2, but see also [8]).

Figure 1.1 summarizes several reactions which are thought to be useful probes of gluon rich channels and where experimental observations have been made. The general properties of these reactions are discussed below.

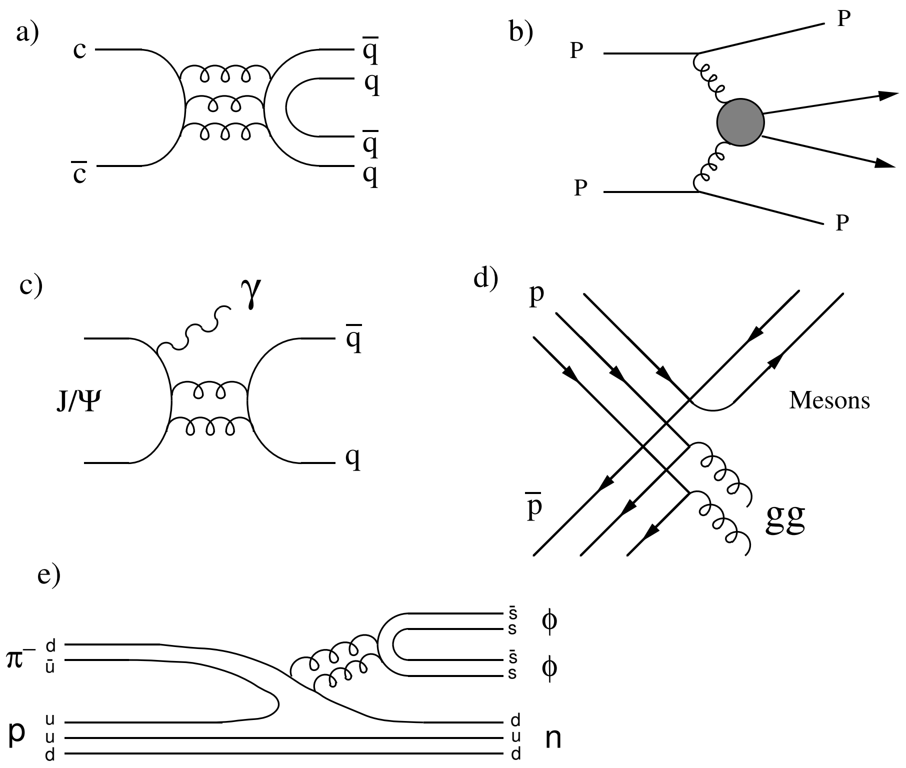

Figure 1.1: Experimental glue-rich channels.

- J/ψ decay, shown in figure 1.1 a,c has well defined initial state properties and a relatively limited number of final states, so they do not suffer from large backgrounds. The radiative decay mode (figure 1.1c) is a hard gluon channel, and hence may couple strongly to glueballs with positive C-parity (to conserve C).

- Double Pomeron Exchange (DPE) (figure 1.1b). The Pomeron (see section 1.6.1) is considered to be responsible for the large cross sections of some diffractive reactions. It is thought to be a multi-gluon state, so that Pomeron–Pomeron scattering could be a good source of gluonic final states [9]. In the centre of mass system, the exchange particles are required to leave the colliding particles almost undisturbed, producing a central system which is essentially at rest. This gives a good signal-to-background ratio, and is the process considered in the CERN WA91 experiment, where several interesting signals have been seen. This will be discussed further in chapter 2.

- Special hadronic reactions like that shown in figure 1.1 e, which are Zweig suppressed [10].

- Proton–antiproton annihilation (figure 1.1 d) is a possible gluon source which may lead to final state gluonic objects. This is the process used in the Crystal Barrel Experiment at LEAR [11], which has recently found evidence for states beyond the standard $q\overline{q}$ model. (See chapter 2.)

Bearing the above discussion in mind, we now proceed to consider the characteristics of glueballs that may make them observable in experiment. Of importance here is the property of normal $q\overline{q}$ states, discussed briefly in section 1.2, whereby hadrons can be grouped into multiplets of J^{PC} values. Simple considerations [3] give

$$P=-(-1)^{L}, \qquad C=(-1)^{L+S},$$

for a $q\overline{q}$ state, where P and C represent the parity and charge conjugation operators respectively, and L and S are the orbital angular momentum and spin quantum numbers of the $q\overline{q}$ system. For spin-$\frac{1}{2}$ $q\overline{q}$ pairs, some values of J^{PC} , for example 1^{-+}, are clearly disallowed by these relationships. This is not the case for a combination of spin-1 gluons. Thus a good search for non-$q\overline{q}$ states is to look for "oddball" states with exotic J^{PC} values.

Furthermore, one can look experimentally for new states which appear to fit into already completed nonets. This is a more problematic approach, since we must be sure that a new state has a mass low enough for it not to be a member of a radial excitation of that nonet. The lowest lying nonets are well established [4], but the higher mass nonets are more difficult to classify, since radial excitations become increasingly important at high mass. Unfortunately, the lowest mass glueball states (particularly the lowest tensor) are expected to be present in this region, where the current multiplet grouping is less certain, and evidence suggesting that new states should be regarded as glueball candidates because they do not fit well into the high mass multiplets is less compelling.

Since gluons carry zero electric charge, they do not couple directly to photons. For the reaction

$$\mathrm{gg} \rightarrow \gamma\gamma$$

to proceed, the gluons must first convert to $q\overline{q}$ pairs, as shown in figure 1.2. This reaction requires additional coupling vertices, and is hence heavily suppressed. Applying time reversal symmetry, we see that the reaction

$$\gamma\gamma \rightarrow \mathrm{gg}$$

is also strongly suppressed, and thus one should not expect to see gluonic resonances produced in $\gamma\gamma$ collisions. An observation of a glueball candidate in such a process would be strong evidence of a quark content, which implies the candidate is either a standard $q\overline{q}$ state, or possibly a hybrid.

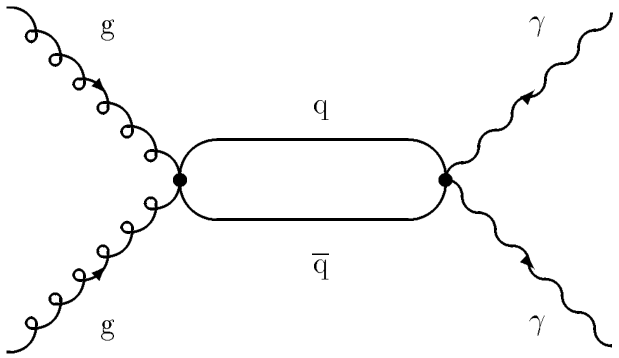

Figure 1.2: Coupling of gluons to photons.

However, the coupling of gluons to quarks should in principle be essentially flavour independent, that is a glueball state should have equal branching ratios to any combination of flavour (up to phase space factors). Compare this with the case of a standard $q\overline{q}$ state. The typical example is the $\phi(1020)/\omega(783)$ system. Experimentally [4], it is found that

$$\begin{array}{llll} \phi(1020) & \longrightarrow & \mathrm{K}\overline{\mathrm{K}} & 84\% \\ & \longrightarrow & \pi\pi\pi & 15\% \\ & & & \\ \omega(783) & \longrightarrow & \pi\pi\pi & 90\% \\ & \longrightarrow & \pi\pi,\ \pi\gamma & 10\% \end{array}$$

Although there is more phase space for the three pion decay of the $\phi(1020)$, the $\mathrm{K}\overline{\mathrm{K}}$ channel is clearly dominant, but the same channel is absent from the $\omega(783)$ decay. The reason for this is the quark content of the $\phi(1020)$ and $\omega(783)$. In this nonet, the mixing between $u\overline{u} + d\overline{d}$ and $s\overline{s}$ is almost ideal, which is to say that the $\phi(1020)$ is close to pure $s\overline{s}$, while the $\omega(783)$ is essentially $u\overline{u} + d\overline{d}$. Thus the $\phi(1020)$ couples very strongly to states with a large strange content, and only weakly to final states without a strange content, with the converse for the $\omega(783)$. A glueball would not be expected to show this flavour dependence. There is, however, a *caveat* to this assertion, and that is that mixing between the primitive glueball and the $q\overline{q}$ states may affect the coupling to some channels, as will be discussed in chapter 2.

To end this section, a summary of possible experimental signatures of glueball states is given below.

- Production in glue-rich processes.
- J^{PC} values not allowed for a standard $q\overline{q}$ state, *e.g.*, 1^{-+}.
- Extra states in already completed nonets.
- Suppressed coupling to photons.
- Flavour independent coupling to quarks (but see chapter 2).

1.6 Pomeron Scattering

1.6.1 The Nature of the Pomeron

At low momentum transfers, perturbative QCD becomes unworkable. Instead, we may appeal to Regge Theory [12], which describes scattering processes in terms of trajectories, $\alpha(t)$, corresponding to the exchange of virtual mesons. Traditionally, this has been applied to peripheral processes, but it may be expected that it is also applicable to central production. At low energies, Regge Theory has had some phenomenological success in predicting observed cross sections for a variety of reactions. However, the situation becomes problematic at high energies, where it is observed that total and elastic cross sections become essentially constant (or rising very slowly). This is shown in figure 1.3 for pp and $p\overline{p}$ interactions. In Regge Theory, total cross sections are expected to behave as

$$\sigma_T \sim s^{\alpha(0)-1},$$

where $\alpha(0)$ represents the dominant elastic Regge Trajectory at high energies. The approximate independence of s of total cross sections at high s therefore implies

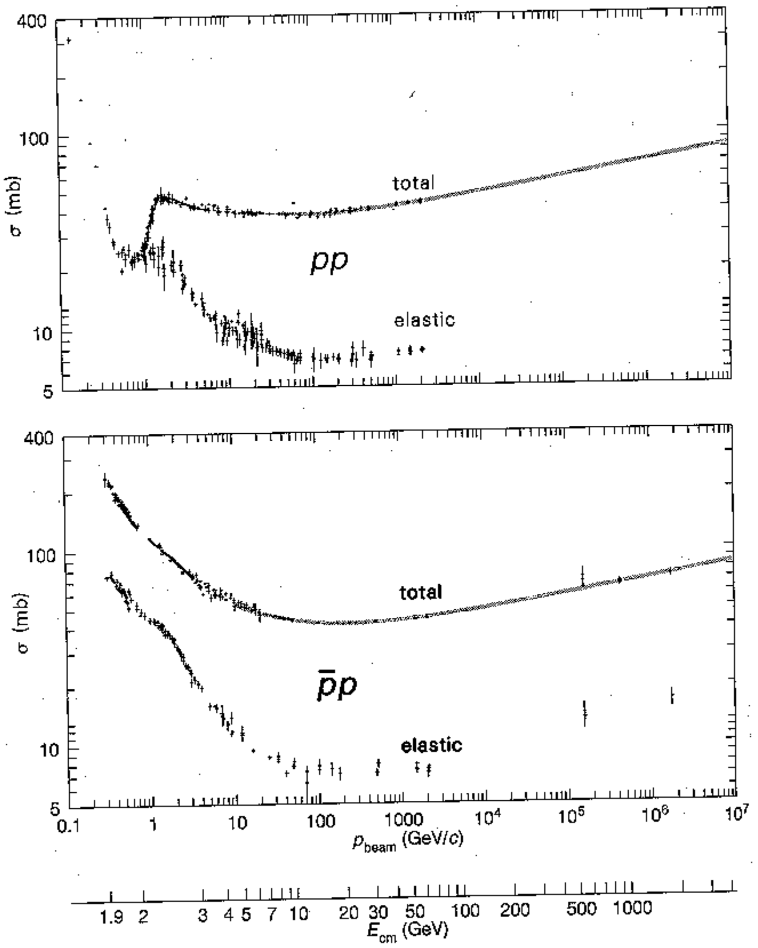

Figure 1.3: Hadronic cross sections as functions of beam momentum and energy for pp and p$\overline{\mathrm{p}}$ (from [4]).

the existence of a trajectory with $\alpha(0) \sim 1$ (all known meson trajectories have $\alpha(0) \lesssim 0.5$). The exchange particle is termed the Pomeron. As may be seen from figure 1.3, the behaviour of cross section as a function of $\sqrt{s}$ is approximately independent of hadronic flavour at high $\sqrt{s}$, and so it may be supposed that the Pomeron corresponds to gluon exchange [13].

Donnachie and Landshoff [14] have fitted the $\sqrt{s}$ dependence of the total cross-section for pp and p$\overline{\text{p}}$ scattering from $\sim$ 5 GeV to $\sim$ 2000 GeV using a term to describe Pomeron exchange, and a second term to describe Reggeon exchange (where the Reggeon corresponds to trajectories with poles at the masses of known mesons). The results of this for the Pomeron trajectory give $\alpha(0) = 1.0808$.

Recently, some progress has been made on understanding how the phenomenological Pomeron fits into the framework of QCD. The observation of high p_T jets in diffractive p$\overline{\text{p}}$ interactions [15] is suggestive of a partonic structure. H1 and ZEUS at the HERA collider have recently presented results [16], [17] which show evidence for a flux of colourless objects associated with the proton. When the virtual photon in Deep Inelastic Scattering (DIS) interacts with these colourless states, large "rapidity gap" events are observed, that is events where there is no hadronic energy in a large region of pseudo-rapidity close to the final state proton or its remnant. H1 find that the states responsible for the rapidity gap events in DIS have $\alpha(0) = 1.10 \pm 0.03 \pm 0.04$, while ZEUS find $\alpha(0) = 1.15 \pm 0.04^{+0.04}_{-0.07}$. These results are consistent with the expected Pomeron trajectory. Assuming, then, that the rapidity gap events can be ascribed to Pomeron exchange, H1 and ZEUS have studied the partonic nature of the Pomeron. They define a structure function for the Pomeron, $\tilde{F}_2^D$, by

$$\tilde{F}_2^D = \int F_2^D(\beta, Q^2, x)dx,$$

where $Q^2 = -q^2$, $x = Q^2/2p \cdot q$, representing the proportion of the proton's momentum carried by the Pomeron, β is the fraction of the Pomeron's momentum carried by the struck quark, and the integration is performed over the entire range of x

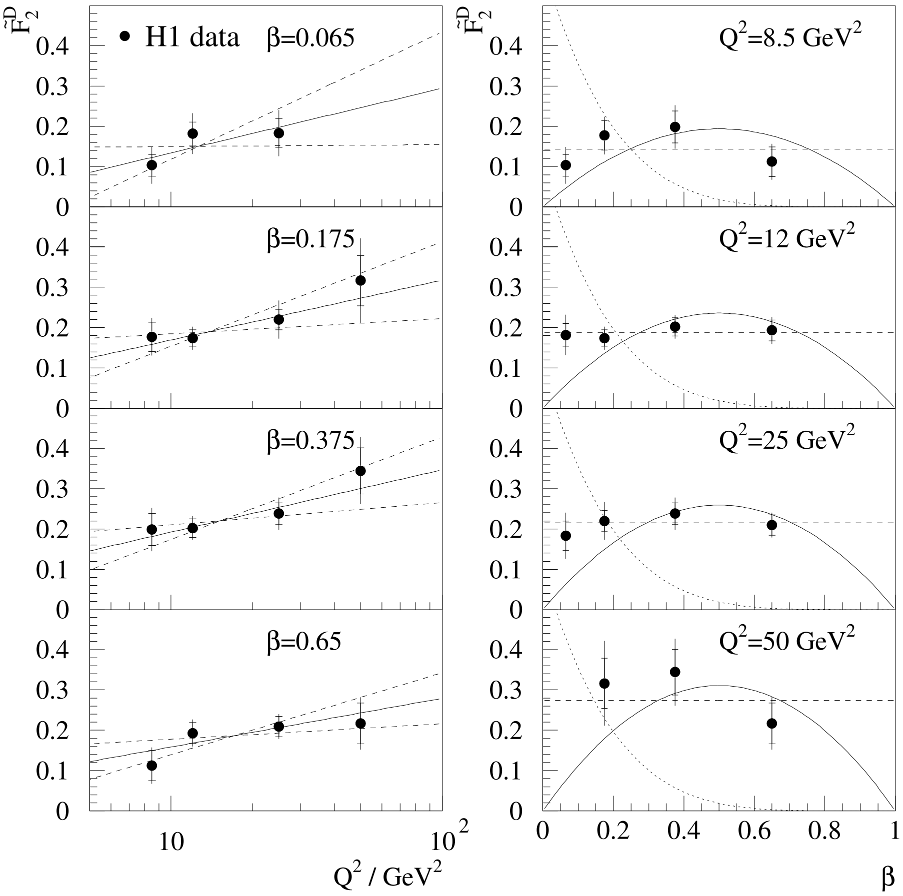

Figure 1.4: Measurements of $\tilde{F}_2^D$. Left : as a function of Q^2 at fixed β with the best fit (solid line) and the upper and lower limits (dashed lines) to a logarithmic slope. Right : as a function of β at fixed Q^2 with assumed dependence $\beta(1-\beta)$ (solid curve), constant β (dashed curve) and $(1-\beta)^5$ (dotted curve) (from T. Ahmed et al. [18]).

measured. The H1 results are shown in figure 1.4. To first order, $\tilde{F}_2^D$ shows Q^2 scale invariance, suggesting a partonic structure. Deviations from this are accountable to $\log Q^2$ scaling violations. The β dependence at fixed Q^2 is inconsistent with the form $(1-\beta)^5$ expected for a fully evolved meson [19], but can be described by either a flat or hard $(\beta(1-\beta))$ dependence. This is consistent with a pomeron valence structure of a gluon pair evolving a parton sea at low β. However, the fact that $\tilde{F}_2^D$ rises with increasing Q^2 for all β may be explained in terms of a gluon dominated structure function. Fits using standard "next-to-leading-order" QCD evolution find that the data are well described with a hard ($\beta \approx 1$) gluon dominated structure, although the confidence level of this description is currently limited by the experimental accuracy of the results.

1.6.2 Double Pomeron Exchange

The reaction

$$\mathrm{pp} \longrightarrow \mathrm{p}_f(X^0)\mathrm{p}_s,$$

(figure 1.5) can proceed by a number of different exchange mechanisms. In general, there will be contributions from Reggeon-Reggeon, Reggeon-Pomeron and Pomeron-Pomeron. However, theoretical considerations [20] suggest that these mechanisms have different energy dependences, and specifically

$$\begin{aligned} \sigma_{RR} &\sim s^{-2}, \\ \sigma_{RP} &\sim s^{-1}, \\ \sigma_{PP} &\sim c, \end{aligned}$$

where σ_{RR}, σ_{RP} and σ_{PP} represent the cross sections for Reggeon-Reggeon, Reggeon-Pomeron and Pomeron-Pomeron exchange respectively and c is a constant. Furthermore, for fixed Feynman x, x_F, defined as $\frac{p_L}{p_{L_{max}}}$, where $p_{L_{max}}$ is the maximum longitudinal momentum available for a particle, it may be shown [20] that the DPE

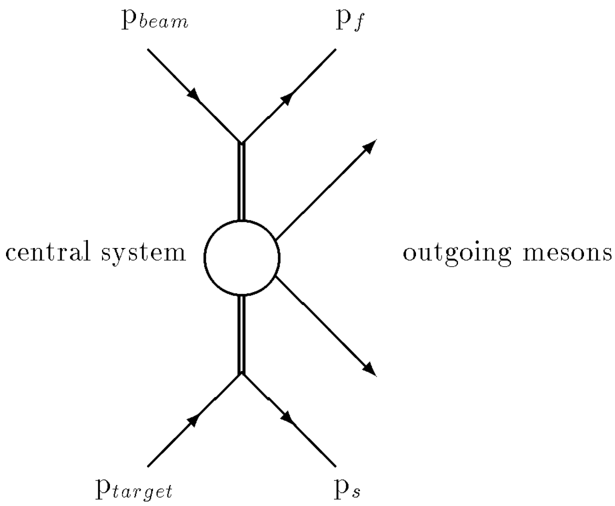

Figure 1.5: The central production mechanism in the centre-of-mass frame.

signal-to-background ratio varies as $\sim e^{-\alpha|t|}$, where t represents the sum of the 4-momentum transfer at the two vertices, and hence more DPE is expected at low $|t|$.

Isospin conservation implies that DPE cannot produce isospin 1 states. Hence a decrease in the signal-to-background for isospin 1 states is a good indication of DPE becoming important.

The WA76 collaboration [21] took data on the reaction

$$\mathrm{pp} \longrightarrow \mathrm{p}_f \pi^+ \pi^- \mathrm{p}_s$$

at beam momenta of 85 GeV/c and 300 GeV/c, corresponding to centre-of-mass energies of 12.7 GeV and 23.8 GeV. The $\pi^+\pi^-$ mass spectra obtained by WA76 at the two energies are shown in figure 1.6. Clear $\rho(770)$ and $f_2(1270)$ signals are observed in the mass spectra; however the $\rho(770)$ signal in particular is substantially reduced in the higher energy data. Since the $\rho(770)$ is an isospin 1 object, it cannot be produced by DPE, and hence the decrease in the size of the $\rho(770)$ signal at high energy is an experimental indication that DPE becomes more important at high

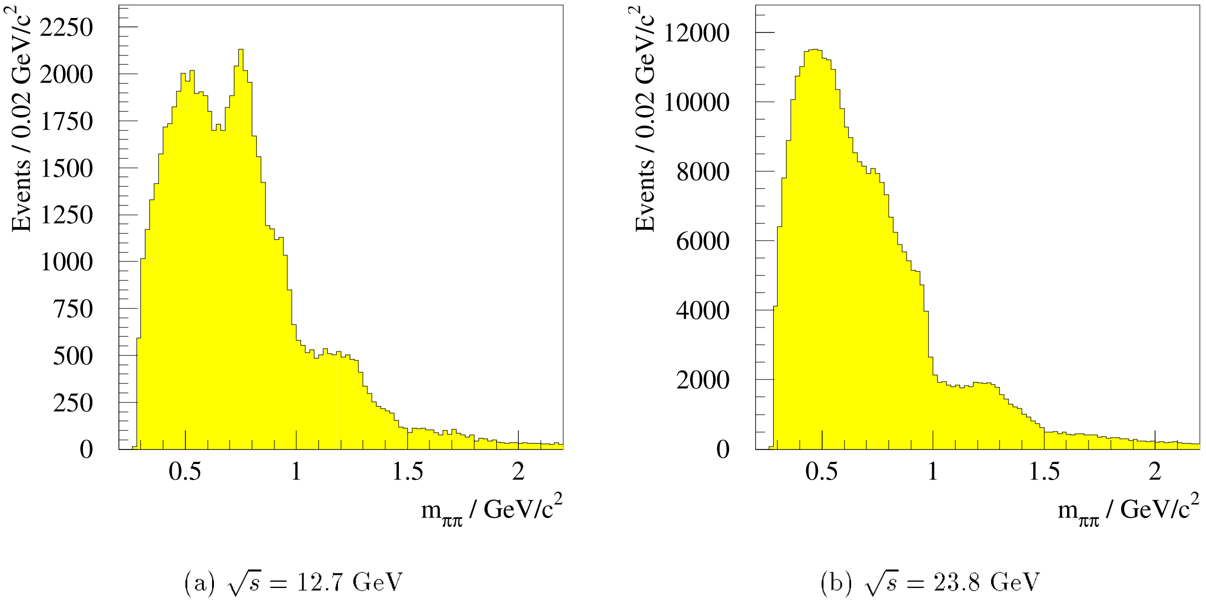

Figure 1.6: $\pi^+\pi^-$ mass spectra obtained by the WA76 Collaboration (from [22]).

energy compared with the Reggeon-Reggeon and Reggeon-Pomeron contributions.

A similar effect is observed if the WA76 data at either energy is divided into a sample with $|t| < 0.3$ GeV^2 and a sample with $|t| > 0.3$ GeV^2, confirming the prediction that DPE is dominant at low 4-momentum transfer. This effect will be shown for the WA91 1992 data sample in chapter 4.

Thus experiments designed to search for non-$q\overline{q}$ states in DPE should be optimised to take data at

- high energy,
- low 4-momentum transfer.

Chapter 2

The 0^{++} Sector

Recently, there has been considerable interest in the lowest lying scalar states. Although table 1.1 lists the established scalars from the Particle Data Group, the grouping is in fact far from certain. In this chapter, the members curently assigned to this nonet will be discussed, and experimental results showing the validity of these assignments will be given. Models which attempt to describe the nonet will be considered, and how this may predict that one of the members in particular is either an extra state or possibly a mixture of a primitive glueball and a standard $q\overline{q}$ state will be shown.

The members of the 0^{++} sector shown in table 1.1 are the $a_0(980)$, $f_0(1300)$, $f_0(980)$ and $K_0^*(1430)$. Pennington [23] asserts that the fact that there is only one K_0^* state below 1800 MeV/c^2 is a good indication that there is only one $q\overline{q}$ multiplet in this mass region. The $K_0^*(1430)$ is observed cleanly by the LASS collaboration [24] in K^-p interactions, decaying to $K\pi$ with a total width of about 300 MeV/c^2. The $a_0(980)$ decaying to $\eta\pi$ is observed by the WA76 Collaboration [25] and the Crystal Barrel Collaboration [26] with a width of around 70 MeV/c^2. Although this width is narrow compared with the $K_0^*(1430)$, it must be remembered that the $a_0(980)$ is essentially at $K\overline{K}$ threshold, and coupling to this channel may affect the width at resonance.

The f_0 states are more problematic. In fact, the 1994 edition of the Review of Particle Properties lists three f_0 states, the $f_0(980)$, the $f_0(1300)$ and the $f_0(1590)$. However, the situation is rather more complicated than this, with several other candidate f_0 states observed around this mass region. The $f_0(980)$ is observed in $\pi\pi$ scattering experiments and in central production, and like the $a_0(980)$ has a narrow width of about 50 MeV/c^2. Weinstein and Isgur [27] have proposed that the $a_0(980)$ and $f_0(980)$ are $K\overline{K}$ molecules, based on their coupling strengths to $K\overline{K}$ and their small $\gamma\gamma$ partial widths.

The status of the $f_0(1300)$ is rather unclear. Recent Crystal Barrel results on the $\pi^0\pi^0\pi^0$, $\eta\eta\pi^0$ and $5\pi^0$ channels in proton-antiproton annihilation find a state at around 1370 MeV/c^2 with a width of about 350 MeV/c^2 [28]. In multi-channel fits to $\pi\pi \longrightarrow \pi\pi$, $\pi\pi \longrightarrow KK$ and central production, Morgan and Pennington [29] add an elastic background term in the 1300 MeV/c^2 region which may be interpreted as a very wide ($\sim$ 700 MeV/c^2) resonant state. However, Bugg, Sarantsev and Zou [30] claim that the f_0 state at this mass is in fact rather inelastic. It is not clear with present data how many states are present in this region, and in particular whether the broad state required in multi-channel fits at around 1300 MeV/c^2 is the same state as the $f_0(1370)$.

2.1 The 1500 MeV/c^2 Mass Region

Most of the recent interest in the scalar nonet has been centred on the 1500 MeV/c^2 mass region. The Crystal Barrel Collaboration report a state with a mass of 1509 ± 10 MeV/c^2 and a width of 116 ± 17 MeV/c^2 decaying to $\pi^0\pi^0$, $\eta\eta$ and $\eta\eta'$ in proton-antiproton annihilation [31], [32], [33], [34], and evidence for the same state in $4\pi^0$ [35]. The Dalitz Plot for $p\overline{p} \longrightarrow \pi^0\pi^0\pi^0$ [31] is shown in figure 2.1. In this figure, the area of increased plot density labelled A corresponds to the 1500 MeV/c^2 mass region (B is the result of interference effects in the cross channel).

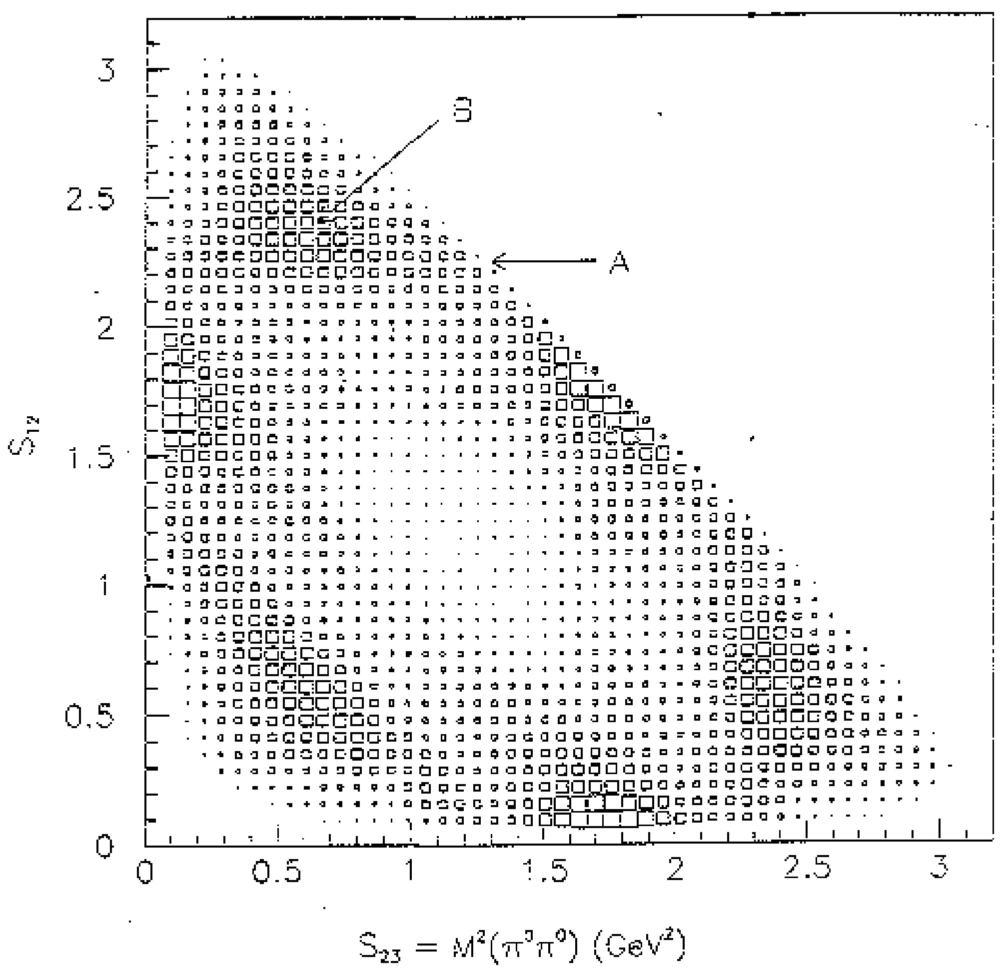

Figure 2.1: Dalitz Plot $m^2_{\pi^0\pi^0}$ vs $m^2_{\pi^0\pi^0}$ (from [31]).

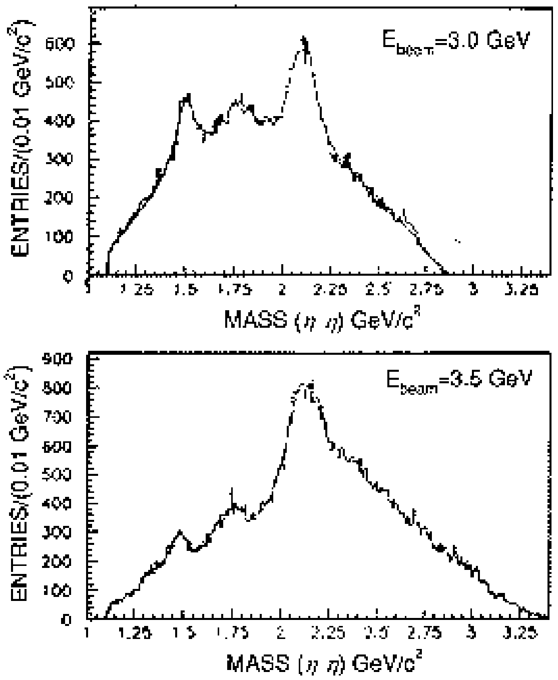

Figure 2.2: E760 $\eta\eta$ mass spectra at 3.0 GeV and 3.5 GeV (from [36]).

E760 [36] report a resonant state decaying to $\eta\eta$ with mass and width around 1488 MeV/c^2 and 148 MeV/c^2 respectively, also in $\mathrm{p\overline{p}}$ annihilation. The $\eta\eta$ mass spectra at beam energies of 3.0 GeV and 3.5 GeV are shown in figure 2.2. A partial wave analysis of this reaction is in preparation, but E760 claim that only even spin particles can be seen in their $\eta\eta$ data.

A recent reanalysis by Bugg *et al.* [37] of radiative J/ψ decay to $\gamma 4\pi$ using data taken by the Mark III Collaboration and by the DM2 Collaboration finds that it is possible to describe the data with a scalar state of mass $\sim$ 1500 MeV/c^2 and width $\sim$ 100 MeV/c^2, which was previously misidentified as a 0^{-+} state. The mass spectrum together with a fit to the scalar contribution is shown in figure 2.3.

The GAMS Collaboration [38] have observed a state which they call the G(1590), with mass 1592 ± 25 MeV/c^2 and width 210 ± 40 MeV/c^2 decaying to $\eta\eta$ in $\pi^-\mathrm{p} \longrightarrow \eta\eta\mathrm{n}$, with a similar peak in $\eta'\eta$. A partial wave analysis of the $\eta\eta$ channel at a

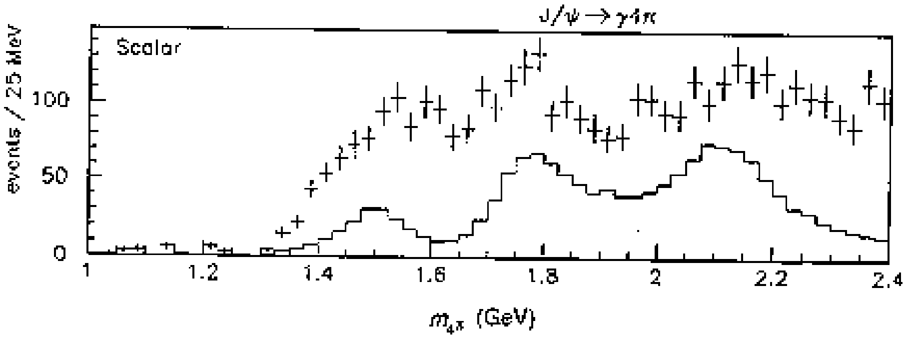

Figure 2.3: The $\gamma 4\pi$ mass spectrum, together with a fit to the scalar contribution (from [37]).

beam momentum of 100 GeV/c produces the S-wave spectrum shown in figure 2.4. The peak at around 1600 MeV/c^2 labelled G is clear, together with a peak at 1300 MeV/c^2 labelled ε, which the GAMS Collaboration identify with the $f_0(1300)$. Similar results are obtained at a beam momentum of 230 GeV/c. Furthermore, GAMS see the same signal in the central production reaction $\pi^- p \longrightarrow \pi^-(X^0)p$ at a beam momentum of 300 GeV/c in the $\eta\eta$ mass spectrum [40]. In the charge exchange reactions, GAMS quote

$$\frac{\sigma(\pi^- p \longrightarrow G(1590)n)}{\sigma(\pi^- p \longrightarrow f_2(1270)n)} \sim \frac{1}{25}$$

for beam momenta of both 40 GeV/c and 100 GeV/c. For the central collisions, GAMS give

$$\frac{\sigma(\pi^- p \longrightarrow G(1590)\pi^- p)}{\sigma(\pi^- p \longrightarrow f_2(1270)\pi^- p)} \sim 10$$

for a beam momentum of 300 GeV/c. [39] claims that the G(1590) is not seen in 40 GeV/c data for central collisions, suggesting that it is formed by DPE.

The WA76 collaboration [21] reported the observation of two previously unobserved states, the X(1450) and the X(1900), in the $\pi^+\pi^-\pi^+\pi^-$ channel of

$$pp \longrightarrow p_f(X^0)p_s$$

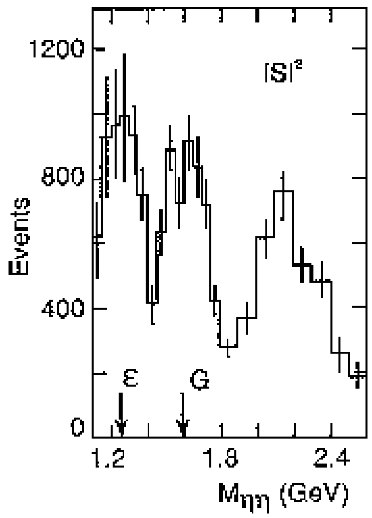

Figure 2.4: GAMS S-wave $\eta\eta$ mass spectrum (from [39]).

at 300 GeV/c. Neither state was observed in the 85 GeV/c data of the same experiment. The increase in cross section with incident energy is again consistent with the formation of these states by DPE. The WA91 collaboration studied the same channel at 450 GeV/c and assigned the $\mathrm{J^{PC}}$ values 0^{++} to the X(1450) and 2^{++} to the X(1900), suggesting that the correct nomenclature for these states should be $\mathrm{f_0}(1450)$ and $\mathrm{f_2}(1900)$ [41]. The combined WA76 and WA91 4π mass spectrum is shown in figure 2.5 a. Figure 2.5 b shows the combined spectra with the requirement $|t| < 0.15$ GeV^2 at both exchange vertices. The mass spectra clearly show the $\mathrm{f_0}(1450)$ and $\mathrm{f_2}(1900)$ signals, together with an $\mathrm{f_1}(1285)$ signal. The WA91 Collaboration note that relative to the $\mathrm{f_1}(1285)$, the $\mathrm{f_0}(1450)$ and $\mathrm{f_2}(1900)$ were both produced predominantly at low $|t|$. The masses and widths were found to be 1445 ± 5 MeV/c^2 with width 65 ± 10 MeV/c^2, and 1918 ± 12 MeV/c^2 with width 390 ± 60 MeV/c^2 respectively. Furthermore, the WA76 collaboration [43] analysed the centrally produced $\pi^+\pi^-$ channel, where they found evidence for a further new state with a mass of 1472 ± 12 MeV/c^2 and a width of 195 ± 30 MeV/c^2. Although the state in $\pi^+\pi^-$ appears to be consistent with those so far discussed, the scalar state in $\pi^+\pi^-\pi^+\pi^-$ has too low a mass and too narrow a width to be consistent with

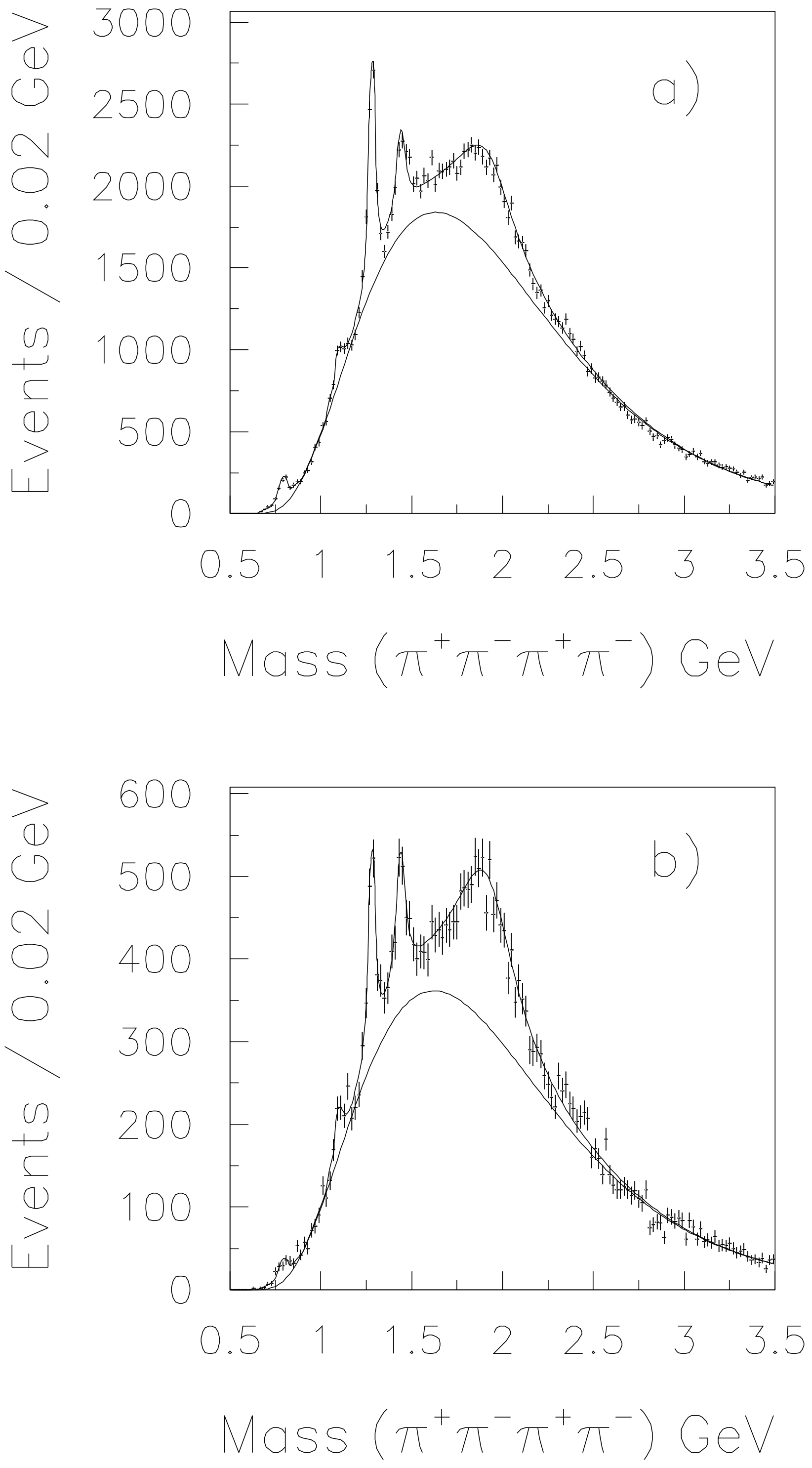

Figure 2.5: The combined 4π mass spectra for the WA76 and WA91 data together with fits using 3 Breit-Wigners and background. a) total spectrum, b) $|t| < 0.15$ GeV^2 at both exchange vertices. (from [42]).

the other observations. However, a further analysis [44] of the $\pi^+\pi^-\pi^+\pi^-$ data has shown that it may be possible to describe the scalar state as being an interference between two scalars parameterized as the 1370 MeV/c^2 and 1510 MeV/c^2 states observed by Crystal Barrel.

2.1.1 Summary of Experimental Results

There is evidence for a scalar state with mass 1500–1600 MeV/c^2 and width 100–200 MeV/c^2 in several channels of $\mathrm{p\overline{p}}$ annihilation, radiative J/ψ decay and central production, all of which are predicted to be possible sources of gluonic states. In order to further understand the properties of this state, it is important to consider its decay branching ratios, especially in light of the naïve expectation that gluonic states decay in a "flavour-blind" way.

2.1.2 Branching Ratios and Theoretical Expectations

Close and Amsler [45] note that the Crystal Barrel data and bubble chamber data [46] show peculiar decay rates for the $f_0(1500)$. They define the ratios

$$\begin{aligned} R_1 &= \frac{\gamma^2(f_0(1500) \longrightarrow \eta\eta)}{\gamma^2(f_0(1500) \longrightarrow \pi\pi)} \\ R_2 &= \frac{\gamma^2(f_0(1500) \longrightarrow \eta\eta')}{\gamma^2(f_0(1500) \longrightarrow \pi\pi)} \\ R_3 &= \frac{\gamma^2(f_0(1500) \longrightarrow \mathrm{K\overline{K}})}{\gamma^2(f_0(1500) \longrightarrow \pi\pi)} \end{aligned}$$

where γ^2 is essentially the matrix-element squared for the interaction, weighted by the sum over the various charge combinations, namely 4 for $\mathrm{K\overline{K}}$, 3 for $\pi\pi$, 2 for $\eta\eta'$ and 1 for $\eta\eta$. The experimental values of the ratios are found to be

$$\begin{aligned} R_1 &= 0.27 \pm 0.11 \\ R_2 &= 0.19 \pm 0.08 \\ R_3 &< 0.1 \text{ (90\% C.L.)}. \end{aligned}$$

The small decay rate for $K\overline{K}$ does not seem to suggest that the $f_0(1500)$ decays in a flavour independent way. However, Close and Amsler have developed a model of the scalar sector using perturbation theory. This model contains nine primitive $q\overline{q}$ states, and one primitive glueball gg state. In this model, the glueball state is allowed to mix into nearby $q\overline{q}$ states with the same quantum numbers. If the primitive glueball is $|G_0\rangle$, then the observed glueball state $|G\rangle$ is, using simple perturbation theory,

$$|G\rangle = |G_0\rangle + \xi \left(\frac{|u\overline{u} + d\overline{d}\rangle}{E(G_0) - E(d\overline{d})} + \frac{|s\overline{s}\rangle}{E(G_0) - E(s\overline{s})} \right),$$

with ξ being the mixing between the primitive glueball and the $q\overline{q}$ states. If flavour were a perfect symmetry, then $E(d\overline{d}) = E(s\overline{s})$, and $|G_0\rangle$ would mix into $|u\overline{u}+d\overline{d}+s\overline{s}\rangle$. However, since in reality $E(s\overline{s}) > E(d\overline{d})$, the flavour symmetry is broken. The case of the primitive glueball mass lying midway between $E(s\overline{s})$ and $E(d\overline{d})$, that is

$$E(G_0) = \frac{1}{2}\left[E(s\overline{s}) - E(d\overline{d})\right] + E(d\overline{d}),$$

gives the mixing to be between the primitive glueball, $|G_0\rangle$, and the state $|u\overline{u} + d\overline{d} - s\overline{s}\rangle$. The minus sign for the $s\overline{s}$ term implies destructive interference in channels with a strong $s\overline{s}$ component, such as $K\overline{K}$.

Although Close and Amsler's treatment is non-relativistic, it appears to provide a consistent description of the scalar nonet. A more sophisticated relativistic treatment has been given by Törnqvist [47]. This uses six parameters to describe the whole nonet, and predicts the masses of each scalar state. A primitive gg state is not included in Törnqvist's treatment, all primitive states being $q\overline{q}$. A discussion is given by Pennington in [23], where he compares the observed 0^{++} states with those predicted by Törnqvist's and Close and Amsler's models. This is shown in figure 2.6. If it is assumed that all the scalar states in the 1500-1600 MeV/c^2 region are in fact the same state, then Törnqvist's picture, using only primitive $q\overline{q}$ states, cannot include the $f_0(1370)$, the $a_0(1430)$ (not discussed here) and in particular the

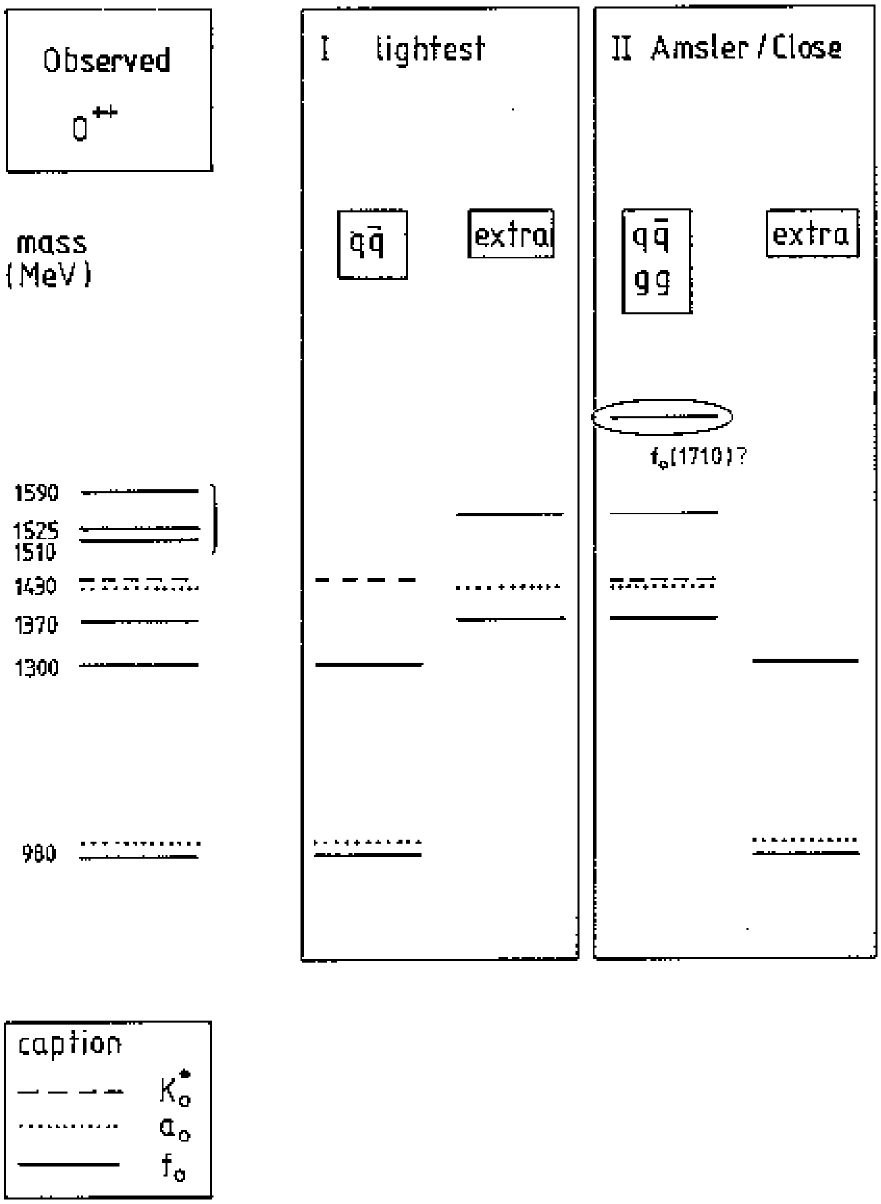

Figure 2.6: Comparison of the observed spectrum of 0^{++} mesons with(I) the scheme supported by Törnqvist's calculation [47] and (II) the scheme of Close and Amsler [45] (from Pennington [23]).

$f_0(1500)$ state.

The Amsler-Close scheme, using nine primitive $q\overline{q}$ states and one gg state, requires 10 states into the scalar multiplet, one of which is an $s\overline{s}$ scalar above 1700 MeV/c^2. In fact there is a state coupling strongly to $K\overline{K}$ at this mass, the $f_J(1710)$. This state is seen in radiative J/ψ decay [48] and in central production [43]. However, the spin assignment is uncertain, with Mark III favouring spin 0, and WA76 favouring spin 2. High statistics data taken by the WA91 collaboration on central production reactions may help to clarify this problem. Also in the Close-Amsler scheme, the $f_0(1500)$ is included naturally as a mixture between the primitive glueball and the $q\overline{q}$ states. The $f_0(1370)$ is the isospin 0 partner of the $f_0(1500)$, and turns out to be composed predominantly of $(u\overline{u} + d\overline{d})$. The $a_0(980)$ and the $f_0(980)$ in this model are excluded, and Close and Amsler identify these with $K\overline{K}$ molecules.

2.2 Summary

The $J^{PC} = 0^{++}$ sector is not well understood, even though it is probably not influenced by radial excitations in this mass region. Several states have been identified in glue rich reactions at around 1500 MeV/c^2. If these states are in fact all the same, then they may be described by two independent models. In the Törnqvist picture, the state cannot be included into the nonet as a standard $q\overline{q}$ object. In Amsler and Close's description, the state is naturally included as the tenth member of the multiplet by starting from nine primitive $q\overline{q}$ states and one primitive gg state, and allowing these to mix to produce the observed mesons.

Chapter 3

WA91 Experimental Details

3.1 Introduction

Experiment WA91 is designed to observe centrally produced hadrons formed at 450 GeV/c in the reaction

$$\mathrm{pp}\rightarrow\mathrm{p}_f X^0 \mathrm{p}_s,$$

where the subscripts f and s refer to the fastest and slowest particles respectively in the laboratory frame, and X^0 represents the neutral, centrally produced system. The reaction is shown in the centre-of-mass frame in figure 1.5.

As discussed in chapter 1, DPE is expected to be dominant at high $\sqrt{s}$ and low $|t|$. WA91 is designed to take data in this kinematic region, and bearing in mind the fact that Pomerons are supposed to have a large gluonic content, the WA91 experiment is thus well suited to search for non-$\mathrm{q\overline{q}}$ objects.

The successful WA76 and WA76$'$ programmes ran similar studies at 85 GeV/c and 300 GeV/c respectively. The main motivation of the extension to WA91 at 450 GeV/c was to study final states produced at higher centre-of-mass energies, and to increase the efficiency for detecting neutral channels. The experiment was carried out at the CERN Ω spectrometer using the H1 beam line [49] of the CERN SPS.

In this chapter, the details of the experiment as used in the 1992 data taking period are described. The main elements of the detectors are discussed, and a description of the WA91 trigger is given.

3.2 The Ω Spectrometer

The Ω spectrometer is a multi-user detector which is designed to take data on reactions which produce many particles in the final state. The spectrometer consists of two superconducting Helmholtz coils that produce a magnetic field of up to 1.8 T at the centre of the field region. For the WA91 programme, the central field used was 1.35 T. This allows accurate reconstruction of the fast and medium tracks, and also gives good acceptance for the slow tracks.

The standard Ω configuration consists of 15 multiwire proportional chambers (MWPCs), described in subsection 3.2.4, with a total of approximately 37,000 wires inside the volume of the spectrometer field region, and two large drift chambers (section 3.2.6) outside the magnet and downstream of the interaction region, which are used to increase the precision of the measured track parameters. The layout for the 1992 WA91 run is shown in figure 3.1.

A description of the components shown in figure 3.1 is given below in more detail. For a discussion of the general construction and properties of detectors similar to those utilised in WA91, the reader is referred to [50], [51].

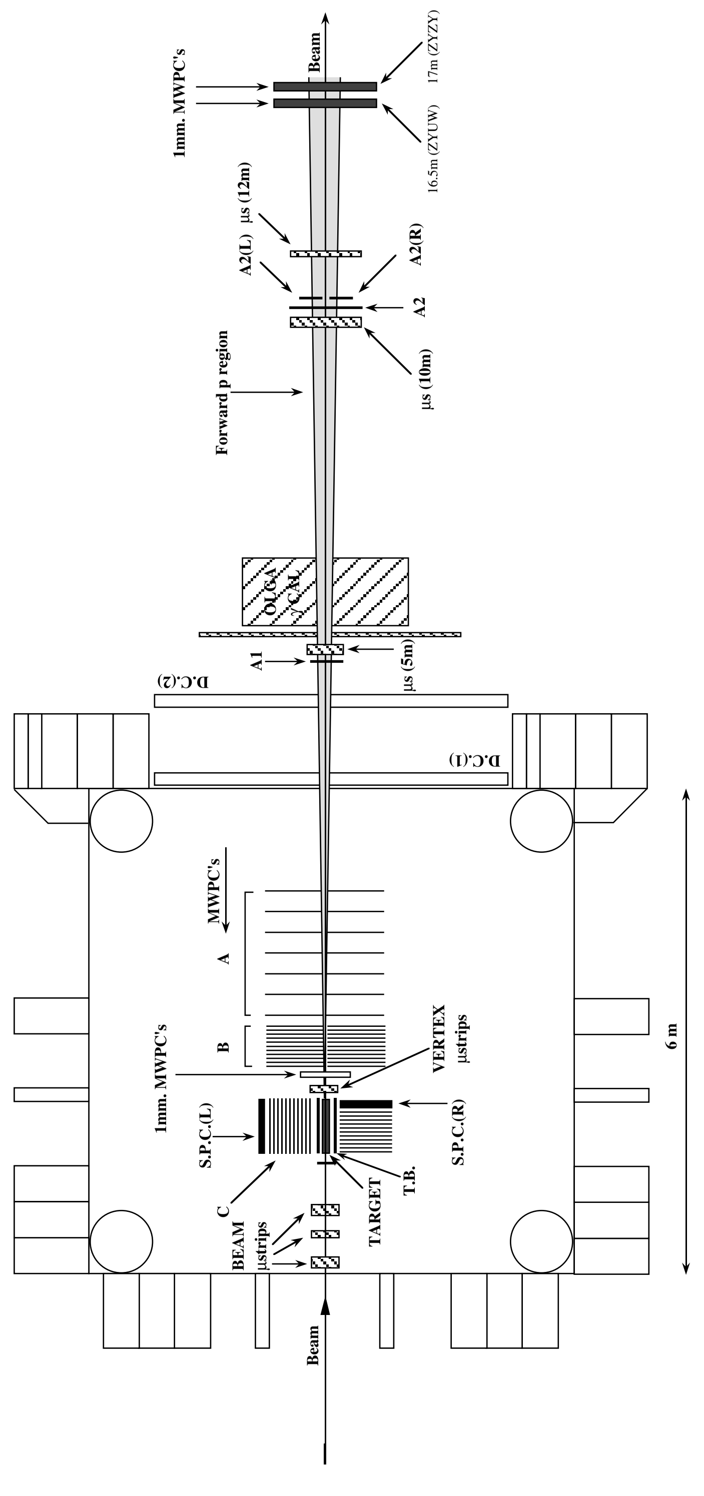

Figure 3.1: The Ω layout for the 1992 WA91 run

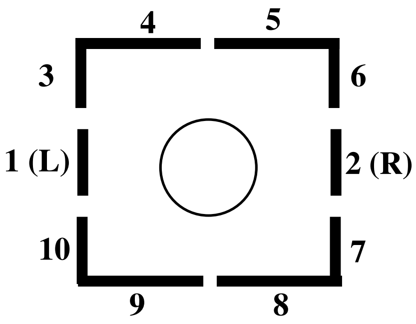

Figure 3.2: The numbering of the target box elements

3.2.1 The Beam

The H1 beam is a 450 GeV/c proton beam extracted from the CERN SPS. No secondary targets are used, and hence the beam is essentially 100% protons.

3.2.2 The Target

The target is a 60 cm long cylinder of liquid hydrogen, representing 15% of an interaction length (see A.1), contained within a mylar and aluminium canister. It is common to use beryllium targets to give a similar interaction length in a shorter physical distance (which enables the interaction vertex to be reconstructed more easily). However, this is not done in WA91 so as not to introduce nuclear effects, and to ensure that only pp interactions can occur. The interaction vertex can be reconstructed accurately in the beam direction by the slow proton detection system (see sections 3.2.4 and 3.2.5).

3.2.3 The Target Box (TB)

The target box consists of 10 scintillator slabs surrounding the target on 4 sides and numbered as shown in figure 3.2. The box is left open at the upstream and downstream ends in order to let through the beam and forward particles. The box is 60 cm long, 28 cm high, and slabs 1 and 2 are 0.5 cm thick, all other slabs being 1 cm thick. It is used in the slow particle trigger, as described in section 3.3.3.

3.2.4 The Multiwire Proportional Chambers (MWPCs)

The MWPCs are labelled A, B and C in figure 3.1. The A and B chambers are located downstream of the target and are used to define the medium momentum, forward-going tracks. The C chambers are positioned on either side of the target, and are used to measure the the slow particle tracks. The left C chambers are mounted with their planes parallel the optical bench, and the right C chambers are mounted perpendicularly to this. The reason for this arrangement is shown in figure 3.3. It may be seen that because of the sense in which positive particles are bent in the Ω magnetic field, in order to get the best acceptance for slow particles the two C chambers must be mounted at right angles to each other. However, the acceptance of the right C chambers is still limited, as may be seen by closer examination of figure 3.3. Particles travelling to the left from any origin along the length of the target have a high probability of traversing all or nearly all of the planes in the left C chambers, but those moving to the right in the magnetic field will only traverse a significant number of planes in the right C chambers for a more limited set of origins along the length of the target cylinder. This is an important effect, as may be seen from the results presented in section 3.3.5.

The A chambers consist of 7 modules, each containing 3 planes of wires, labelled Y, U and V. The Y planes are inclined to the vertical in the Ω system, and the U and V planes are inclined at $\pm 10.14°$ to the Y planes in order to facilitate the tracing of tracks as they pass through the system. The B and C chambers have 8 modules, each consisting of 2 planes, one Y and the other alternately U and V. In all cases, the wire spacing is 2 mm. The chambers are filled with a mixture of isobutane and alcohol.

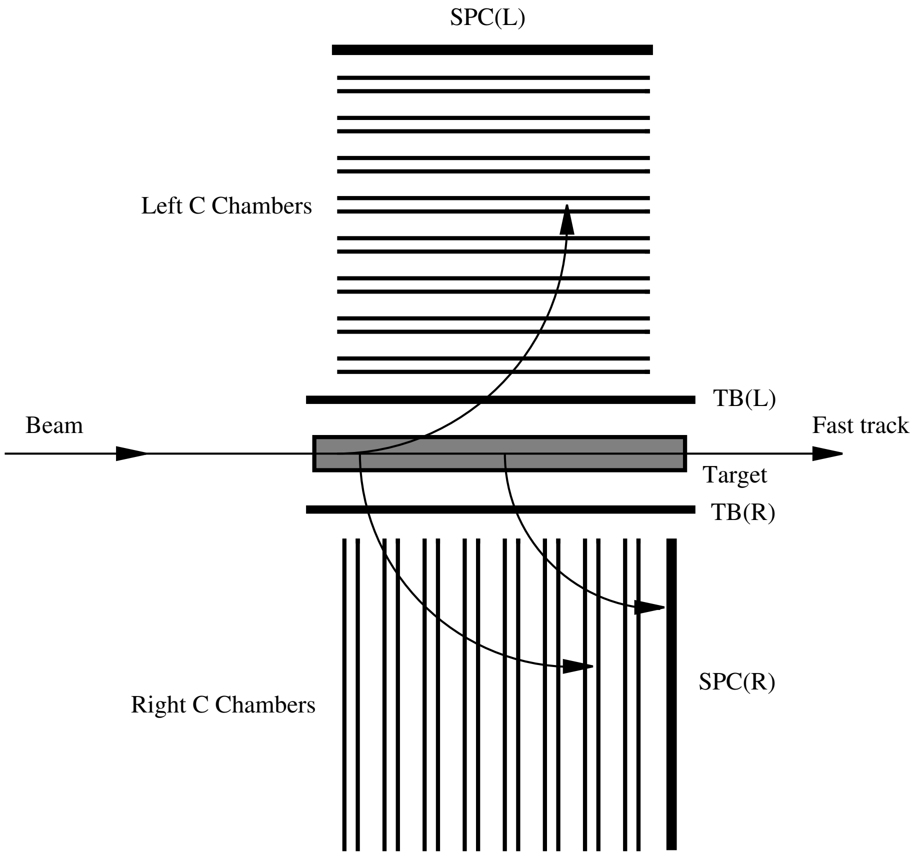

Figure 3.3: Mounting of the C chambers

In addition to the standard Ω chambers, WA91 also uses 3 further sets of MWPCs with a wire spacing of 1 mm. The first of these is located downstream of the target between the vertex microstrip detector and the B chambers. It has 4 planes, Y, Z, U and V, where the Z direction is perpendicular to both Y and the beam direction, and is used to give extra points for track reconstruction for the fast track and for centrally produced tracks. The other 2 chambers are placed at 16.5 m and 17 m downstream of the Ω centre. They each have 4 planes (ZYUV and ZYZY) and are used to provide extra information for accurate reconstruction of the fast track.

3.2.5 The Slow Proton Counters (SPCs)

There are two slow proton counters, one on either side of the target and after the C chambers, labelled SPC(L) and SPC(R) in figure 3.1 to denote the left and right sides relative to the beam direction. They both are composed of 14 scintillator slabs held in an aluminium frame in such a way that the entire assembly is vertical. SPC(R) has a slab width of 7 cm, and SPC(L) has a slab width of 6 cm. SPC(L) has an active length of approximately 1 m, and SPC(R) approximately 70 cm, and both are used for slow proton identification in conjunction with the C chambers. Slow pions are antiselected by consideration of the pulse heights of the signals in the SPCs. At this point, it is appropriate to digress briefly from the discussion of the detector layout to describe how this is done.

The Bethe–Bloch formula [4],

$$-\frac{dE}{dx} = Kz^2 \frac{Z}{A} \frac{1}{\beta^2} \left[\frac{1}{2} \ln \frac{2m_e c^2 \beta^2 \gamma^2 T_{max}}{I^2} - \beta^2 - \frac{\delta}{2} \right],$$

gives the energy loss of a charged particle travelling through a dense medium. K/A is a measure of the energy deposited per unit mass of absorber with unit area, and can be calculated to be 0.307 MeV g^{-1} cm^2 [4]. The charge of the incident particle is z in units of the electron charge, Z is the atomic number of the medium, I characterizes the binding energy of the atomic electrons in the medium in units of eV, and δ represents corrections due to density effects. A total pulse height versus momentum plot for SPC(L) is shown in figure 3.4. The maximum on the plot corresponds to a particle just being stopped in the medium and giving up all of its energy. The broad band labelled p at the top of the distribution is due to slow protons, and the region with increased density labelled π in the lower portion of the plot is due to pions stopping in the scintillator. By carefully adjusting the discriminator for each slab in the SPCs, or by using a software cut, the pion signals can be essentially completely removed. Thus protons can be selected from the total slow particle spectrum.

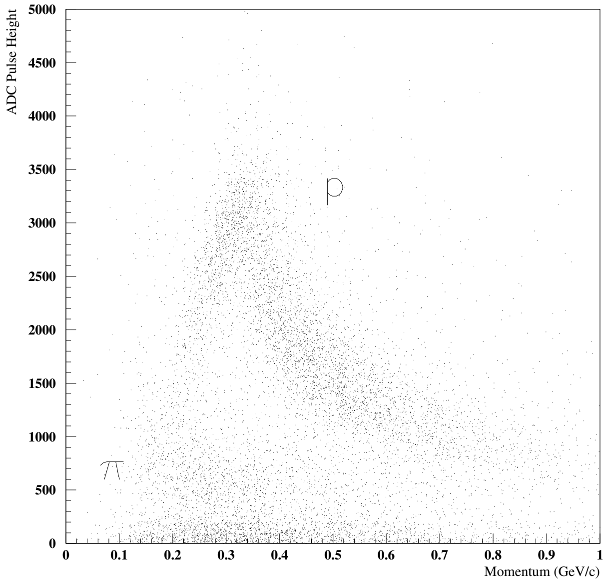

Figure 3.4: Pulse height versus momentum for SPC(L).

3.2.6 The Drift Chambers (DC(1) and DC(2))

Immediately outside the Ω magnet, at 3.27 m and 4.41 m from the centre of the field region, are situated two high-precision drift chambers, marked DC(1) and DC(2) in figure 3.1. Each chamber comprises 4 planes, Y, U, Y and V, using the same notation as that for the MWPCs in subsection 3.2.4. Each plane has a 2.5 cm spacing between the sense (where the liberated electrons are collected) and field wires (used to stabilise the field across the volume of the chamber, see [50]), and the drift time is $\sim$5 cm/μs. The drift chambers are used to reconstruct the tracks of medium momentum particles.

3.2.7 Microstrip Detectors

Five separate sets of silicon microstrip detectors are used, labelled BEAM, VERTEX, 5 m, 10 m and 12 m in figure 3.1. They consist of silicon strips of several different pitches held at a bias voltage of $\sim$50 V. Their high spatial accuracy is useful in

WA91 in two important respects :

- **Beam reconstruction** 10 planes, grouped into pairs, are used to define the direction of the beam. All the pair modules are attached to a rigid optical bench. The optical bench serves as a coordinate reference for all the microstrip planes. The modules are positioned on the bench in 3 groups, labelled BEAM1, BEAM2 and BEAM3, as tabulated in table 3.1.

Table 3.1: Details of the microstrips used in the 1992 run.

Name	Planes	Pitch	Channels	Dimensions (mm)	x position (m)
BEAM1	4 (ZYZY)	20 μm	512	10.24×10.24	$-3.998, -3.998, -3.942, -3.931$
BEAM2	2 (ZY)	20 μm	512	10.24×10.24	$-3.326, -3.315$
BEAM3	4 (ZYYZ)	20 μm	512	10.24×10.24	$-2.729, -2.718, -2.686, -2.676$
VERTEX	4 (ZYYZ)	25 μm	2048	51.2×51.2	$-0.969, -0.944, -0.919, -0.894$
5m A1	4 (ZYZY)	25 μm	2048	51.2×51.2	$5.330, 5.335, 5.380, 5.405$
10m A2	4 (ZYZY)	25 μm	2048	51.2×51.2	$10.462, 10.487, 10.512, 10.537$
12m A2	2 (YY)	50 μm	2048	51.2×51.2	$12.501, 12.553$

- **Fast track reconstruction** Four sets of microstrips (labelled VERTEX, 5 m, 10 m and 12 m) are used, positioned as shown in table 3.1. The VERTEX detector is also used to help reconstruct the tracks from medium momentum particles, which gives an improved efficiency in locating V^0 decays. Furthermore, the downstream microstrips are also used to identify beam particles which have not interacted in the target.

3.2.8 The Electromagnetic Calorimeter (OLGA)

Some particles produced in the interaction region may decay electromagnetically to photons. These decays are detected by the Omega Lead Glass Apparatus (OLGA) calorimeter. A schematic diagram of OLGA is shown in figure 3.5.

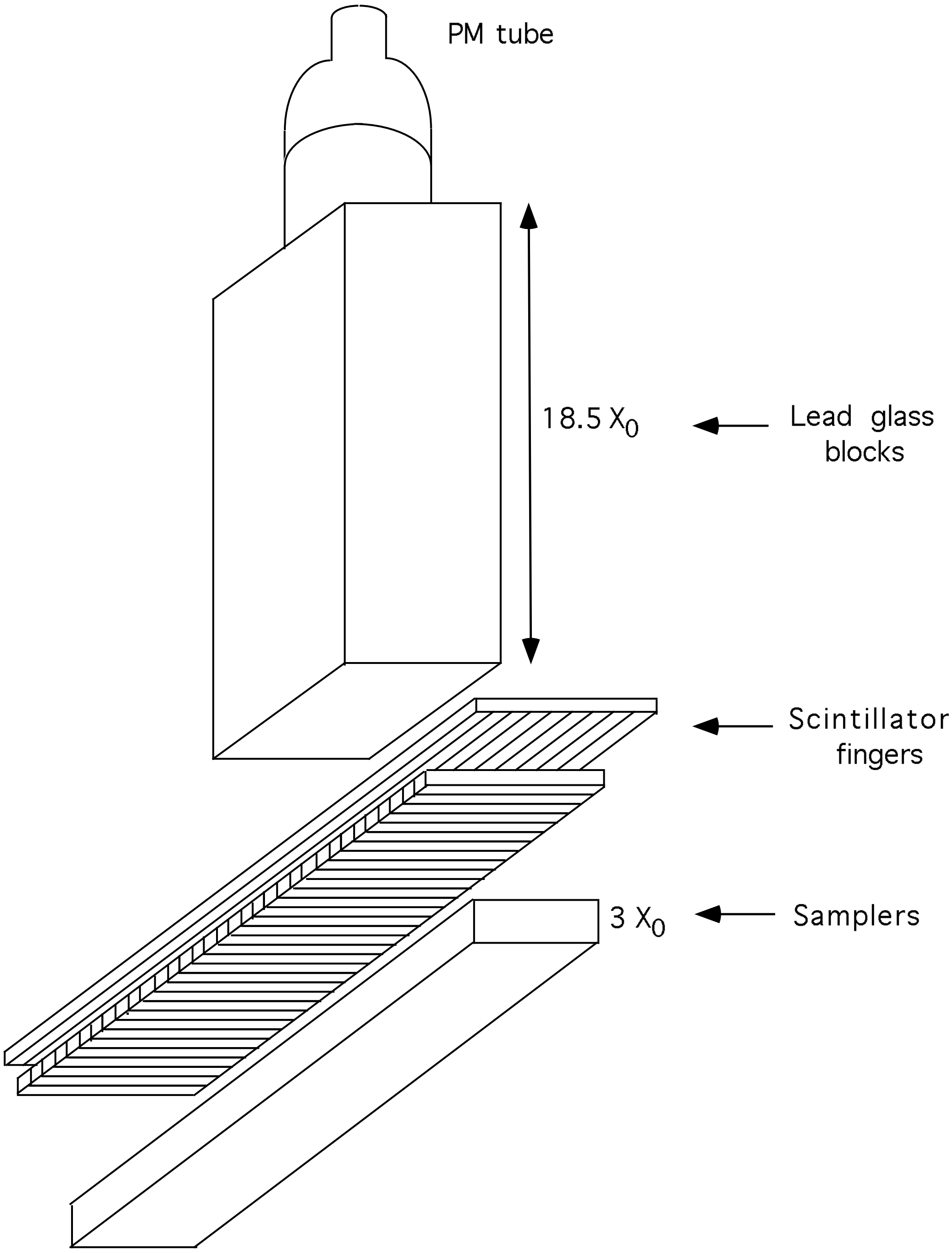

Figure 3.5: Schematic diagram of OLGA

OLGA has three modules :

1. **Lead glass blocks** These are arranged in an array of 18×19 blocks, each with an area of 14×14 cm^2 and a depth of 47 cm. This corresponds to approximately 18.5 radiation lengths. For the 1992 run, the central block was removed in order to allow the beam and fast track particles to pass through OLGA.

2. **Samplers** These are large slabs of lead glass with area 14×145 cm^2 and depth 10 cm, corresponding to 3 radiation lengths. They are arranged in columns of 19 slabs down the right and left halves of the front face of the calorimeter. The amount of energy deposited by an electromagnetic shower in the samplers gives an estimate of the energy of the initial photon causing the shower. This energy is measured to higher accuracy in the lead glass array.

3. **Positional detector** This consists of fingers of scintillator material arranged in four half-planes. Two of these are horizontal, made up of 180 fingers of dimension 147 cm$\times$1.53 cm$\times$1 cm, and the remaining two are vertical, consisting of 180 fingers of dimension 152 cm$\times$1.53 cm$\times$1 cm. An electromagnetic shower in the fingers allows the position of the incident photon to be established.

The front face of the samplers was located 6.1 m downstream from the centre of Ω.

3.2.9 Downstream Scintillation Counters (A1, A2, A2(L), A2(R))

A1 and A2 are used in the definition of the WA91 trigger, as will be described in section 3.3. A1 is a square slab of scintillator of side 2.5 cm, positioned 4.9 m downstream of the Ω centre, and A2 is a square slab of side 5.0 cm, positioned at 10.8 m. A2(L) and A2(R) are located immediately behind A2, to the left and right

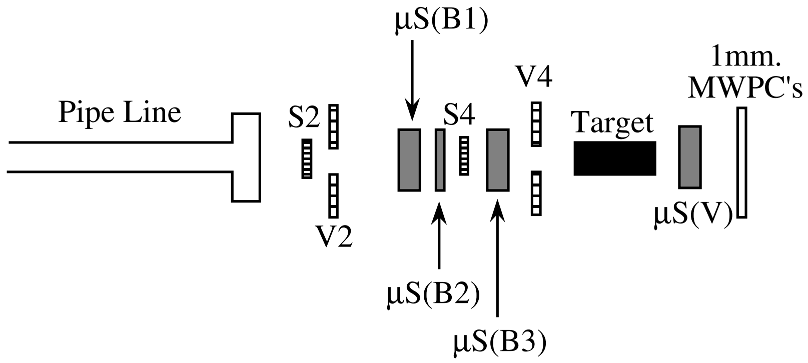

Figure 3.6: Positions of beam counters in relation to target

sides of the beam direction, as shown in figure 3.1, and are used to find the fast track direction (see section 3.3.5).

3.2.10 Beam Counters

Not shown on figure 3.1 are 4 scintillation counters used to define a beam signal before interactions with the target, as will be discussed in section 3.3. These are shown in figure 3.6, where the labels B and V designate the beam and vertex detectors. Two detectors (S2 and S4) are beam signal counters, and the remaining two (V2 and V4) are beam vetos. S2 is a square slab of scintillator of side 2.5 cm and thickness 0.5 cm. S4 is also a square slab of side 0.8 cm. V2 and V4 are similar slabs of side 17 cm, but each has a small hole for the beam to travel through. For V2, this hole is of diameter 1.5 cm, and for V4, 0.8 cm. Both V2 and V4 are 1 cm in thickness.

3.3 The Trigger

In any high–multiplicity high energy physics experiment, an efficient trigger which selects only those events which are of interest is vital. For WA91, the most important trigger conditions are to select those events which have one fast proton, one slow proton, and two or more medium momentum particles. In this section, a description of the various trigger elements which are required for this task is given. A full trigger diagram is shown in figure 3.7.

3.3.1 Clean Beam Signal

A beam signal is defined by the condition that S2 and S4 fire, but V2 and V4 do not, *i.e.*, the beam particle has passed through the material of S2 and S4, but through the holes in V2 and V4. Clean beam is then defined by requiring that only *one* particle has passed through S2. In order to understand this, consider the diagram shown in figure 3.8. An extra signal (S2P) is taken from the S2 counter. This signal is split into a shaped pulse, and an inverted pulse. Clean beam (CB) is then defined by coincidence between S2, the inverse of S2P, the shaped S2P pulse and a beam signal. Careful choice of the delays brings the signals into the configuration shown in figure 3.9. Note that S2P starts just after the end of $\overline{\mathrm{S2P}}$, and only $\overline{\mathrm{S2P}}$ updates. Because of this timing, the coincidence will, in general, be satisfied for one particle passing through the system. However, if after a time Δt, a second particle arrives (as shown by a dashed line in figure 3.9), $\overline{\mathrm{S2P}}$ will have a longer duration, and the coincidence condition will not be satisfied. Hence events where more than one particle arrives within the pulse width of $\overline{\mathrm{S2P}}$ will be rejected.

3.3.2 Fast Particle Trigger

This is done by asking for coincidence between signals from the A1 and A2 counters, described in section 3.2.9.

WA91 TRIGGER LOGIC (1992/P2)

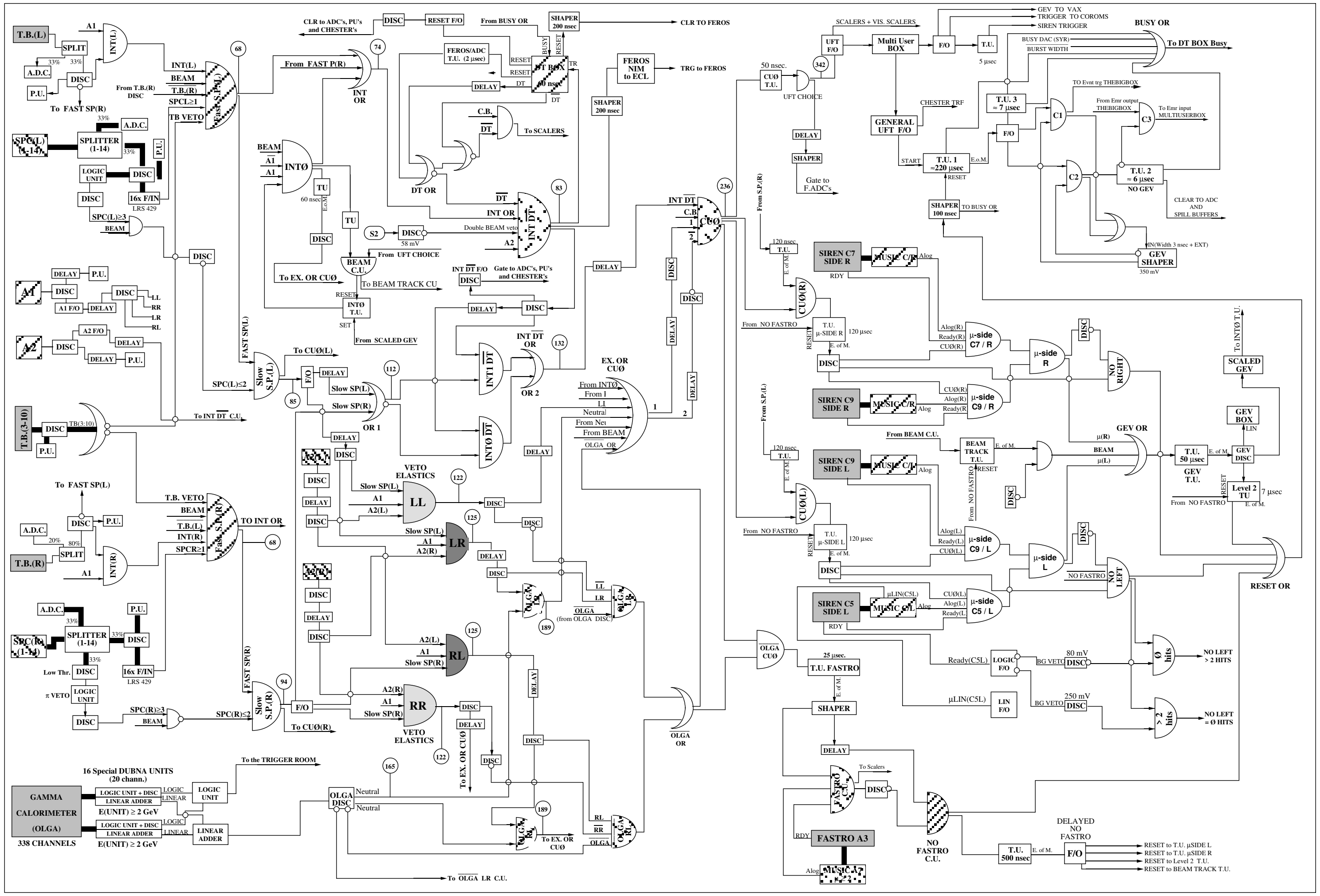

V. LENTI 19/11/1992

Figure 3.7: The WA91 trigger for 1992

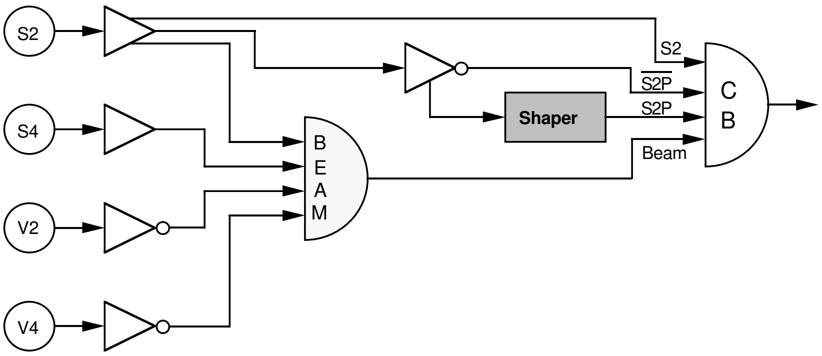

Figure 3.8: Logic used to define a clean beam signal

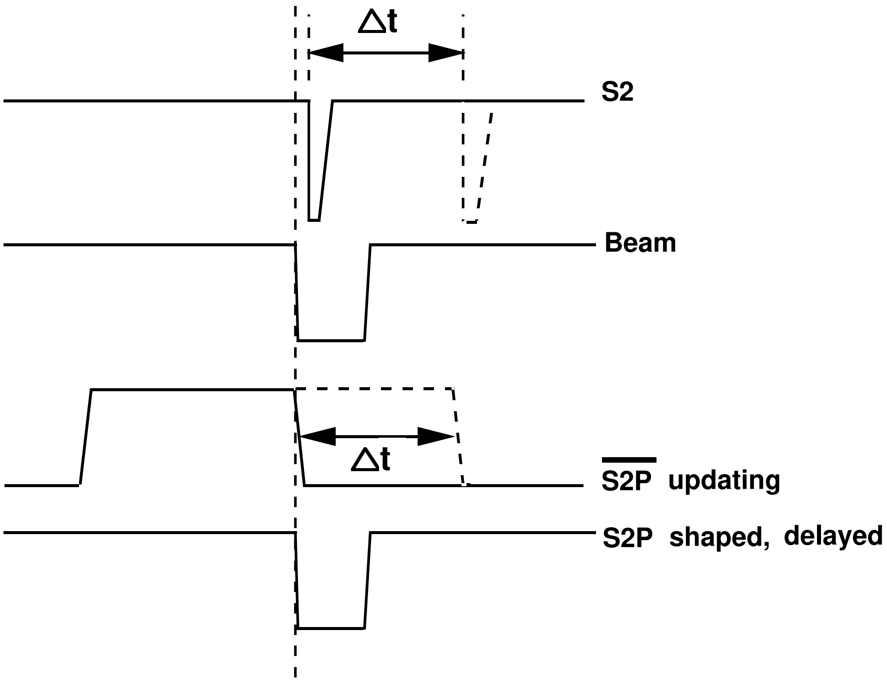

Figure 3.9: Timing of clean beam coincidence signals

3.3.3 Slow Particle Trigger

The trigger for slow protons requires a coincidence between a signal from one side of the target box (either TB1(L) or TB2(R), see section 3.2.3) and a signal from only one or two slabs in the slow proton counter (section 3.2.5) *on the same side*; that is, coincidence is required between TB1(L) and SPC(L) or TB2(R) and SPC(R).

A competing process with central production is target diffraction. A typical target diffraction event is shown in figure 3.10. Several slow particles in the laboratory

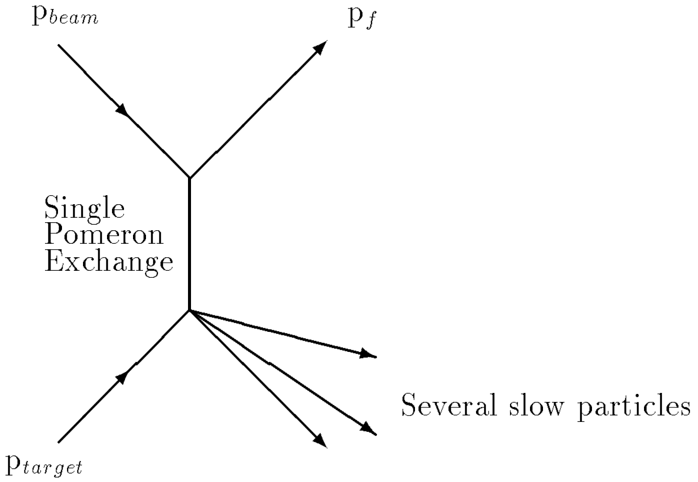

Figure 3.10: A typical target diffraction event

frame are produced, and the trigger must be required to antiselect such events. In order to do this, it is verified that no other slabs fire in the target box. The requirement that only one or two slabs fire in the SPC further reduces target diffraction effects by removing those events that have several slow particles going through only one slab of the target box.

Table 3.2: Event classification for the 1992 run

Trigger	BEAM	SPC(L)	SPC(R)	A2(L)	A2(R)	FASTRO	OLGA	Class	Proportion(%)
LEVEL1	Yes	Yes	No	Yes	No	–	–	LL	64.0
	Yes	No	Yes	No	Yes	–	–	RR	6.6
	Yes	Yes	No	No	Yes	–	Yes	LR&OLGA	8.8
	Yes	No	Yes	Yes	No	–	Yes	RL&OLGA	4.0
	Yes	–	–	–	–	–	–	BEAM	6.6
LEVEL2	Yes	Yes	No	No	Yes	Yes	No	LR&FASTRO	10.0

3.3.4 Neutral Particle Trigger

OLGA is used to select neutral particle decays. A neutral trigger is defined as having at least 2 GeV deposited in any OLGA block.

3.3.5 Classification Of Events

Events which pass the trigger conditions are classified according to the scheme shown in table 3.2. The first letter of the class assignments denotes which SPC was triggered, the second letter shows which of A2(L) and A2(R) fired. The so-called LEVEL 1 triggers are the fast triggers on an event, LL, RR, LR and RL being assigned in 125 ns after the initial S2 pulse, and the extra OLGA decision coming within 190 ns. The low relative proportions of events relying on triggering in SPC(R) may be interpreted as being due to the low acceptance of the right C chambers, as remarked on in section 3.2.4.

Events which have their origin in elastic scattering of the pp system can be largely eliminated by selecting only those events where the fast particle and the slow particle are both on the same side of the detector system, if there are no signals in OLGA. The LEVEL 2 trigger requires that only one or two wires fire in planes 5 and 7 of the left C chambers, or planes 7 and 9 of the right C chambers, assuming the appropriate LEVEL 1 conditions were satisfied. This results in a significant increase in track reconstruction efficiency. Furthermore, LEVEL 2 uses the Fast Readout

(FASTRO) trigger to check those events where the fast and slow particles go in different directions and there is no energy deposited in OLGA, but there is still a reasonable number of hits the the A chambers. FASTRO requires that there be two or more hits outside the beam region in the third plane of the A MWPC. This has the effect of increasing the reconstruction efficiency for channels such as $\pi^+\pi^-$, where the particles do not decay electromagnetically. FASTRO reads A3 in groups of 8 wires at a time (this decreases the readout time by a factor of ~ 10 from ~ 100 μs for individual wire readout).

3.4 Event Statistics For The 1992 Run

The beam flux from the SPS for the 1992 run was approximately 5×10^6 protons per second, with a burst time of 2.4 s. Around 500 events were recorded per burst, leading to 8.4×10^7 events over 43 days of data taking.

3.5 Event Reconstruction

The experimental data taken were processed through a track reconstruction program, TRIDENT, which attempts to reconstruct events by track recognition, momentum calculation and the production of fits to primary or secondary vertices. Wire hits in several planes at different inclinations are combined to provide a large number of constraints to the fitting procedure and to help reduce chamber inefficiencies.

The x coordinate of the primary vertex is found by intersecting the beam track with the slow proton track. The beam track is then retraced to this x position to give the y and z coordinates of the primary vertex. Forward going tracks are traced back from the drift chambers where they have been well separated by the bending effect of the magnet through the A and B chambers, and a fit is made to find the best track hypothesis. At this stage, tracks coming from the decay of a V^0 near the primary vertex may be incorrectly assigned as originating at the primary vertex. In order to overcome this, after the initial TRIDENT run the events are run through a V^0 recovery program [52]. This takes all combinations of positive and negative tracks that have not been assigned to a V^0 by TRIDENT. The combinations are required to trace to a vertex at least 3 cm downstream from the primary target, with an impact parameter greater than 0.05 cm at the primary vertex.

3.6 Summary

The main elements of the WA91 set up used during the 1992 run of the experiment have been described. The trigger has been discussed in some detail, and a brief description of the event reconstruction has been given.

Chapter 4

The 1992 $\pi^+\pi^-$ Mass Spectrum

4.1 Introduction

The WA76 observation of a state compatible with the $f_0(1500)$ in the central $\pi^+\pi^-$ channel (see section 2.1) is clearly interesting, and prompts further analysis. In particular, a full spin analysis of this mass region is required, which has not previously been attempted for central production at this energy. In this chapter, the selection of $\pi^+\pi^-$ events from the WA91 1992 data is described, leading to a high statistics data set. The formalism used to fit the mass spectrum is discussed, and a fit presented, where it will be shown that a term is needed in the fit parameterization to describe the contribution of the $f_0(1500)$ to this channel.

4.2 Selection of the $\pi^+\pi^-$ channel

The reaction

$$\mathrm{pp} \to \mathrm{p}_f\ (\pi^+\pi^-)\ \mathrm{p}_s\ ,$$

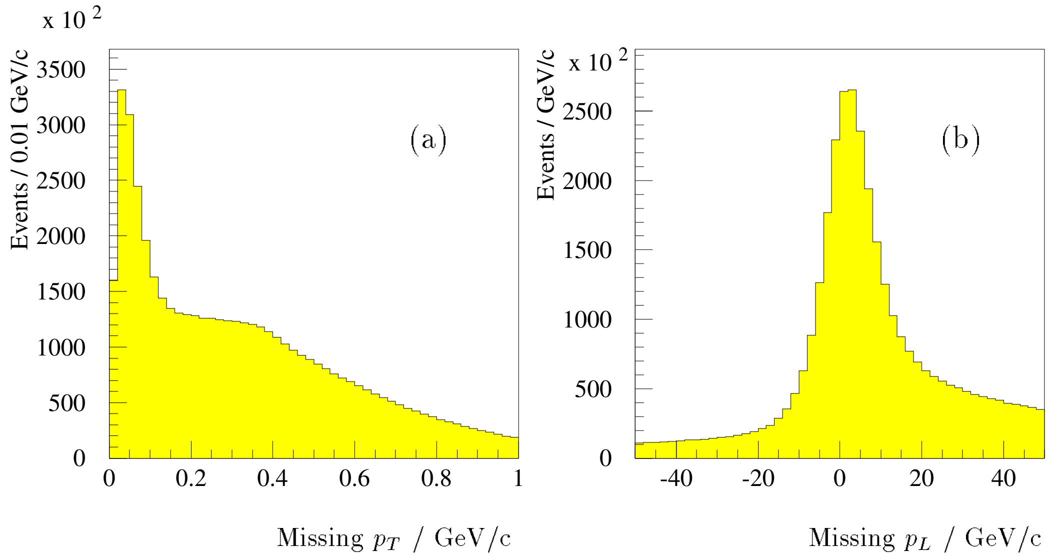

Figure 4.1: Missing momentum distributions for WA91 events with 4 outgoing tracks. Figure a) shows the missing transverse momentum distribution, and b) the missing longitudinal momentum.

where the subscripts f and s refer to the fastest and slowest particles respectively in the laboratory frame, was selected from the sample of WA91 events with four outgoing tracks by applying the following cuts to the missing momentum components for each event :

$$\begin{aligned} |\text{missing } p_x| &< 14.0 \text{ GeV}/c, \\ |\text{missing } p_y| &< 0.16 \text{ GeV}/c, \\ |\text{missing } p_z| &< 0.08 \text{ GeV}/c. \end{aligned}$$

Figures 4.1 a and b show the missing transverse and longitudinal momentum distributions before the cuts are made. A clear signal of events having good p_x, p_y, p_z and energy information can be seen at low missing transverse momentum, p_T ("4C events").

The Ehrlich Mass squared [53] (see appendix A) was calculated for each event in order to select those tracks compatible with being $\pi^+\pi^-$. A plot is shown in figure 4.2. Visible are a clear peak at the π mass squared, together with a shoulder

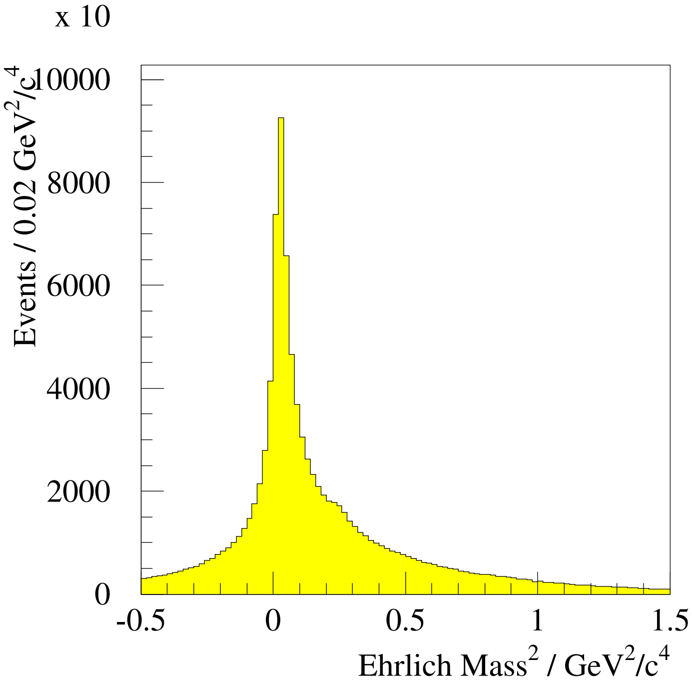

Figure 4.2: The Ehrlich mass squared for WA91 $\pi^+\pi^-$ events.

at the K mass squared. Cuts were made on the Ehrlich Mass squared such that events were only accepted in the mass squared region between -0.3 GeV$^2/c^4$ and 0.2 GeV$^2/c^4$.

The variable *Feynman x*, x_F, is defined by the relation

$$x_F = \frac{p_L}{p_{L_{max}}},$$

where $p_{L_{max}}$ represents the maximum longitudinal momentum available for a particle. In the centre of mass frame, the fast proton will have essentially $x_F = +1$, the slow proton $x_F = -1$, and the central $\pi^+\pi^-$ system $x_F \sim 0$. The x_F distribution is shown in figure 4.3. The 3 structures are clearly visible, but there is also a broad smearing between $x_F = 0$ and $x_F = +1$. In order to understand this effect, it is necessary to consider the $p_f\pi^+$ mass spectrum, shown in figure 4.4. A clear $\Delta^{++}(1232)$

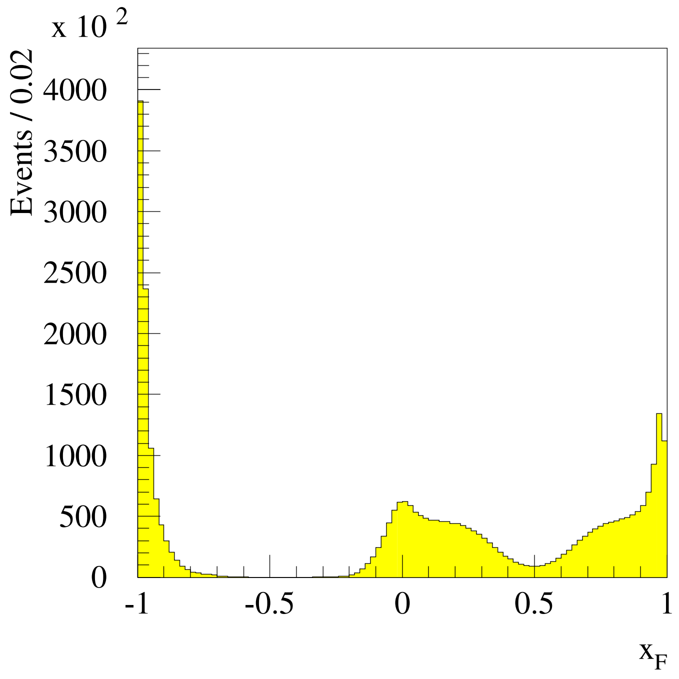

Figure 4.3: x_F for WA91 $\pi^+\pi^-$ events, before the cut on the Δ^{++} signal in the $\pi^+\mathrm{p_f}$ channel.

signal is observed in this channel, and can be removed from the $\pi^+\pi^-$ channel by requiring $m_{\mathrm{p}\pi} \geq 1.5$ GeV/c^2. In reconsidering the x_F plot for the $\pi^+\pi^-$ system, it is observed that most of the smearing in the positive x_F region has been eliminated, and the central system at $x_F \approx 0$ is unambiguously identified, as may be seen in figure 4.5.

4.2.1 Cuts on 4-momentum transfer

Using the cuts described above, the $\pi^+\pi^-$ mass spectrum obtained is shown in figure 4.6. It consists of 289 459 events.

The 4-momentum transfer at the p_{beam}–p_f vertex is defined to be t_f, and that at the p_{target}-p_s vertex to be t_s; the total 4-momentum transfer, t, is then given by the sum of t_f and t_s. Since double Pomeron exchange is expected to be dominant at low t,

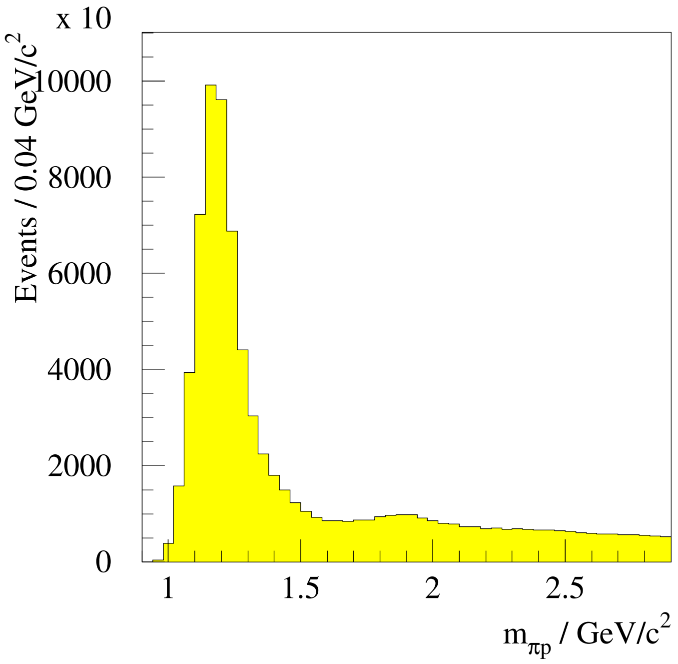

Figure 4.4: The $\pi^+ p_f$ mass spectrum.

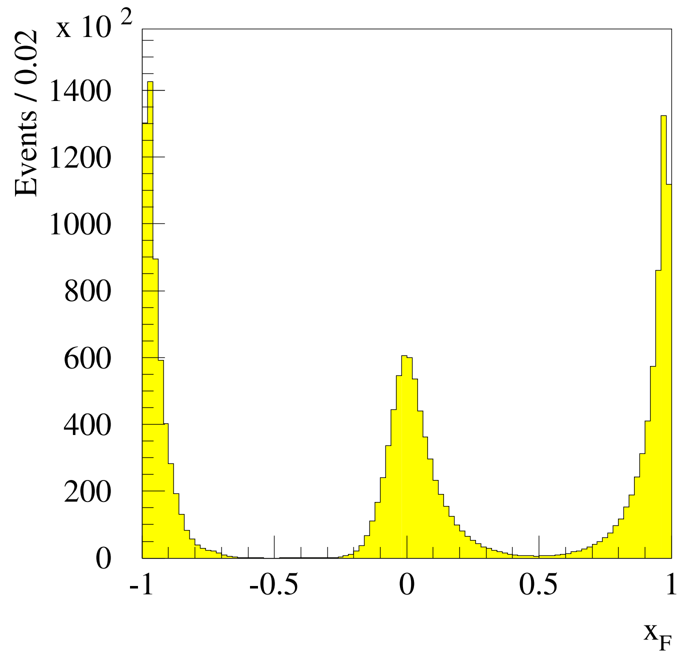

Figure 4.5: The x_F distribution after the Δ^{++} cut.

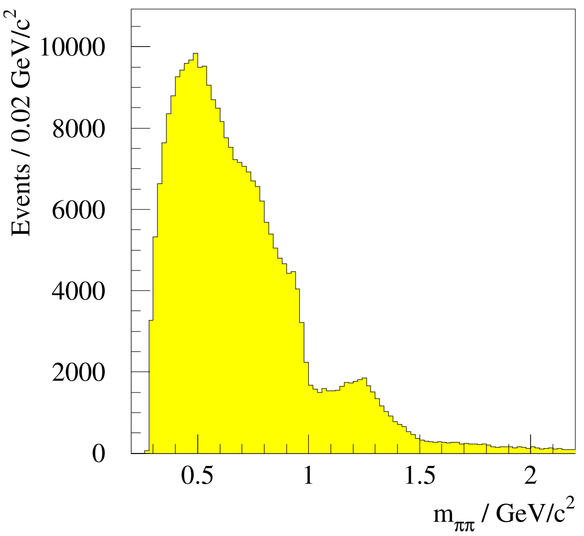

Figure 4.6: The WA91 $\pi^+\pi^-$ Mass Spectrum for all t.

the cut $|t| < 0.3$ GeV^2 is imposed. The final mass spectrum with this requirement is shown in figure 4.7a. This consists of 165 841 events. Shown in figure 4.7b is the equivalent spectrum for $|t| > 0.3$ GeV^2. Visible on the plots are clear $\rho(770)$ and $f_2(1270)$ signals. The drop at $\sim$1 GeV is attributed to the $f_0(980)$. The rapid decrease of phase space in this region is due to the coupling of the $f_0(980)$ to the $K\overline{K}$ channel, which has its threshold mass at approximately this point. The $\rho(770)$ and $f_2(1270)$ signals are suppressed at low t; this is consistent with the proposition that they are formed by Reggeon exchange, which is supposed to be the dominant production mechanism at higher t.

4.3 Parameterization of the $\pi^+\pi^-$ mass spectrum

In order to fit the mass spectrum, it is appropriate to use a relativistic spin-1 Breit–Wigner function [54] to describe the $\rho(770)$ resonance, and a relativistic spin-2 Breit–Wigner function to describe the $f_2(1270)$. However, the description of the $f_0(980)$ is more complicated since its mass is close to that of the $K\overline{K}$ threshold mass, and

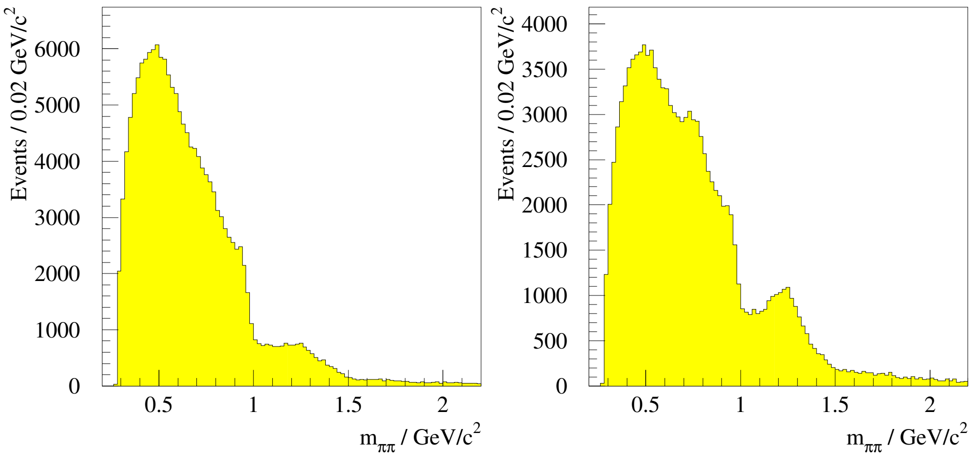

Figure 4.7: (a) The $\pi^+\pi^-$ mass spectrum for $|t| < 0.3$ GeV^2; (b) The spectrum for $|t| > 0.3$ GeV^2.

it has a large coupling to this channel in addition to $\pi^+\pi^-$. In this case, a *coupled channel* formalism must be used. Two functions, $F_\pi(m)$ and $F_K(m)$, are defined to describe the $f_0(980)$ mass region,

$$F_\pi(m) = \frac{m_0\sqrt{\Gamma_i}\sqrt{\Gamma_\pi}}{m_0^2 - m^2 - im_0(\Gamma_\pi + \Gamma_K)},$$

$$F_K(m) = \frac{m_0\sqrt{\Gamma_i}\sqrt{\Gamma_K}}{m_0^2 - m^2 - im_0(\Gamma_\pi + \Gamma_K)},$$

where Γ_i is the (unknown) coupling of the exchange particles to the central system, and Γ_π, Γ_K represent the $f_0(980)$ partial decay widths to the $\pi^+\pi^-$ and $K\overline{K}$ channels. These are the Flatté functions [55] for the $\pi^+\pi^-$ and $K\overline{K}$ channels. Γ_π and Γ_K may be interpreted in terms of the squares of the couplings, g_π and g_K, of the $f_0(980)$ to $\pi^+\pi^-$ and $K\overline{K}$, by writing them as

$$\begin{aligned}\Gamma_\pi &= g_\pi\sqrt{\frac{m^2}{4} - m_\pi^2},\\ \Gamma_K &= \frac{g_K}{2}\left(\sqrt{\frac{m^2}{4} - m_{K^+}^2} + \sqrt{\frac{m^2}{4} - m_{K^0}^2}\right).\end{aligned}$$

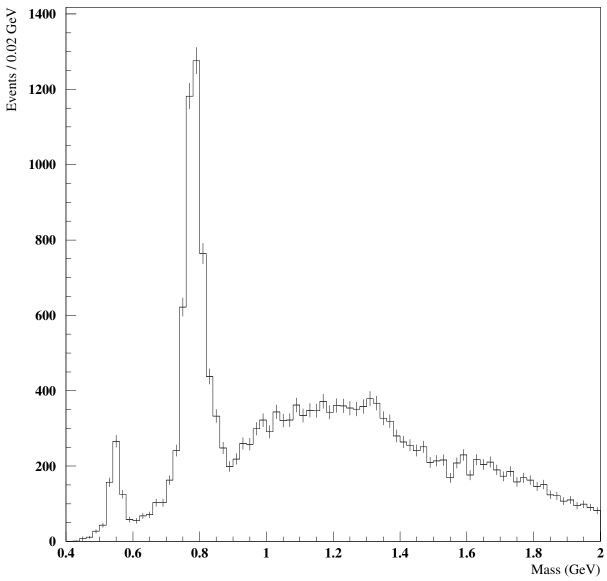

Figure 4.8: The $\pi^+\pi^-\pi^0$ mass spectrum.

The individual couplings for K^+K^- and $K^0\overline{K^0}$ are incorporated into a single $K\overline{K}$ coupling by averaging over the charged and neutral kaon masses. The background for the $\pi^+\pi^-$ channel may be parameterized as

$$G(m) = (m - m_{th})^{\alpha}\, e^{-\beta m - \gamma m^2},$$

where m_{th} is the $\pi^+\pi^-$ threshold mass and α, β, γ are free fit parameters.

In the $\pi^+\pi^-\pi^0$ channel there is a strong $\omega(783)$ signal, as may be seen from the mass spectrum shown in figure 4.8. This can appear as a reflection in the $\pi^+\pi^-$ mass spectrum if the π^0 is inside the missing p_T cuts for $\pi^+\pi^-$ event selection. The $\omega(783)$ events are simulated by making Monte Carlo $\omega(783)$ events and decaying these to $\pi^+\pi^-\pi^0$ in their rest frame. If this satisfies the same momentum balance cuts as are applied to the $\pi^+\pi^-$ system, then the mass of the $\pi^+\pi^-$ system is histogrammed. This histogram represents the shape of the contribution of the $\omega(783)$ reflection in the $\pi^+\pi^-$ channel, and is shown in figure 4.9. This histogram is included in the fit with a free amplitude.

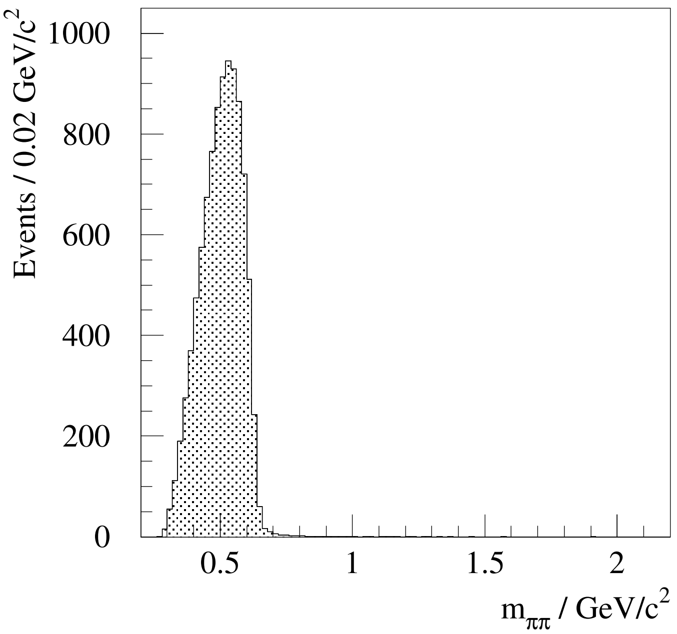

Figure 4.9: Simulated $\pi^+\pi^-$ events coming from the $\omega(783)$ in the $\pi^+\pi^-\pi^0$ channel.

With the above discussion in mind, the parameterization of the $\pi^+\pi^-$ mass spectrum at this stage is

$$\frac{dN}{dm} = A_\omega \omega(m) + G(m)\left[1 + A_{\mathrm{f}_0(980)}|F_\pi(m)|^2 + A_\rho B_\rho(m) + A_{\mathrm{f}_2} B_{\mathrm{f}_2}(m)\right],$$

where A_i, B_i represents the normalization and $|\text{amplitude}|^2$ respectively of the Breit–Wigner functions used to describe the resonances, $G(m)$ is the background parameterization, and $\omega(m)$ is the contribution of the $\omega(783)$ reflection from $\pi^+\pi^-\pi^0$. This parameterization was used in a mass fitting routine using the CERN library program MINUIT [56] to minimise the χ^2 value in the region from the $\pi^+\pi^-$ threshold mass to 2.2 GeV.

Using this parameterization, a typical fit is shown in figure 4.10. It is clear from figure 4.10 that the fit is poor, especially around the $\mathrm{f}_0(980)$ mass region. The background parameterization does not vary steeply enough to take into account the extremely rapid decrease of phase space in this region. Several ideas were employed

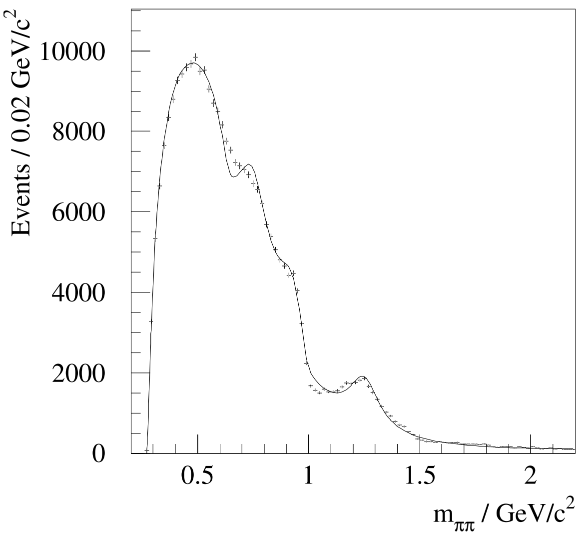

Figure 4.10: Fit to the mass spectrum.

in order to take the $f_0(980)$ drop into account. Convoluting the $f_0(980)$ region with a Gaussian of width 10 MeV to represent the experimental resolution did not produce a significant improvement. Introducing interference terms between the $f_2(1270)$ and the $f_2'(1525)$ (which has a strong coupling to the related $K\overline{K}$ channel) made a reasonable fit impossible. It was thought possible that introducing an incoherent free Breit–Wigner function at $\sim$1.1 GeV with width $\sim$200 MeV could decrease the background around the $f_0(980)$ region, but this also made the fit impossible. The same was found if an incoherent Breit–Wigner was introduced at a lower mass of $\sim$0.8 GeV.

However, it may be supposed that the background at low mass will have a large S-wave component (see chapter 6 for confirmation of this expectation). Therefore, it might be expected that the background will interfere coherently with other spin 0 objects. In order to take this into account in the parameterization, the substitution

$$1 + A_{f_0(980)}|F_\pi(m)|^2 \rightarrow |1 + A_{f_0(980)}F_\pi(m)e^{i\delta_1}|^2 = B_{f_0(980)}$$

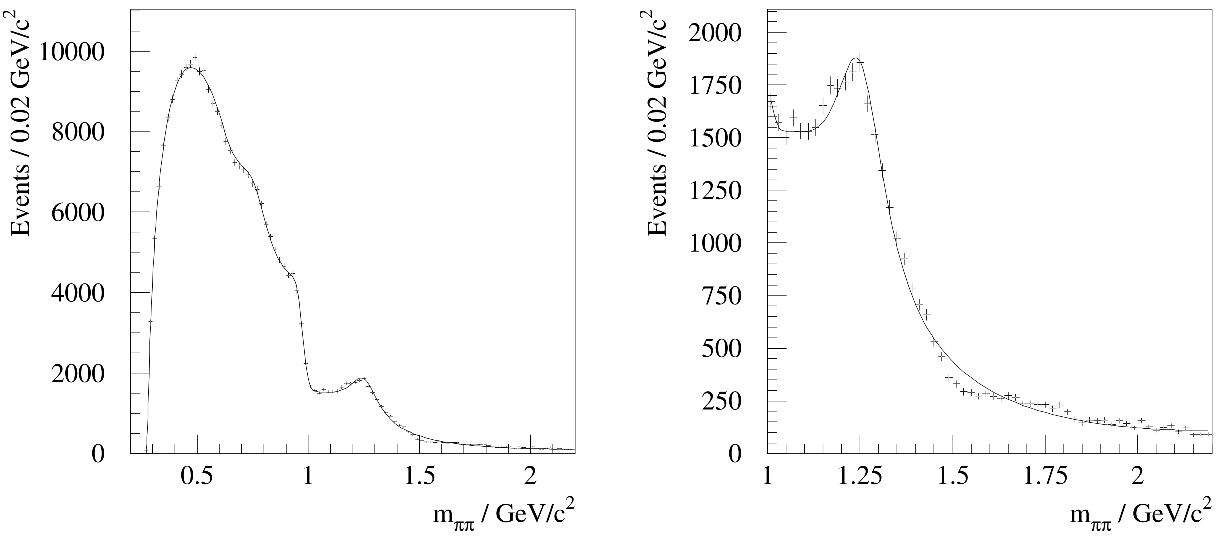

(a) Fit with interference

(b) Expanded view

Figure 4.11: Fit to the $\pi^+\pi^-$ mass spectrum using interfering formalism.

is made, where δ_1 represents the phase angle describing the interference between the $f_0(980)$ and the S-wave background. This parameterization gives a good fit at both low mass and the 1 GeV/c^2 region. However, it suffers from a poor χ^2 around $\sim$1.5 GeV, as may be seen in figures 4.11 a and b. In common with the parameterization used by WA76 [43], a further S-wave interference term is introduced with another Breit–Wigner function of mass 1.472 GeV/c^2 and width 195 MeV/c^2. The S-wave term is then

$$B_{f_0(980)} \rightarrow |1 + A_{f_0(980)} F_\pi(m) e^{i\delta_1} + A_X F_X e^{i\delta_2}|^2,$$

where A_X, F_X are the amplitude and shape respectively of the Breit–Wigner function described above, and δ_2 is the phase angle describing the interference. Using this formalism, the fit shown in figures 4.12 a and b is obtained. The χ^2 per degree of freedom using this parameterization is $\sim$ 104/81.

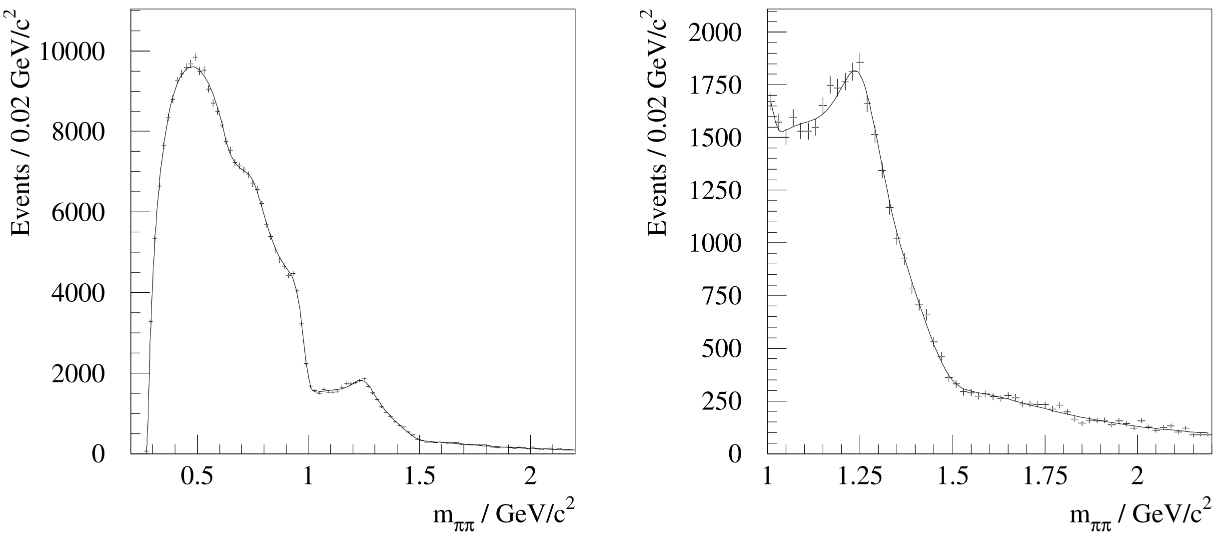

(a) Fit to whole mass spectrum

(b) Expanded view

Figure 4.12: Fit to the $\pi^+\pi^-$ mass spectrum using interfering formalism and term at ~ 1500 MeV$/c^2$.

If the parameters of the state at $\sim$ 1500 MeV$/c^2$ are left free, the χ^2 per degree of freedom is found to be $\sim 104/79$, and the fit parameters for the new state are $m = 1490 \pm 10$ and $\Gamma = 150 \pm 25$.

The final fit parameters are shown in table 4.1.

In the complex s plane, the poles of the $\mathrm{f}_0(980)$ are given by

$$m^2_{\mathrm{f}_0(980)} - s - i m_{\mathrm{f}_0(980)}\Gamma = 0.$$

This has more than one solution depending on the signs of the imaginary parts of the breakup momenta to $\pi^+\pi^-$ and $\mathrm{K\overline{K}}$ in the expressions for Γ_π and Γ_K (*i.e.*, the square roots in these expressions lead to more than one solution). By convention [57], sheet II is taken to be the sheet on the complex s plane which has the imaginary part of the breakup momentum to $\mathrm{K\overline{K}}$ positive, and sheet III has the imaginary part

Table 4.1: The parameters for the fitted $\pi^+\pi^-$ mass spectrum.

Fit Parameter	Value
α	0.62 ± 0.01
β	(4.4 ± 0.1) GeV$^{-1}c^2$
γ	$(-0.3 \pm 0.3\ )$ GeV$^{-2}c^4$
A_ρ	0.04 ± 0.03
A_{f_2}	0.15 ± 0.01
A_{S^*}	0.13 ± 0.01
A_X	0.025 ± 0.001
A_ω	$(7.5 \pm 0.7)\times 10^{-6}$
δ_1	$(13 \pm 4)^\circ$
δ_2	$(50 \pm 2)^\circ$
$m_{\mathrm{f_0(980)}}$	(0.978 ± 0.005) GeV$/c^2$
g_π	(0.20 ± 0.01) GeV$/c^2$
g_K	(0.1 ± 0.1) GeV$/c^2$
m_{1500}	(1.49 ± 0.01) GeV$/c^2$
Γ_{1500}	(0.15 ± 0.025) GeV$/c^2$

of the breakup momentum to $K\overline{K}$ negative. In this convention, the sheet II pole of the $f_0(980)$ is calculated to be $((982 \pm 2) - i(42 \pm 2))$ MeV/c^2, and the sheet III pole $((969 \pm 2) - i(51 \pm 2))$. The width is given by twice the imaginary part of the sheet II pole [43], giving $\Gamma = 84 \pm 4$ MeV/c^2. These values are consistent with the $f_0(980)$ parameters quoted by the Particle Data Group [4], although they note that the width determination is highly model dependent.

WA76 found it necessary to include a contribution from the $f_J(1710)$. However, for the WA91 data, there appears to be little activity in this mass region. Including a term to represent the $f_J(1710)$ does not result in any significant improvements to the fit quality.

It is interesting to note that the WA76 Collaboration used the formalism discussed here to fit the $\pi^+\pi^-$ mass spectra from the AFS Experiment and from hadronic J/ψ decay, with the parameters of the 1500 MeV/c^2 state fixed. They found good agreement with the data in both cases.

4.4 Conclusions

It has been shown that in order to obtain a good fit to the WA91 $\pi^+\pi^-$ mass spectrum, a formalism must be used in which the S-wave contributions to the spectrum interfere coherently. In effect, this results in an interference between the phase space background (supposed to be spin 0), the $f_0(980)$ and another Breit-Wigner function with parameters consistent with the $f_0(1500)$.

Ideally, however, in order to fully describe the properties of the states observed, a partial wave analysis must be performed in order to extract in particular the S-wave. This will enable the $f_0(980)$ and 1500 MeV/c^2 state to be examined, without interferences from other resonances. The formalism used in order to do this is described in chapter 5, and the application of this parameterization is given in chapter 6.

Chapter 5

A Partial Wave Analysis of the 1992 $\pi^+\pi^-$ Data

5.1 Introduction

The angular distribution of the decay products in any specific reaction is determined by the spin quantum numbers of the resonances and backgrounds involved in that process. Spin 0 states will in general decay isotropically in their centre-of-mass; higher spin states will decay according to some more complicated angular distribution. If it is understood how an object of a specific spin decays, then in principle the spin of that object may be determined from the angular distribution of its decay products. However, the situation is generally complicated by interferences between resonances and background terms, or between several resonances, which may be of different widths. For systems such as $\pi^+\pi^-$ in central production, the complications may be to some extent overcome by performing a Partial Wave Analysis (PWA) [58], that is the average is taken over the incoming spin states and the sum is taken over the outgoing spin states involved in the interaction in order to produce an expression for the angular distribution.

Although such analyses have been discussed in detail (*e.g.*, [59]), there is comparitively little literature on the application of PWA to centrally produced 2-body channels, and much of the following work will appear in [60].

5.2 Choice of Axes

The choice of axes for a PWA of central production reactions is more complicated than the usual choices made for peripheral reactions, such as the so-called Gottfried-Jackson axes [61]. In the peripheral case it is easier to define a plane which contains the 3-momenta of all the particles being considered, but for reactions such as $\mathrm{pp} \longrightarrow \mathrm{p}_f(\pi^+\pi^-)\mathrm{p}_s$ there is no plane which will in general contain the 3-momenta of all the particles. However, the problem may be simplified by considering the reaction

$$ab \longrightarrow M, \tag{5.1}$$

where a and b represent the exchange particles and M represents the $\pi^+\pi^-$ system (M could be used to represent any 2-body central system). The momenta $\mathbf{p}_a$ and $\mathbf{p}_b$ are trivially defined by the momentum change at each vertex. In the (ab) rest frame, the vectors $\mathbf{p}_a$, $\mathbf{p}_b$, $\mathbf{p}_{\pi^+}$ and $\mathbf{p}_{\pi^-}$ are coplanar, and it is thus possible to define a set of axes.

The z-axis is chosen to be along the direction of $\mathbf{p}_b$. In principle it is irrelevant whether a or b is chosen to define this axis, but in practice the slow vertex is better measured than the fast. For the same reason, the y-axis is defined to be $\mathbf{p}_{ab} \times \mathbf{p}_s$, and then x is defined by $\hat{\mathbf{x}} = \hat{\mathbf{y}} \times \hat{\mathbf{z}}$. This is illustrated in figure 5.1.

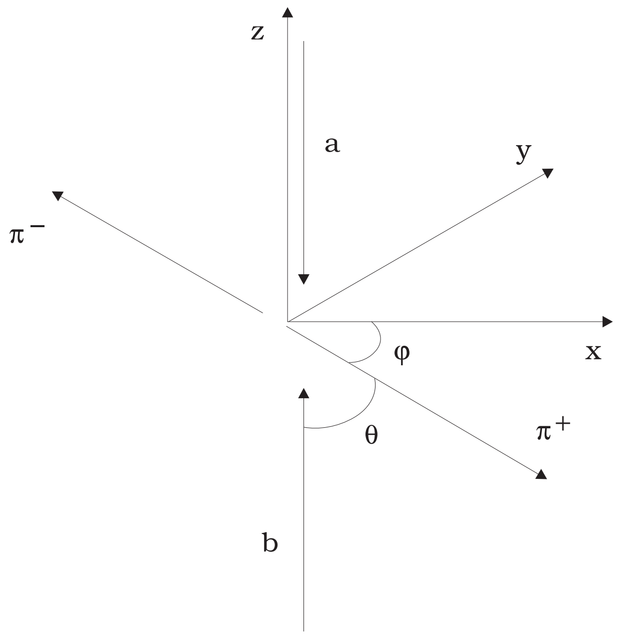

Figure 5.1: Definition of axes for partial wave analysis.

5.3 Helicity Amplitudes

The amplitudes for equation 5.1 may be written as

$$\mathbf{f}^{J_a J_b}_{\lambda_a \lambda_b} = \langle \theta, \phi | U | \mathbf{p}_a, J_a, \lambda_a; \mathbf{p}_b, J_b, \lambda_b \rangle, \tag{5.2}$$

where θ and ϕ represent the scattering angles (figure 5.1) for the decay of M, and $\mathbf{p}_i$, J_i and λ_i represent the momentum, spin and helicity of the exchange particle i. Equation 5.2 may be expanded in terms of the angular momentum states, J and Λ, of M, that is the basis of equation 5.2 is changed by writing

$$\mathbf{f}^{J_a J_b}_{\lambda_a \lambda_b} = \langle \theta, \phi | J, \Lambda \rangle \langle J, \Lambda | U | \mathbf{p}_a, J_a, \lambda_a; \mathbf{p}_b, J_b, \lambda_b \rangle. \tag{5.3}$$

The overlap integrals are given by

$$\langle \theta, \phi | J, \Lambda \rangle = \sqrt{\frac{2J+1}{4\pi}} \mathcal{D}^{(J)*}_{\Lambda\ 0}(\phi, \theta, -\phi), \tag{5.4}$$

where the $\mathcal{D}^{(J)*}_{\Lambda\ 0}(\phi, \theta, -\phi)$ are the Wigner-$\mathcal{D}$ functions (see, *e.g.*, [62, 63]). Then

$$\mathbf{f}^{J_a J_b}_{\lambda_a \lambda_b} = \sum_{J,\Lambda} \sqrt{\frac{2J+1}{4\pi}} \mathcal{D}^{(J)\ *}_{\Lambda\ 0}(\phi, \theta, -\phi) \langle J, \Lambda | U | \mathbf{p}_a, J_a, \lambda_a; \mathbf{p}_b, J_b, \lambda_b \rangle, \tag{5.5}$$

and the intensity $I(\Omega)$, where Ω represents (θ, ϕ) will be given by

$$I(\Omega) = \sum_{J_a, \lambda_a} \frac{1}{n_{J_a}} \sum_{J_b, \lambda_b} \frac{1}{n_{J_b}} (\mathbf{f}^{J_a J_b}_{\lambda_a \lambda_b}\ \mathbf{f}^{J_a J_b\ *}_{\lambda_a \lambda_b}), \tag{5.6}$$

where n_J is 1 if $J = 0$ and n_J is 3 if $J \geq 1$. Note that at this point the assumption is made that the helicities can be only 0 (proton non-spin flip) or 1 (proton spin-flip). Expanding this in terms of the amplitudes given by 5.5,

$$\begin{aligned} I(\Omega) &= \sum_{\substack{J_a, \lambda_a \\ J_b, \lambda_b}} \frac{1}{n_{J_a} n_{J_b}} \sum_{\substack{J\ , \Lambda \\ J', \Lambda'}} \frac{\sqrt{(2J+1)(2J'+1)}}{4\pi} \mathcal{D}^{(J)*}_{\Lambda\ 0}(\Omega) \mathcal{D}^{(J')}_{\Lambda'\ 0}(\Omega) \times \\ & \langle J, \Lambda | U | \mathbf{p}_a, J_a, \lambda_a; \mathbf{p}_b, J_b, \lambda_b \rangle \langle \mathbf{p_a}, J_a, \lambda_a; \mathbf{p_b}, J_b, \lambda_b | U | J', \Lambda' \rangle. \end{aligned} \tag{5.7}$$

The density matrix for the interaction is defined by

$$\rho^{JJ'}_{\Lambda\Lambda'} = \sum_{\substack{J_a, \lambda_a \\ J_b, \lambda_b}} \frac{1}{n_{J_a} n_{J_b}} \langle J, \Lambda | U | \mathbf{p}_a, J_a, \lambda_a; \mathbf{p}_b, J_b, \lambda_b \rangle \langle \mathbf{p_a}, J_a, \lambda_a; \mathbf{p_b}, J_b, \lambda_b | U | J', \Lambda' \rangle, \tag{5.8}$$

and it follows that

$$I(\Omega) = \sum_{\substack{J,\Lambda \\ J',\Lambda'}} \sqrt{\frac{(2J+1)(2J'+1)}{4\pi}} \mathcal{D}^{(J)*}_{\Lambda\ 0}(\Omega)\mathcal{D}^{(J')}_{\Lambda'\ 0}(\Omega)\rho^{JJ'}_{\Lambda\Lambda'}. \tag{5.9}$$

Thus the intensity of the decay products is parameterized as a function of Ω.

5.4 Parity Constraints

At this stage, a choice of phase is required which describes the eigenstates of the parity operator. Following the convention of Jacob and Wick [64], the parity operator $\mathbf{P}$ acts on a helicity state $|J, \Lambda\rangle$ such that

$$\mathbf{P}|J,\Lambda\rangle = \eta_J(-1)^{J-\Lambda}e^{i\pi J_y}|J,-\Lambda\rangle, \tag{5.10}$$

while for the Hermitian conjugate,

$$\langle J,\Lambda|\mathbf{P}^\dagger = \langle J,-\Lambda|\frac{1}{\eta_J}(-1)^{\Lambda-J}e^{-i\pi J_y}, \tag{5.11}$$

and for a two particle state $|J_a, \lambda_a; J_b, \lambda_b\rangle$,

$$\mathbf{P}|J_a,\lambda_a;J_b,\lambda_b\rangle = \eta_a\eta_b(-1)^{J_a+J_b-\lambda_a+\lambda_b}e^{i\pi J_y}|J_a,-\lambda_a;J_b,-\lambda_b\rangle. \tag{5.12}$$

Combining equations 5.12 and 5.11 gives

$$\langle J,\Lambda|\mathbf{P}^\dagger U\mathbf{P}|J_a,\lambda_a;J_b,\lambda_b\rangle = \frac{\eta_a\eta_b}{\eta_J}(-1)^{\Lambda-J+J_a+J_b-\lambda_a+\lambda_b}\langle J,-\Lambda|U|J_a,-\lambda_a;J_b,-\lambda_b\rangle. \tag{5.13}$$

Parity conservation implies that

$$\mathbf{P}^\dagger U\mathbf{P} = U = \mathbf{P}^{-1}U\mathbf{P}, \tag{5.14}$$

since $\mathbf{P}$ is a unitary operator. Hence defining $h^{JJ_aJ_b}_{\Lambda\lambda_a\lambda_b}$ as $\langle J,\Lambda|U|J_a,\lambda_a;J_b,\lambda_b\rangle$, then

$$h^{JJ_aJ_b}_{\Lambda\lambda_a\lambda_b} = \frac{\eta_a\eta_b}{\eta_J}(-1)^{J_a+J_b-J+\Lambda+(\lambda_b-\lambda_a)}h^{\,J\ \ J_a\ \ J_b}_{-\Lambda-\lambda_a-\lambda_b}. \tag{5.15}$$

Equation 5.15 can be simplified by noting that in the (ab) rest frame, $\Lambda = \lambda_a - \lambda_b$. Furthermore, defining the *naturality* of the exchange such that

$\eta = (-1)^J$ corresponds to *natural* parity exchange, while

$\eta = (-1)^{J+1}$ corresponds to *unnatural* parity exchange,

then for natural-natural (or unnatural-unnatural) exchange, the product $\eta_a\eta_b(-1)^{J_a+J_b}$ must be positive, while for natural-unnatural exchange $\eta_a\eta_b(-1)^{J_a+J_b}$ must be negative. If these conditions are put into 5.15, then

$$h^{JJ_aJ_b}_{\Lambda\lambda_a\lambda_b} = +h^{\,J\ \ J_a\ \ J_b}_{-\Lambda-\lambda_a-\lambda_b}, \tag{5.16}$$

for natural-natural or unnatural-unnatural exchange, and

$$h^{JJ_aJ_b}_{\Lambda\lambda_a\lambda_b} = -h^{\,J\ \ J_a\ \ J_b}_{-\Lambda-\lambda_a-\lambda b} \tag{5.17}$$

for natural-unnatural exchange. This may now be applied to the density matrix elements, where for natural-natural (or unnatural-unnatural) exchange

$$\begin{aligned}
\rho^{JJ'}_{\Lambda\Lambda'} &= \sum_{\substack{J_a,\lambda_a\\ J_b,\lambda_b}} \frac{1}{n_{J_a}n_{J_b}}\langle J,\Lambda|U|\mathbf{p}_a,J_a,\lambda_a;\mathbf{p}_b,J_b,\lambda_b\rangle\langle\mathbf{p_a},J_a,\lambda_a;\mathbf{p_b},J_b,\lambda_b|U|J',\Lambda'\rangle \\
&= \sum_{\substack{J_a,\lambda_a\\ J_b,\lambda_b}} \frac{1}{n_{J_a}n_{J_b}}\langle J,-\Lambda|U|\mathbf{p}_a,J_a,-\lambda_a;\mathbf{p}_b,J_b,-\lambda_b\rangle \times \\
&\quad \langle\mathbf{p_a},J_a,-\lambda_a;\mathbf{p_b},J_b,-\lambda_b|U|J',-\Lambda'\rangle \\
&= \rho^{\,J\ \ J'}_{-\Lambda-\Lambda'}.
\end{aligned} \tag{5.18}$$

For natural-unnatural exchange, 5.17 requires that all terms with $\Lambda = \lambda_a = \lambda_b = 0$ vanish.

5.5 Moments

Equation 5.9 may be rewritten by using the identity

$$\mathcal{D}_{\Lambda 0}^{(J)*}(\Omega)\ \mathcal{D}_{\Lambda' 0}^{(J')}(\Omega) = \sum_{L(M)} (-1)^{\Lambda'} C_{\Lambda\, -\Lambda'\, M}^{J\ \ J'\, L}\ C_{0\,0\,0}^{JJ'L}\ \mathcal{D}_{M0}^{(L)*}(\Omega) \tag{5.19}$$

where the $C_{\Lambda\Lambda' M}^{JJ'L}$ are Clebsch-Gordan coefficients. This gives

$$I(\Omega) = \sum_{\substack{J\,,\Lambda\\ J',\Lambda'}} \sum_{L(M)} \frac{\sqrt{(2J+1)(2J'+1)}}{4\pi} (-1)^{\Lambda'} C_{\Lambda\, -\Lambda'\, M}^{J\ \ J'\, L}\ C_{0\,0\,0}^{JJ'L}\ \mathcal{D}_{M0}^{(L)*}(\Omega) \rho_{\Lambda\Lambda'}^{JJ'}. \tag{5.20}$$

For the case of natural-natural exchange with zero helicity, this simplifies to

$$I(\Omega) = \sum_{\substack{JJ'\\ L}} \frac{\sqrt{(2J+1)(2J'+1)}}{4\pi} (C_{0\,0\,0}^{JJ'L})^2 \mathcal{D}_{00}^{(L)*}(\Omega) \rho_{\Lambda\Lambda'}^{JJ'}. \tag{5.21}$$

Furthermore, the *CP* of the initial state is positive, and hence *CP* conservation for $\pi^+\pi^-$, $\mathrm{K}^+\mathrm{K}^-$, *etc.*, implies that the final state must have J^{PC} =(even)$^{++}$. Hence

$$\begin{aligned} I(\Omega) &= \frac{1}{4\pi}\{\mathcal{D}_{00}^{(0)*}(\Omega)\rho_{00}^{00} + \sqrt{5}[(C_{000}^{202})^2\mathcal{D}_{00}^{(2)*}(\Omega)\rho_{00}^{20} + (C_{000}^{022})^2\mathcal{D}_{00}^{(2)*}(\Omega)\rho_{00}^{02}] \\ &+ 5[(C_{000}^{220})^2\mathcal{D}_{00}^{(0)*}(\Omega)\rho_{00}^{22} + (C_{000}^{222})^2\mathcal{D}_{00}^{(2)*}(\Omega)\rho_{00}^{22} \\ &+ (C_{000}^{224})^2\mathcal{D}_{00}^{(4)*}(\Omega)\rho_{00}^{22}]\}, \end{aligned} \tag{5.22}$$

and using $\mathcal{D}_{00}^{(0)*}(\Omega) = 1$ and $\rho_{00}^{20} + \rho_{00}^{02} = 2\mathrm{Re}\rho_{00}^{22}$, this gives

$$I(\Omega) = \frac{1}{4\pi}(\rho_{00}^{00} + 2\sqrt{5}\mathcal{D}_{00}^{(2)}(\Omega)2\mathrm{Re}\rho_{00}^{20} + 5(\mathcal{D}_{00}^{(2)}(\Omega))^2\rho_{00}^{22}), \tag{5.23}$$

since the $\mathcal{D}^{(J)}_{00}(\Omega)$ are real.

This approach is applicable at very high energies where the production mechanism should be essentially pure DPE. However, in the more general case of $J \leq 2, |\Lambda| \leq 1$, the procedure becomes more complicated. To overcome this, the method of moments may be used. The moments $H(L,M)$ are defined as being the expectation values of $\mathcal{D}^{(L)}_{M0}(\Omega)$, that is,

$$H(L,M) \equiv \left\langle \mathcal{D}^{(L)}_{M0}(\Omega) \right\rangle = \int I(\Omega)\mathcal{D}^{(L)}_{M0}(\Omega)d\Omega. \tag{5.24}$$

These are determined experimentally as

$$H(L,M) = \sum_{i=1}^{N} \mathcal{D}^{(L)}_{M0}(\Omega_i)acc_i^{-1}, \tag{5.25}$$

where acc_i is the acceptance in that bin. Using the orthogonality of the $\mathcal{D}^{(L)}_{M0}(\Omega)$,

$$\int \mathcal{D}^{j*}_{mm'}(\Omega)\mathcal{D}^{J}_{Mm'}(\Omega)d\Omega = \frac{4\pi}{(2J+1)}\delta_{jJ}\delta_{mM}\delta_{m'M'}, \tag{5.26}$$

substituting into 5.20 and 5.24 gives

$$H(L,M) = \sum_{\substack{J,J' \\ \Lambda,\Lambda'}} (-1)^{\Lambda'} C^{J\ \ J'L}_{\Lambda -\Lambda' M} C^{JJ'L}_{0\ 0\ 0} \frac{\sqrt{(2J+1)(2J'+1)}}{(2L+1)} \rho^{JJ'}_{\Lambda\Lambda'}. \tag{5.27}$$

Using this form for the moments, a set of coefficients for each of the density matrix elements may be calculated. Only moments with $M \geq 0$ need be considered as independent, since

$$H(L,M) + (-1)^M H(L,-M) = 2\mathrm{Re}H(L,M). \tag{5.28}$$

The parity conditions 5.18 are applied. This leads to the parameterization shown in equations 5.29.

$$\boxed{\begin{aligned} H(0,0) &= \rho^{00}_{00} + \rho^{11}_{00} + \rho^{22}_{00} + 2\rho^{11}_{11} + 2\rho^{22}_{11} \\ H(1,0) &= 1.1548\rho^{01}_{00} + 1.7888\rho^{12}_{11} + 1.0328\rho^{12}_{00} \\ H(2,0) &= 0.8944\rho^{02}_{00} - 0.4\rho^{11}_{11} + 0.4\rho^{11}_{00} + 0.2858\rho^{22}_{11} + 0.2858\rho^{22}_{00} \\ H(2,2) &= -0.4899\rho^{11}_{1-1} - 0.3499\rho^{22}_{1-1} \\ H(3,0) &= -0.7688\rho^{12}_{11} + 0.6640\rho^{12}_{00} \\ H(3,2) &= -0.6998\rho^{12}_{1-1} \\ H(4,0) &= 0.2857\rho^{22}_{00} - 0.381\rho^{22}_{11} \\ H(4,2) &= -0.3012\rho^{22}_{1-1}. \end{aligned} \qquad (5.29)}$$

5.6 Phase Coherence

If phase coherence [65] is assumed, that is that all the amplitudes giving rise to a given J,Λ are coherent (as might be expected if they are all associated with a common production mechanism), and therefore their sum can be written as

$$\rho^{JJ'}_{\Lambda\Lambda'} = \sum_{\substack{J_a,\lambda_a \\ J_b,\lambda_b}} (1 + \epsilon^{J_a J_b}_{\lambda_a \lambda_b}(J,\Lambda)) h^J_\Lambda h^{J'*}_{\Lambda'}, \tag{5.30}$$

then the indices $J_a, \lambda_a, J_b, \lambda_b$ in expression 5.5 can be dropped. Thus equations 5.29 may be rewritten as

$$
\boxed{\begin{aligned}
H(0,0) &= |S_0|^2 + |P_0|^2 + |D_0|^2 + 2|P_{+1}|^2 + 2|D_{+1}|^2 \\
H(1,0) &= 1.1548 S_0 P_0^* + 1.7888 P_{+1} D_{+1}^* + 1.0328 P_0 D_0^* \\
H(2,0) &= 0.8944 S_0 D_0^* - 0.4|P_{+1}|^2 + 0.4|P_0|^2 + 0.2858|D_1|^2 + 0.2858|D_0|^2 \\
H(2,2) &= -0.4899 P_{+1} P_{-1}^* - 0.3499 D_{+1} D_{-1}^* \qquad (5.31) \\
H(3,0) &= -0.7688 P_{+1} D_{+1}^* + 0.6640 P_0 D_0^* \\
H(3,2) &= -0.6998 P_{+1} D_{-1}^* \\
H(4,0) &= 0.2857|D_0|^2 - 0.381|D_{+1}|^2 \\
H(4,2) &= -0.3012 D_{+1} D_{-1}^*.
\end{aligned}}
$$

S_0, P_0 and D_0 refer to the helicity 0 spin 0, 1 and 2 waves respectively, and $P_{\pm 1}$, $D_{\pm 1}$ refer to the helicity ± 1 spin 1 and 2 waves respectively. In practice, this means that there are 8 moments to fit, but 14 free parameters (real and imaginary parts of S_0, P_0, D_0, P_{+1}, P_{-1}, D_{+1}, D_{-1}). Since the overall phase cannot be determined, one reference phase may be chosen in the definition of the complex quantities. In an attempt to further reduce the number of free parameters, a similar method is followed to that used by Estabrooks and Martin [66] in fitting the moments for peripheral reactions. Here, since the helicity $+1$ and helicity -1 amplitudes are expected to be small (supposing that the $\pi^+\pi^-$ channel is dominated by S wave), then $P_{+1} \sim P_{-1} = P_1$ and $D_{+1} \sim D_{-1} = D_1$. Furthermore, the phases are chosen such that D_0 and D_1 are both real, and P_0 and P_1 both have the same phase, ϕ_P, relative to the D-wave. The phase of the S-wave is denoted ϕ_S.

This means that a fit may now be performed to seven free parameters, $|S_0|$, $|P_0|$, $|D_0|$, $|P_1|$, $|D_1|$, ϕ_S and ϕ_P, in each mass bin using the measured values of $H(0,0)$, $H(1,0)$, $H(2,0)$, $H(2,2)$, $H(3,0)$, $H(3,2)$, $H(4,0)$ and $H(4,2)$.

5.7 Fit Ambiguities

In performing the fits to the mass bins, an ambiguity arises that results in fits of equivalent quality being produced for different values of the S and P-waves [67]. To see how this occurs, consider equation 5.5 rewritten with the phase coherence assumption explicit, that is,

$$\mathbf{f} = \sqrt{\frac{1}{4\pi}}S_0 + \sqrt{\frac{3}{4\pi}}P_0 z + \frac{1}{2}\sqrt{\frac{5}{4\pi}}D_0(3z^2 - 1), \tag{5.32}$$

where $z = \cos\theta$ and the $\mathcal{D}$ matrix elements are written in full. Note that the helicity one terms are are assumed to be negligible; a full analysis including the helicity one terms leads to further ambiguities, but this is unnecessary in this simplified case, since the helicity one terms have already been assumed to be small in order to reduce the number of free parameters.

Now $\mathbf{f}$ may be written as

$$\begin{aligned} \mathbf{f} &= a_0 + a_1 z + \frac{1}{2}a_2(3z^2 - 1) & (5.33) \\ &= \frac{3}{2}a_2 z^2 + a_1 z + (a_0 - \frac{1}{2}a_2). & (5.34) \end{aligned}$$

Since this is just a polynomial in z, it could be written in terms of its roots, z_i, *i.e.*,

$$\mathbf{f} = c\prod_{i=1}^{L}(z - z_i), \tag{5.35}$$

with c complex. For $L \leq 2$ the zeros are given by

$$z_{1,2} = \frac{-a_1 \pm \sqrt{a_1^2 - 4(\frac{3}{2}a_2(a_0 - \frac{1}{2}a_2))}}{2(\frac{3}{2}a_2)}. \tag{5.36}$$

However, it is not $\mathbf{f}$ that is observable, but the differential cross section, $\frac{d\sigma}{d\Omega}$, which is given by

$$\frac{d\sigma}{d\Omega} \sim |\mathbf{f}|^2 = |c|^2 \prod_{i=1}^{L} (z - z_i)(z - z_i^*). \tag{5.37}$$

This expression is clearly invariant under $z_i \longrightarrow z_i^*$, and hence it is not possible to know *a priori* which zero (z_i or z_i^*) is the correct one to associate with $\mathbf{f}$. Thus a new set of solutions for $\mathbf{f}$ can be written by swapping, for example, z_1^* for z_1. This leads to

$$\begin{aligned} \mathbf{f} &= c(z - z_1^*)(z - z_2) & (5.38)\\ &= cz_1^* z_2 - c(z_1^* + z_2)z + cz^2. & (5.39)\\ & & (5.40) \end{aligned}$$

Now since $\mathcal{D}_{00}^{(0)}(\alpha,\beta,\gamma) = 1$, $\mathcal{D}_{00}^{(1)}(\alpha,\beta,\gamma) = z$ and $\mathcal{D}_{00}^{(2)}(\alpha,\beta,\gamma) = \frac{1}{2}(3z^2 - 1)$, it follows that

$$\begin{aligned} \mathbf{f} &= cz_1^* z_2 \mathcal{D}_{00}^{(0)} - c(z_1^* + z_2)\mathcal{D}_{00}^{(1)} + c(\frac{2}{3}\mathcal{D}_{00}^{(2)} + \frac{1}{3}) & (5.41)\\ &= \frac{2}{3} c\mathcal{D}_{00}^{(2)} - c(z_1^* + z_2)\mathcal{D}_{00}^{(1)} + c(z_1^* z_2 + \frac{1}{3})\mathcal{D}_{00}^{(0)}. & (5.42) \end{aligned}$$

Comparing this with our original expression for $\mathbf{f}$ leads us to conclude that a new set of amplitudes,

$$\begin{aligned} S_0' &= \sqrt{4\pi} c(z_1^* z_2 + \frac{1}{3}) & (5.43)\\ P_0' &= -\sqrt{\frac{4\pi}{3}} c(z_1^* + z_2) & (5.44)\\ D_0' &= \frac{2}{3}\sqrt{\frac{4\pi}{5}} c, & (5.45) \end{aligned}$$

can be generated which will provide identical values of $|\mathbf{f}|^2$ and hence identical fits to the angular distribution.

In this method, D_0 will not change, because it has been chosen to be real. However, the S_0 and P_0 waves can alter (although unitarity implies that $|S_0'|^2 + |P_0'|^2 = |S_0|^2 + |P_0|^2$). In general, this will lead to 4 solutions, *i.e.*, $z_1, z_2 \longrightarrow z_1, z_2$, $z_1 \longrightarrow z_1^*$, $z_2 \longrightarrow z_2^*$, $z_1, z_2 \longrightarrow z_1^*, z_2^*$, all of which provide identical fits. However, only two of these are independent, since the remaining pair can be trivially obtained by complex conjugation.

Note that, since in the PWA formalism the helicity one amplitudes are included, a full ambiguity analysis would lead to further ambiguities. However, since the helicity one amplitudes have been assumed to be small, it is only necessary to calculate the ambiguous solutions using the method discussed above. In mass bins where the helicity one waves are non-zero, the ambiguity will in general be resolved (*i.e.*, the solutions generated above will not provide identical fits to the moments). However, in bins where the helicity one terms are close to zero, the ambiguous solutions will provide very similar fits to the moment distributions. The appropriate solution is chosen by using the following prescription.

1. Find one set of solutions, S_0, P_0, D_0, P_1, D_1, ϕ_S, ϕ_P, by fitting the moments.
2. Generate new S_0 and P_0 solutions (by making the substitution $z_1 \longrightarrow z_1^*$, for example).
3. Constrain the parameters to vary by small amounts and refit.
4. If this fit is better than the original fit, then assume the new parameters are the correct values, otherwise allow the fit to return to the old values.

5.8 Conclusions

In summary, a new method has been developed of parameterizing the angular distribution of the centrally produced $\pi^+\pi^-$ channel in terms of the partial waves. The parity constraints for this case have been determined, and these have been included in the parameterization. Furthermore, a discussion has been given of the problem of ambiguities in the fitted parameters which means that another set of solutions can be generated which provide the same (in the case of pure helicity 0) or very similar (in the case of small helicity 1 amplitudes) fits to the moments. This now allows a fit to the angular distribution for WA91 data to be performed, and this is discussed further in chapter 6.

Chapter 6

The 1992 $\pi^+\pi^-$ Angular Distribution and Fit

In this chapter, the application of the formalism described in chapter 5 to the 1992 $\pi^+\pi^-$ data is discussed. It was noted in chapter 3 that the data taken during the 1992 run were classified by the directions taken by the outgoing protons into four trigger types, namely

slow proton left, fast proton left (LL),
slow proton right, fast proton right (RR),
slow proton right, fast proton left (RL),
slow proton left, fast proton right (LR).

Since the majority of the 1992 data are LL triggers, and since the trigger type can have an effect on the states observed in the $\pi^+\pi^-$ mass spectrum (see chapter 7), only the LL trigger types are discussed here.

Using the axes discussed in chapter 5, a set of angular distributions are produced as a function of mass. The definition of the polar angles θ and ϕ is shown in figure 5.1. For each event, θ and ϕ are calculated and then each event is weighted by the reciprocal of the acceptance for that event.

6.1 Calculation of Acceptance Weight

In order to calculate the appropriate weight for each event, it is necessary to simulate a data set. A "traditional" Monte Carlo method could be applied to do this, *i.e.*, a simulation where a model is used to describe the exchange processes in central production and tracks are generated at random according to this formalism. However, although such models exist (*e.g.*, [68]), it is unclear how to incorporate DPE, Reggeon-Reggeon and Reggeon-Pomeron exchange into a single description of central production. Furthermore, trial runs using the CERN routine FOWL [69] and a formalism to describe DPE only [68] were found to take prohibitively long runs of computer time, but with limited statistics the results were found to be essentially the same as those from the method discussed below.

A sample of events is generated by taking a sample of 30,000 real events and choosing one beam and two fast tracks at random from different events in this sample, *i.e.,* a beam from one event, a p_f from another event and a second p_f from another event are chosen. The second fast track is used to simulate a slow track. This is because in the experimental data the slow proton momentum spectrum does not extend to 0, since the reconstructed slow track must have sufficient momentum to leave the target (typically, this means that the slow track must have $|p| > 0.3$ GeV/c, as may be seen from the plot of reconstructed slow proton momentum shown in figure 6.1). Since it is required in the simulation that the fast and slow t-distributions are the same at input, slow tracks are simulated by transforming fast tracks into the centre-of-mass rest frame, reversing the three-momentum components of the resultant vector, and then boosting back to the lab frame. The combined tracks are then rotated around the beam axis by random polar angles, ϕ_i.

A $\pi^+\pi^-$ system is then made in such a way as to balance momentum and energy

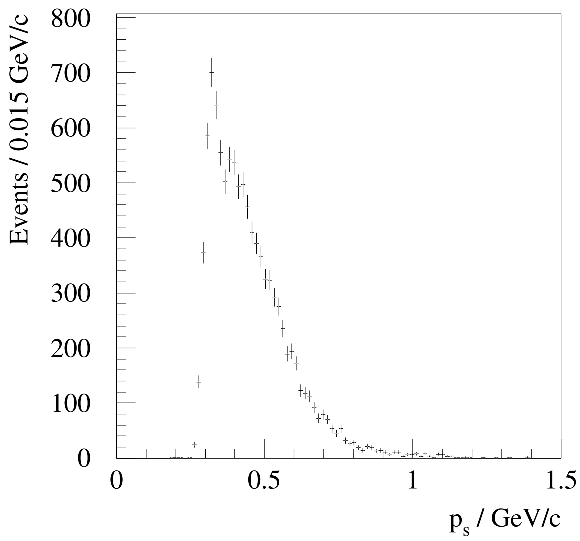

Figure 6.1: Reconstructed slow proton momentum.

exactly, assuming that the target proton is at rest in the laboratory system. If there is not enough available energy in this event to give an invariant mass greater than or equal to the mass of two pions, then the event is rejected at this point. The $\pi^+\pi^-$ system is decayed isotropically in its rest frame, and then the resulting tracks are boosted back to the centre-of-mass frame and then to the laboratory frame.

This method of simulating data has the advantage that the details of the kinematics at input do not need to be known, that is to say a formalism to describe the exchange mechanism is not needed. Furthermore, it is relatively fast, allowing a few hundred million events to be to be generated in a few hundred hours of computer time.

A set of acceptance tables is calculated using the measured positions of the detectors by tracing tracks generated in bins of momentum, p, polar angles θ and ϕ, and vertex x-position, v_x, through the detector planes. In the case of the slow proton, the energy losses experienced in the target and box counter are taken into account. A plot of the momentum loss, dp, predicted for the slow proton against its final momentum is shown in figure 6.2, where it is seen that the energy loss primarily affects the low p region. The "band" structure in this plot is due to the effect of binning the data

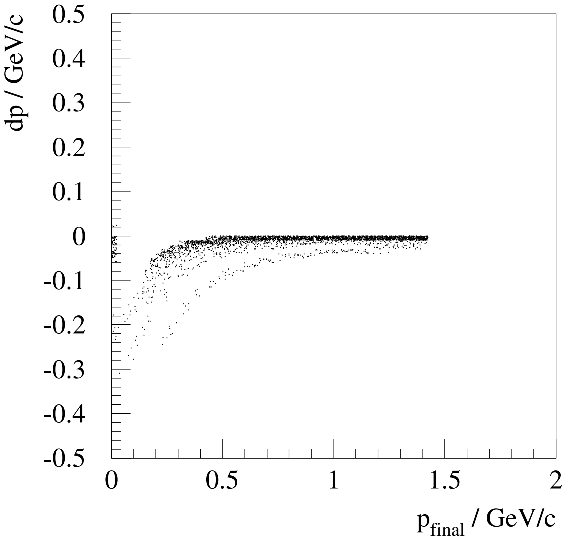

Figure 6.2: Predicted momentum loss experienced in target against final momentum.

in $\cos\theta$. Each simulated event is required to satisfy the same trigger conditions as the real data, *i.e.*, the fast track must trace through A1 and A2, and a slow proton must trace through TB(1), CL(5), CL(7) and SPC(L). In order to be reconstructed, each pion must trace through at least 4 B chambers.

In liquid hydrogen, for momenta less than a few hundred GeV, pions lose about 4 MeV/g cm^{-2} above $\beta\gamma \sim 3$ [4]. For ~50 cm of hydrogen target material the energy loss is a few hundred MeV for all p being considered. This small correction can be taken into account in the Monte Carlo, but is found to have little effect on the final results.

Using the acceptance tables, the generated tracks are traced through the detector planes. It has been found necessary to include two efficiency corrections which are functions of momentum. The first of these corrects for the efficiency of the SPC(L) slabs. To see how this comes about, consider the slow proton momentum spectrum for each slab, normalized to slab 7 (this slab is used because it has the largest pulse height for a given momentum of all the slabs in SPC(L)). A sample of these plots, smoothed by the 353QH algorithm [70], are shown in figure 6.3. It may be

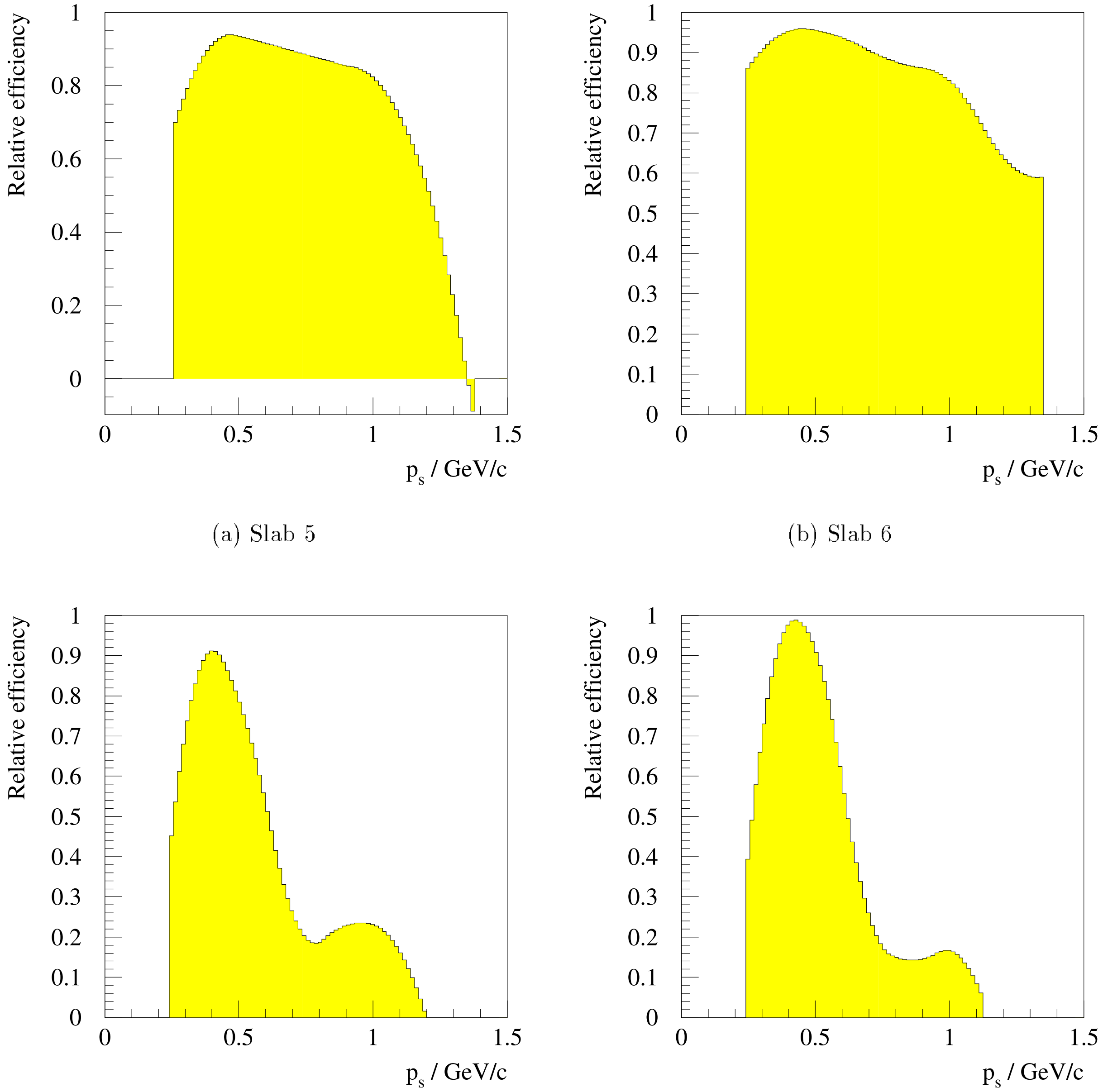

(a) Slab 5

(b) Slab 6

(c) Slab 9

(d) Slab 10

Figure 6.3: Slow proton momentum normalized to slab 7.

seen that while some of the slabs exhibit a fairly flat efficiency as a function of momentum (figures 6.3 a and b), others show a drop in efficiency at a momentum of approximately 0.5 GeV/c (figures 6.3 c and d). This efficiency is due to the discriminator cut placed at trigger level on each slab pulse height. Efficiency curves such as the ones shown in figure 6.3 are made for all the slabs in SPC(L) and are used as corrections in the Monte Carlo procedure described above.

The second correction as a function of momentum applies to the central tracks. Here it is found that the efficiency of TRIDENT for reconstructing a vertex is correlated with the momentum of the pions, particularly at low momentum, where the reconstruction efficiency is poor.

In addition to these corrections, the same cuts are applied to the Monte Carlo data as are applied to the real data, namely the diffractive mass cuts on the pπ systems.

A comparison between the kinematic distributions produced by the simulation and those observed in the data is given in chapter 7, where it is shown that good agreement is produced between the predicted behaviour of the 4-momentum transfer at both the fast and slow vertices and that observed in the data.

For the simulated data, values of θ and ϕ are calculated in 100 MeV bins of $\pi^+\pi^-$ mass, both before and after the acceptance corrections are applied. The output of these divided by the input produces a set of corrections which describe the inverse of the acceptance weight in each mass bin. These are shown in figures 6.4 and 6.5, where it may be seen that the corrections are smoothly varying functions of $\cos\theta$, ϕ and $\pi^+\pi^-$ mass. The majority of the structure observed is due to the diffractive cuts.

The acceptance weight for each event is then found by taking the reciprocal of the acceptance for those values of m, $\cos\theta$ and ϕ.

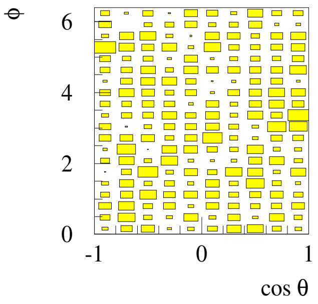

(a) 0.2 GeV/c^2 – 0.3 GeV/c^2

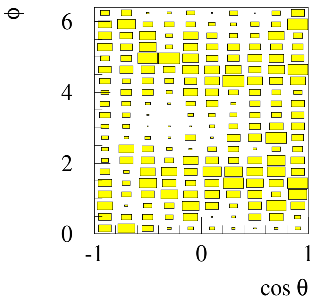

(b) 0.3 GeV/c^2 – 0.4 GeV/c^2

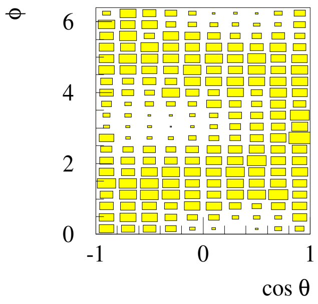

(c) 0.4 GeV/c^2 – 0.5 GeV/c^2

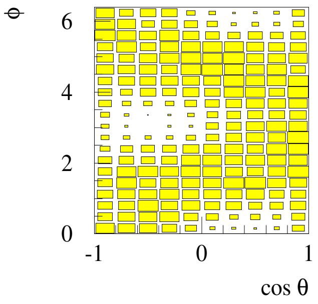

(d) 0.5 GeV/c^2 – 0.6 GeV/c^2

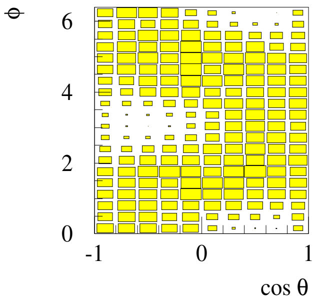

(e) 0.6 GeV/c^2 – 0.7 GeV/c^2

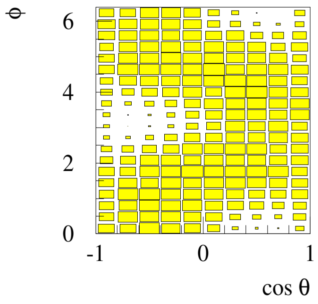

(f) 0.7 GeV/c^2 – 0.8 GeV/c^2

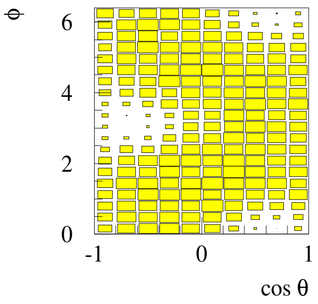

(g) 0.8 GeV/c^2 – 0.9 GeV/c^2

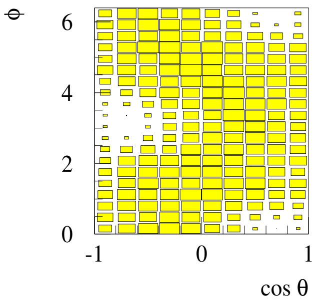

(h) 0.9 GeV/c^2 – 1.0 GeV/c^2

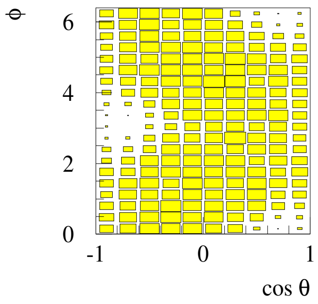

(i) 1.0 GeV/c^2 – 1.1 GeV/c^2

Figure 6.4: Corrections for $\cos\theta$ and ϕ as a function of $\pi^+\pi^-$ mass.

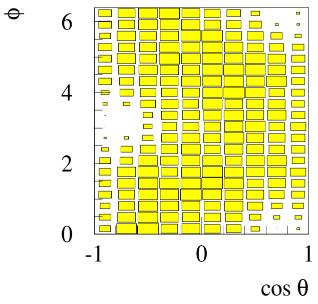

(a) 1.1 GeV/c^2 – 1.2 GeV/c^2

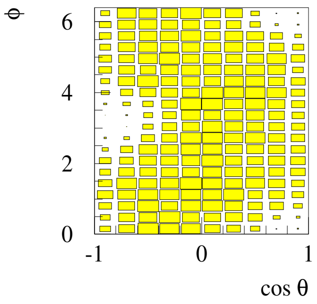

(b) 1.2 GeV/c^2 – 1.3 GeV/c^2

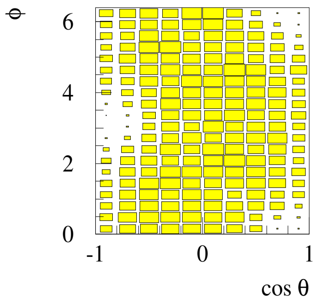

(c) 1.3 GeV/c^2 – 1.4 GeV/c^2

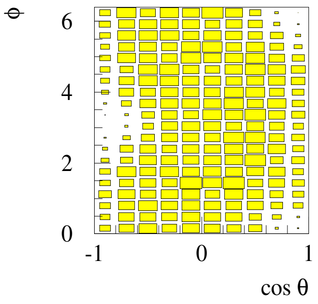

(d) 1.4 GeV/c^2 – 1.5 GeV/c^2

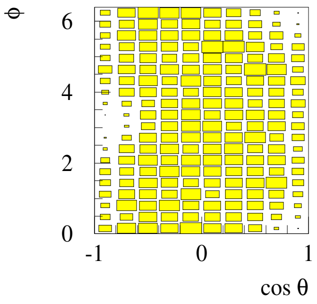

(e) 1.5 GeV/c^2 – 1.6 GeV/c^2

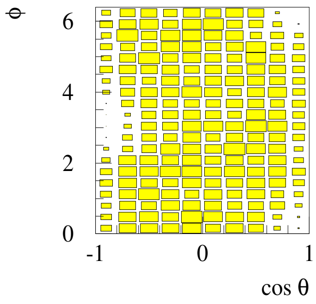

(f) 1.6 GeV/c^2 – 1.7 GeV/c^2

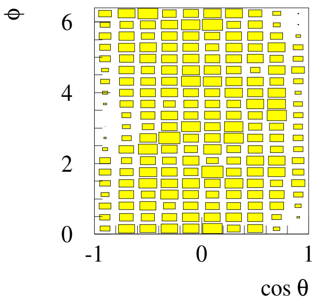

(g) 1.7 GeV/c^2 – 1.8 GeV/c^2

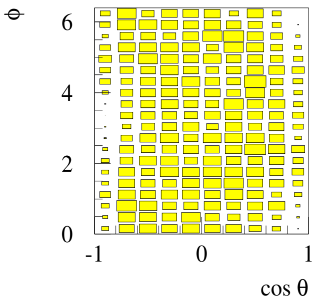

(h) 1.8 GeV/c^2 – 1.9 GeV/c^2

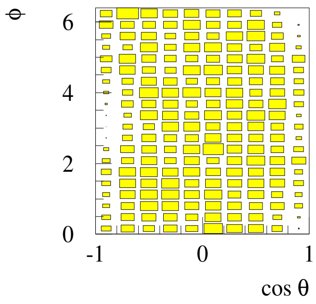

(i) 1.9 GeV/c^2 – 2.0 GeV/c^2

Figure 6.5: Corrections for $\cos\theta$ and ϕ as a function of $\pi^+\pi^-$ mass.

6.2 Moments

The moments are calculated according to the prescription discussed in chapter 5, that is

$$H(L,M) = \sum_{i=1}^{N} \mathcal{D}^{(L)}_{M0}(\Omega_i) acc_i^{-1}$$

are found for each L, M. For the 1992 data, the moments are shown in figures 6.6 and 6.7. Other moments are generally consistent with being zero for all m; in particular, very little activity is seen in moments with $L > 4$.

In order to understand the error calculation on each bin, consider a histogram bin with x entries, filled such that

$$x = \sum_{i=1}^{N} w_i,$$

i.e., the ith entry is weighted by w_i. Then $x = N\langle w\rangle$, where $\langle w\rangle$ is the mean value of the weight for that bin. Assuming that N and w are independent, then

$$\left(\frac{\sigma_x}{x}\right)^2 = \left(\frac{\sigma_N}{N}\right)^2 + \left(\frac{\sigma_{\langle w\rangle}}{\langle w\rangle}\right)^2.$$

Now for Poisson statistics, $\sigma_N = \sqrt{N}$. Furthermore, the error on $\langle w\rangle$, $\sigma_{\langle w\rangle}$ is simply $\frac{\sigma_w}{\sqrt{N}}$, where $\sigma_w^2 = \sum_{i=1}^{N} \sigma_{w_i}^2$, and hence

$$\left(\frac{\sigma_x}{x}\right)^2 = \frac{1}{N} + \frac{\sigma_w^2}{N\langle w\rangle^2}.$$

Then

$$\sigma_x{}^2 = N\langle w\rangle^2 + N\sigma_w^2 = N\langle w\rangle^2 + N\langle w^2\rangle - N\langle w\rangle^2,$$

and thus,

$$\sigma_x{}^2 = N\langle w^2\rangle = \sum_{i=1}^{N} w_i^2. \tag{6.1}$$

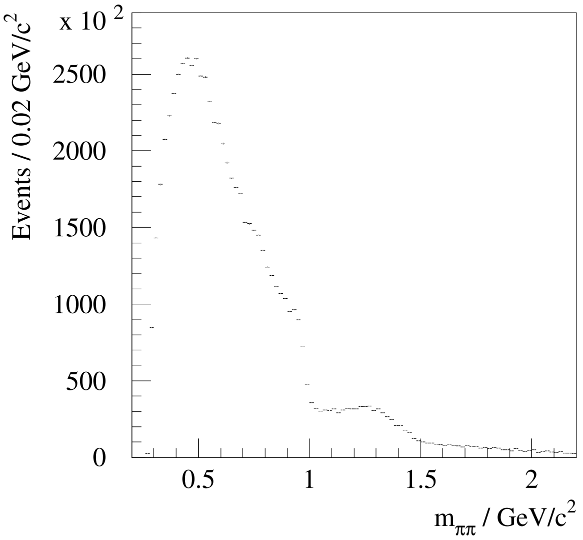

(a) H(0,0)

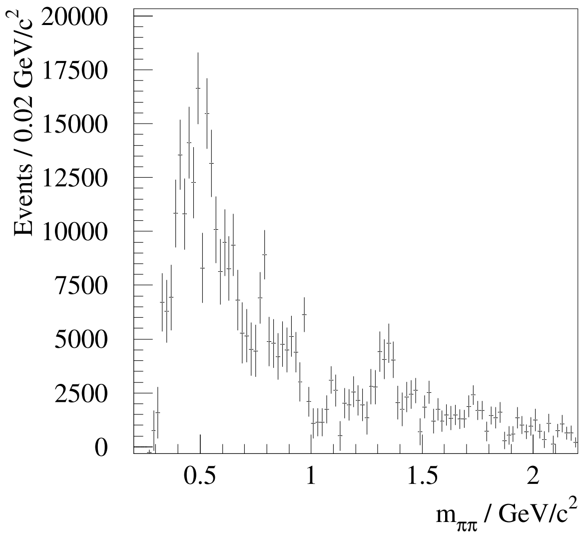

(b) H(1,0)

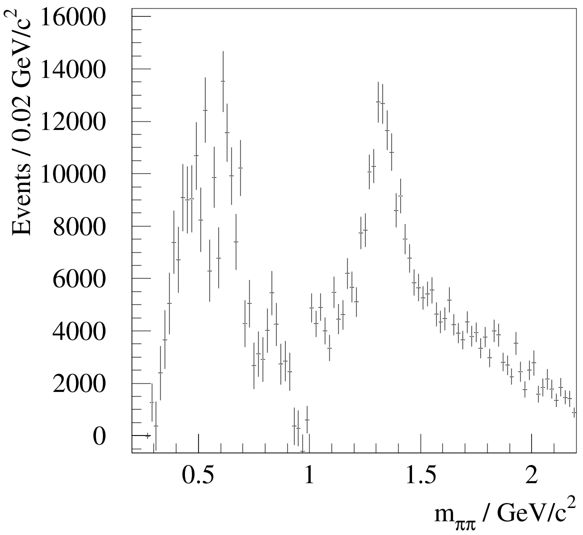

(c) H(2,0)

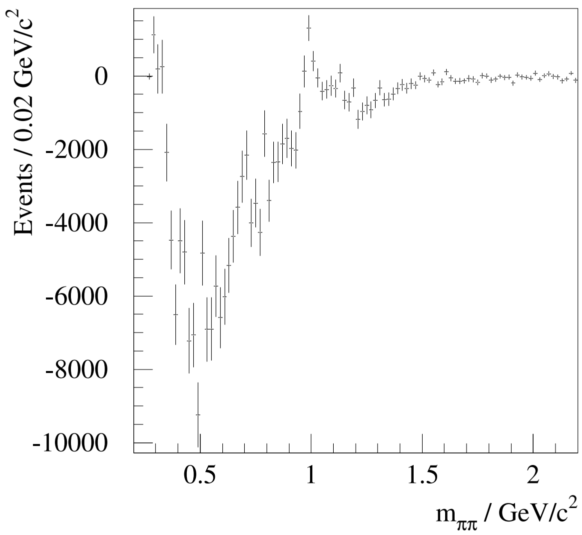

(d) H(2,2)

Figure 6.6: Acceptance corrected moments.

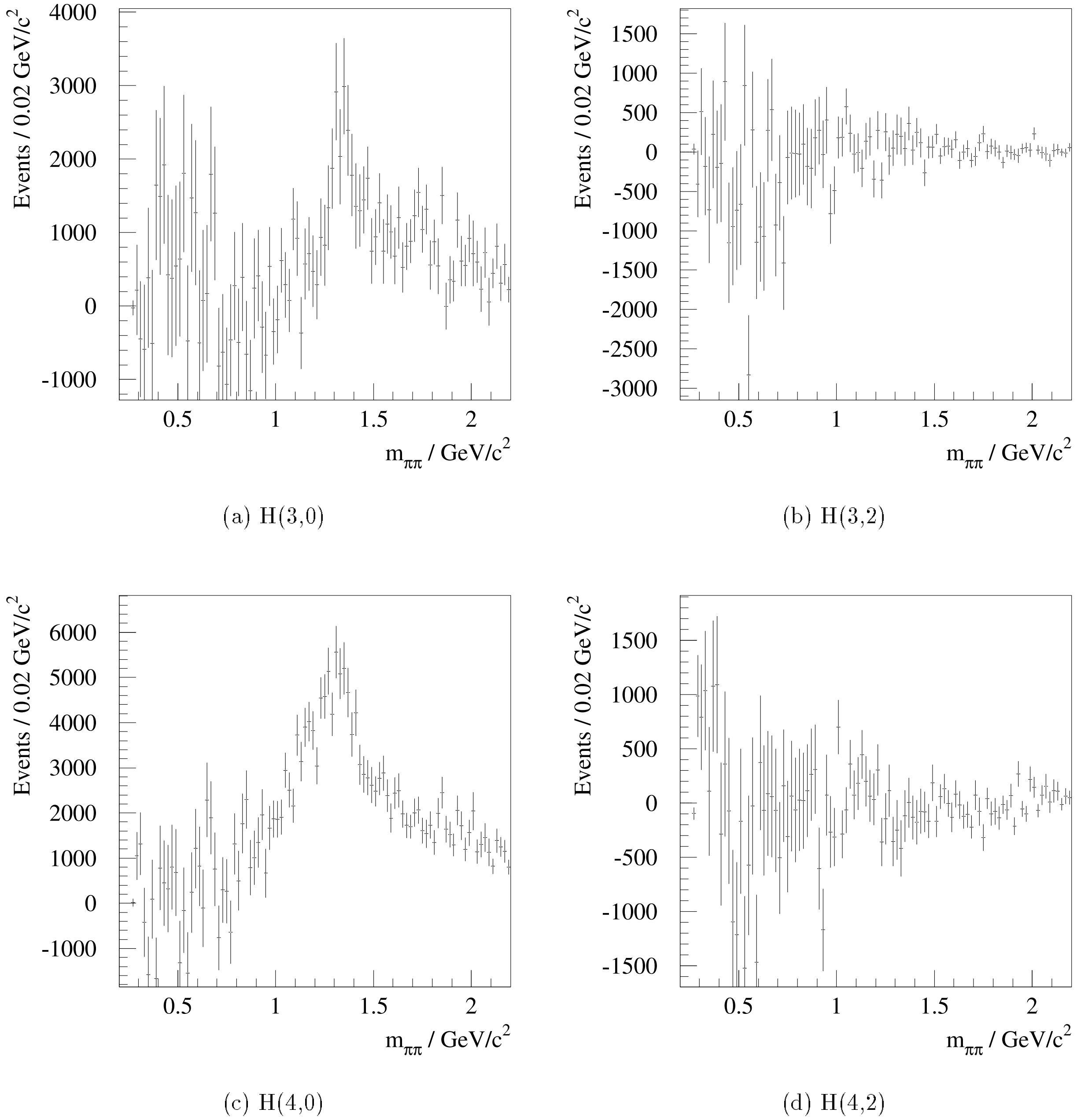

Figure 6.7: Acceptance corrected moments.

The effect of the $\omega(783)$ reflection from the channel $\mathrm{pp} \longrightarrow \pi^+\pi^-\pi^0$ discussed in chapter 4 is taken into account by generating $\omega(783)$ events, calculating the angles θ and ϕ in the PWA axes for decays of the simulated particles, and then generating a set of moments for these θ and ϕ. The fit discussed in chapter 4 gives the amount of $\omega(783)$ reflection needed to fit the $\pi^+\pi^-$ mass spectrum as being $(7.5 \pm 0.7) \times 10^{-6}$. Taking into account the number of events generated by the $\omega(783)$ simulation, this corresponds to $3.0 \pm 0.4\%$ of the total number of events in the $\pi^+\pi^-$ mass spectrum. This value is used to normalise the $\omega(783)$ moments, which are shown in figures 6.8 and 6.9. These are then subtracted from the $\pi^+\pi^-$ moments, resulting in the $\pi^+\pi^-$ moments shown in figures 6.10 and 6.11.

The imaginary parts of all moments are found to be consistent with zero in all mass bins. Furthermore, if a set of data are generated using this simulation technique (*i.e.*, flat in $\cos\theta$ and ϕ for all masses), then applying the acceptance tables to these data and correcting them using the acceptance weights, produces moments which are again found to be consistent with zero in all mass bins.

6.3 Fitting procedure and ambiguities

The moments are fitted to the parameterization developed in chapter 5 independently for each mass bin. The fitting is performed by minimising χ^2 in each mass bin using MINUIT [56]. All the parameters are constrained to be positive, with the phase angles further restricted to less than 2π. This results in the fits shown in figures 6.12 and 6.13. The fit parameters as a function of mass are shown in figures 6.14 and 6.15, together with the minimized χ^2 value for each mass bin.

It may be seen that the quality of the fit is reasonable in most mass bins. An examination of the fit parameters shows that the S-wave clearly dominates at low mass, although there is some P-wave below 1 GeV/c^2. The D-wave activity is consistent with being close to zero at low mass, and the resonant D-wave at the

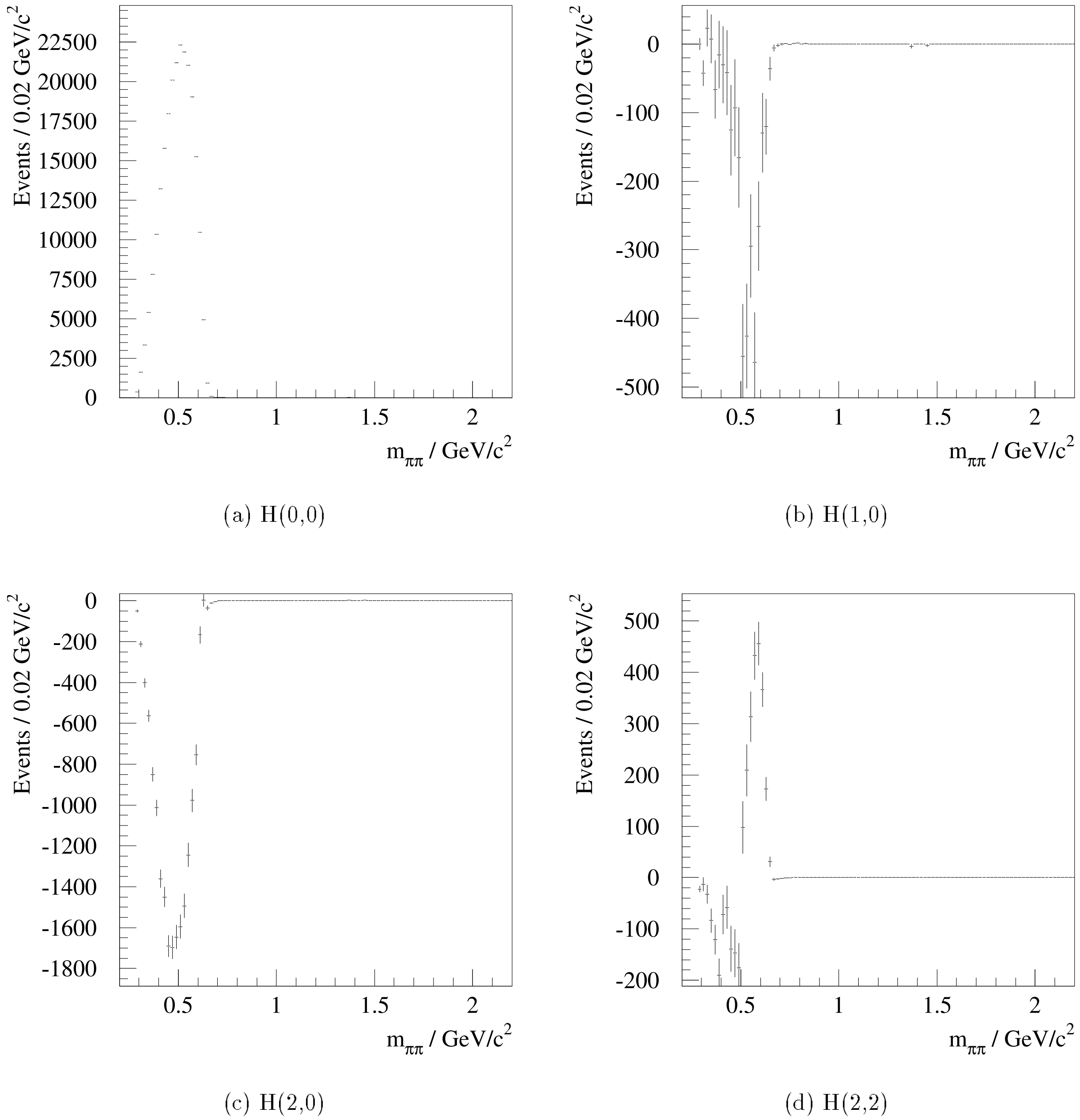

Figure 6.8: Acceptance corrected moments for $\omega(783)$ reflection from $\pi^+\pi^-\pi^0$.

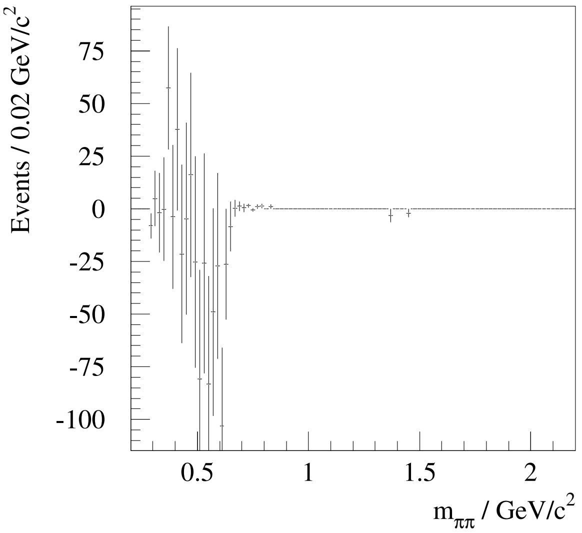

(a) H(3,0)

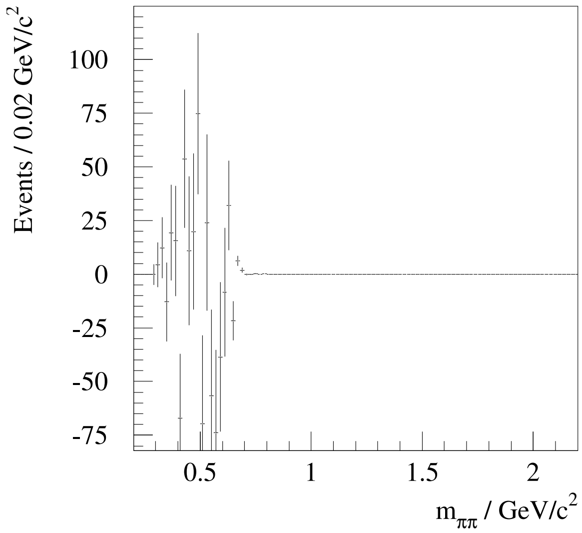

(b) H(3,2)

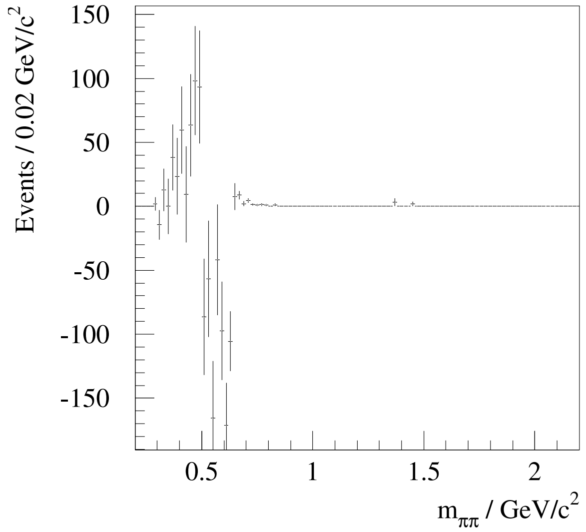

(c) H(4,0)

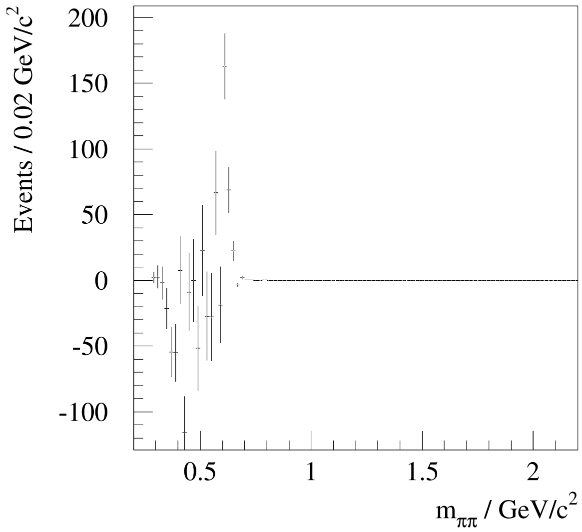

(d) H(4,2)

Figure 6.9: Acceptance corrected moments for $\omega(783)$ reflection from $\pi^+\pi^-\pi^0$.

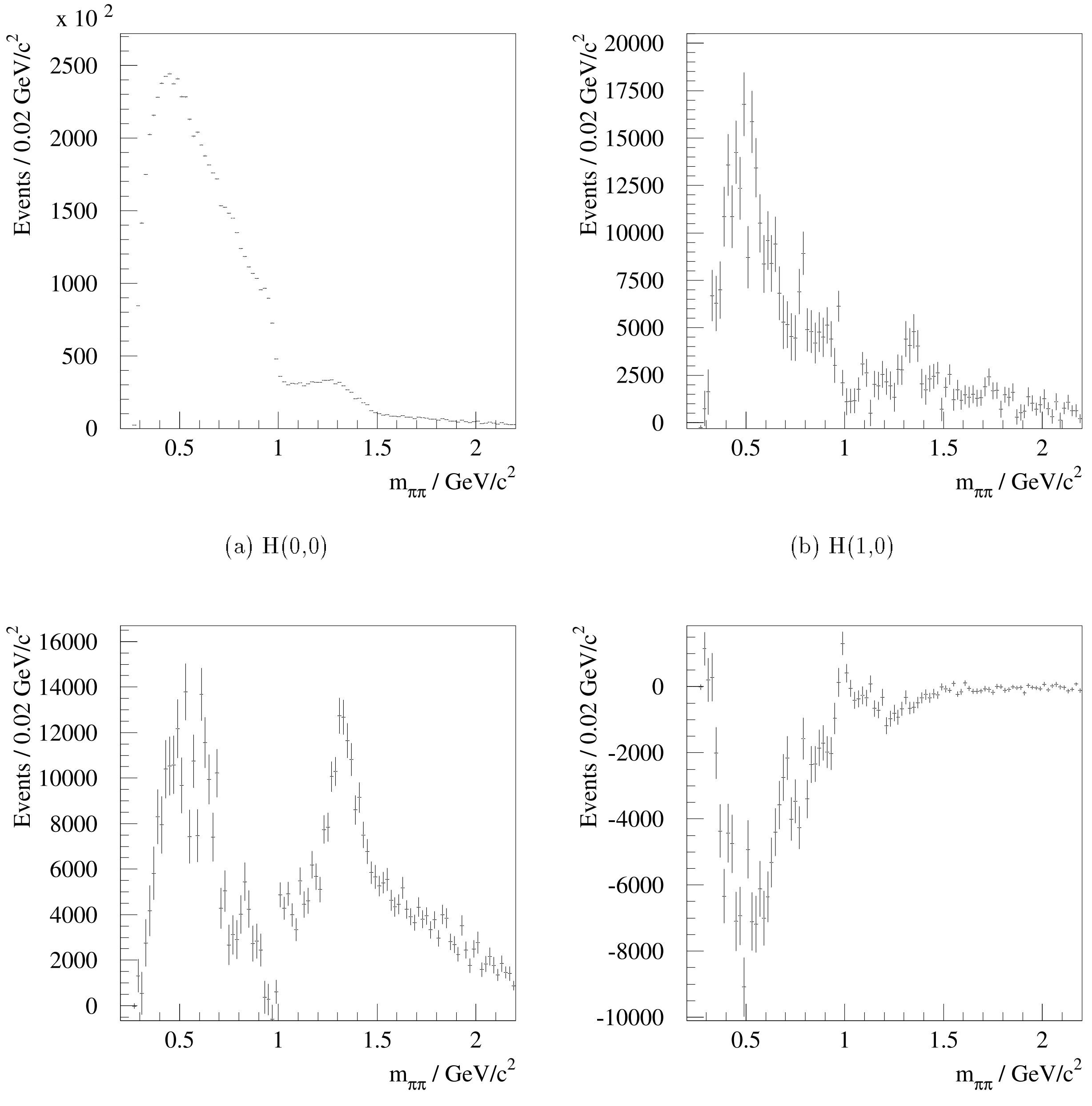

(a) H(0,0)

(b) H(1,0)

(c) H(2,0)

(d) H(2,2)

Figure 6.10: Acceptance corrected moments with $\omega(783)$ contribution removed.

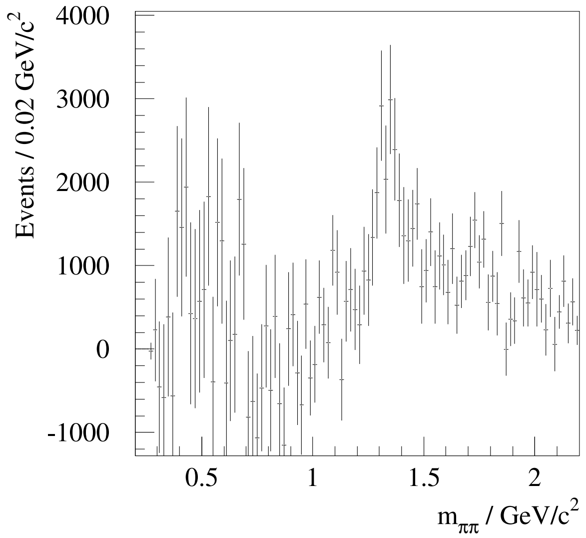

(a) H(3,0)

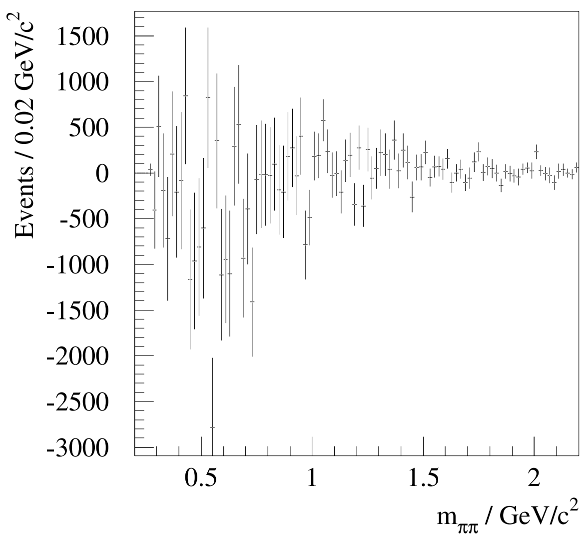

(b) H(3,2)

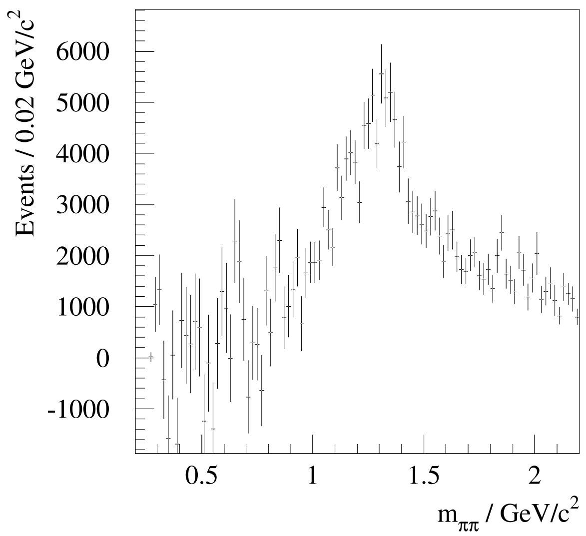

(c) H(4,0)

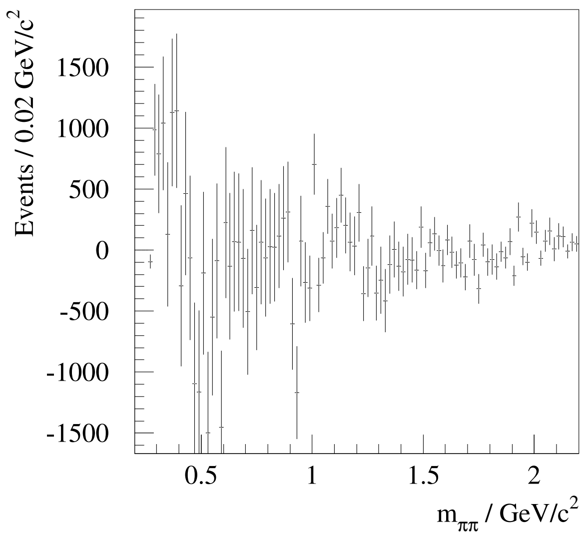

(d) H(4,2)

Figure 6.11: Acceptance corrected moments with $\omega(783)$ contribution removed.

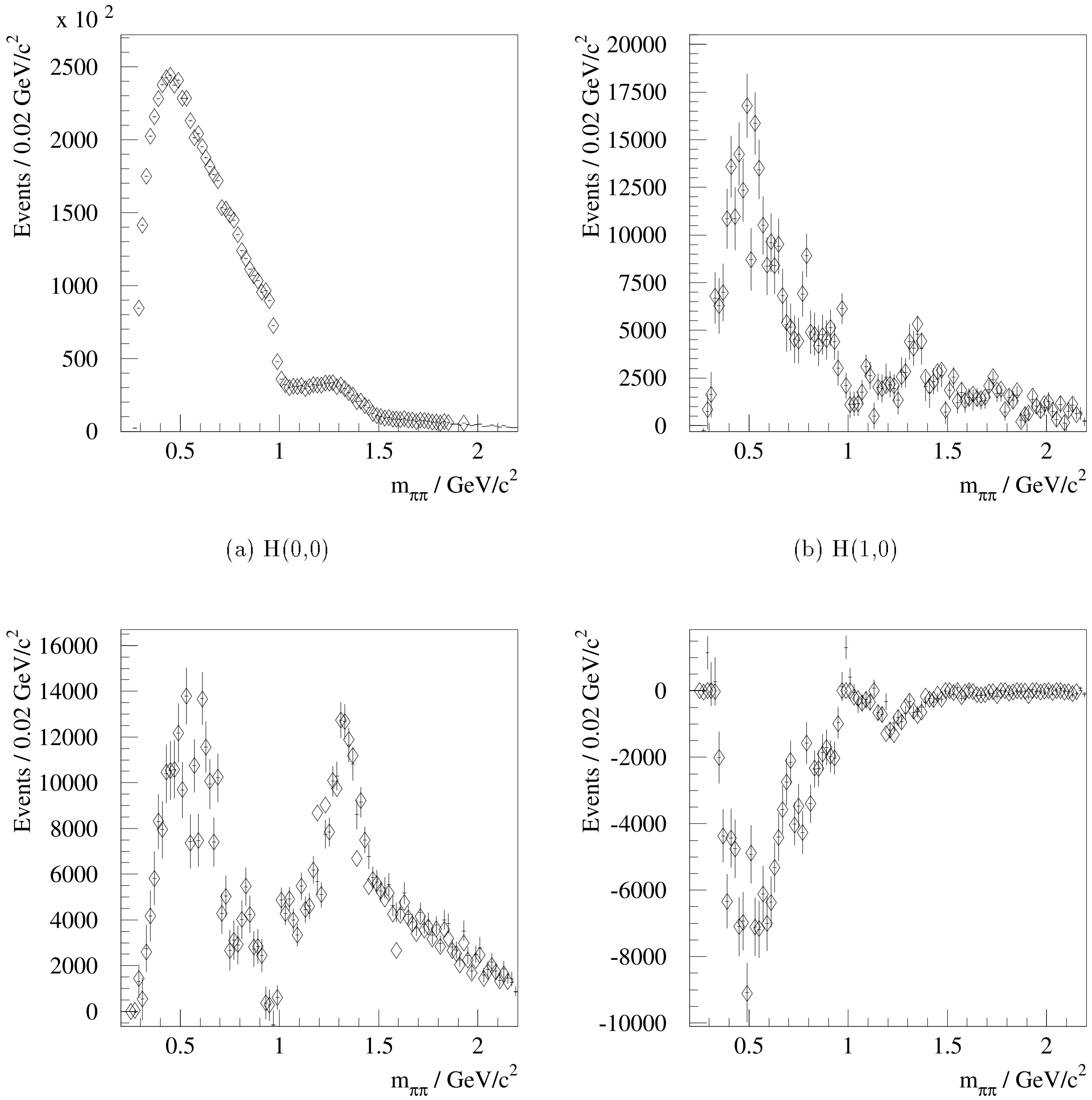

(a) H(0,0)

(b) H(1,0)

(c) H(2,0)

(d) H(2,2)

Figure 6.12: Fit to the acceptance corrected moments, using the parameterization described in chapter 5.

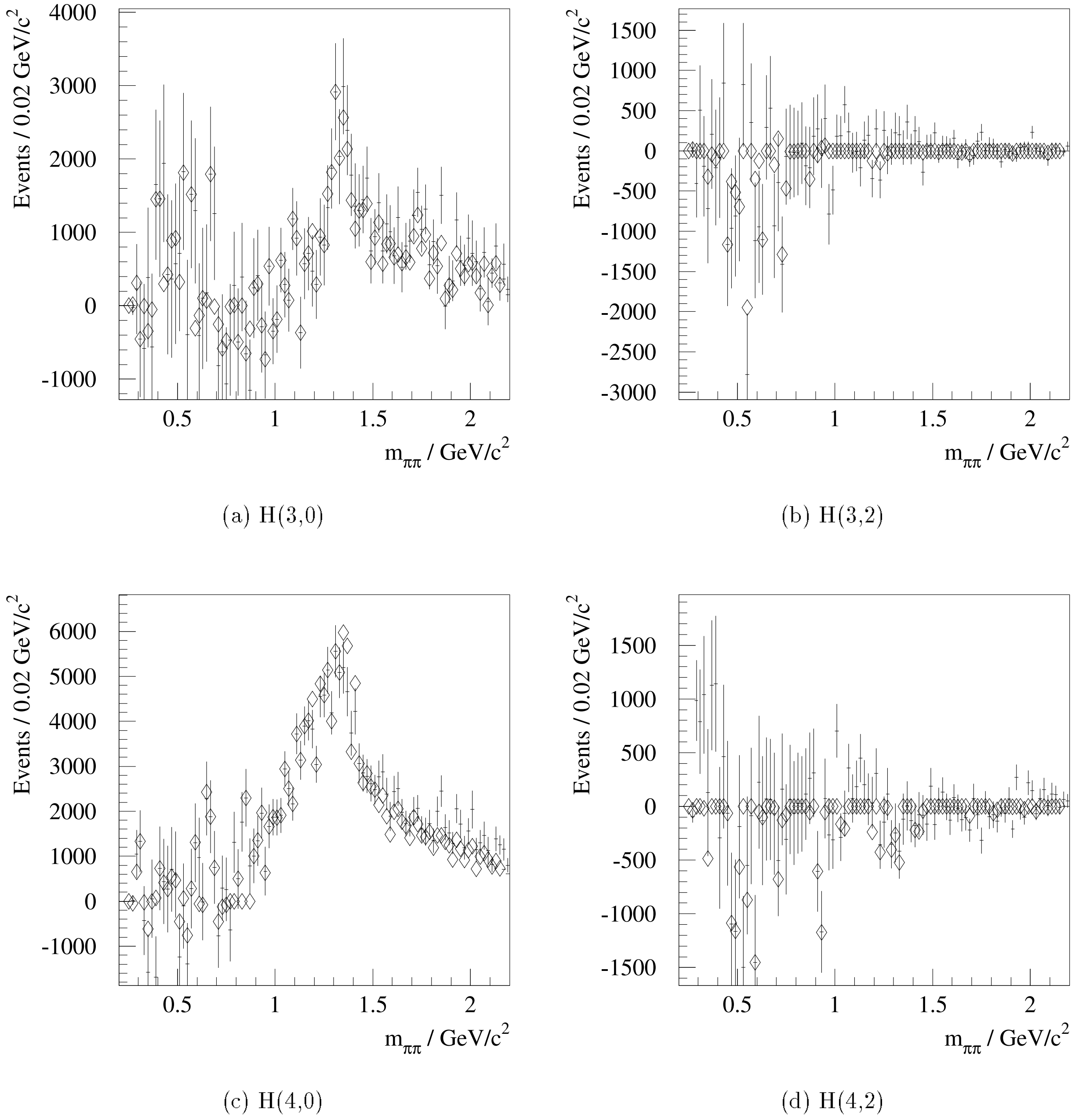

(a) H(3,0)

(b) H(3,2)

(c) H(4,0)

(d) H(4,2)

Figure 6.13: Fit to the acceptance corrected moments, using the parameterization described in chapter 5.

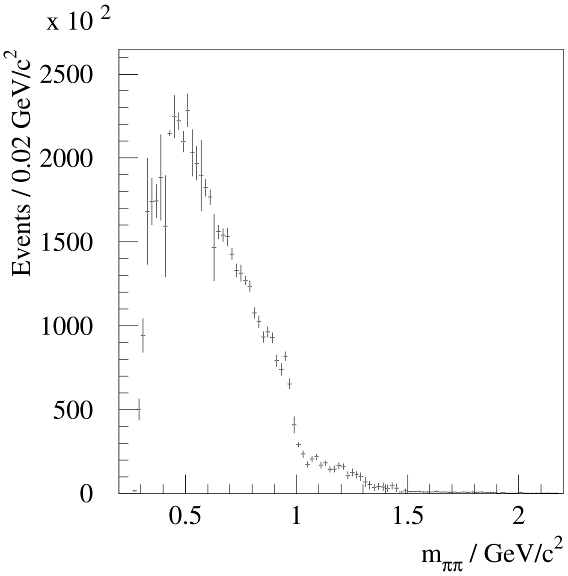

(a) S_0

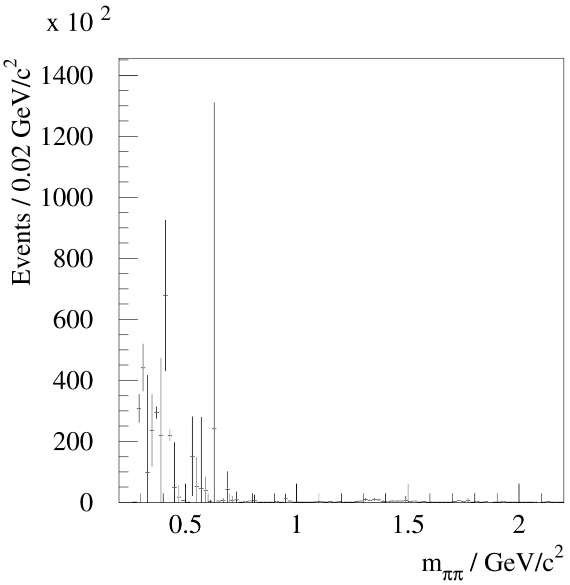

(b) P_0

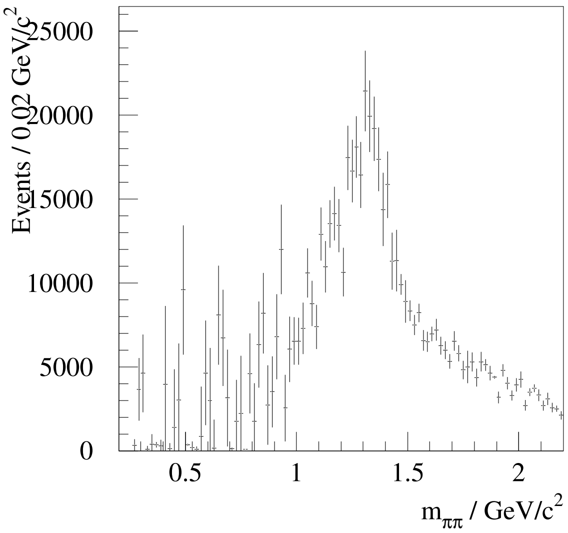

(c) D_0

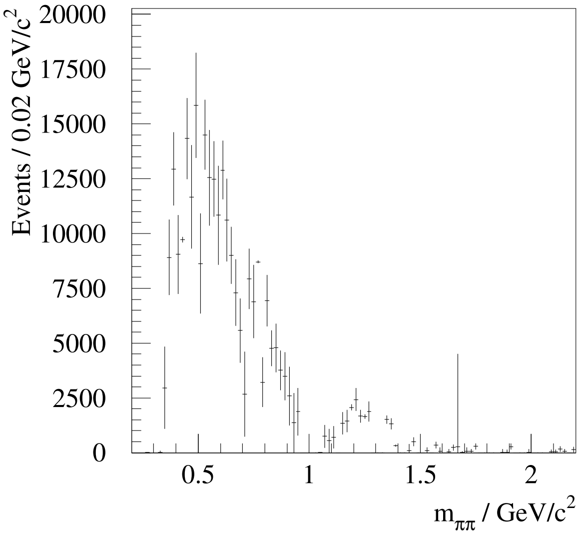

(d) P_1

Figure 6.14: Fit parameters as a function of mass.

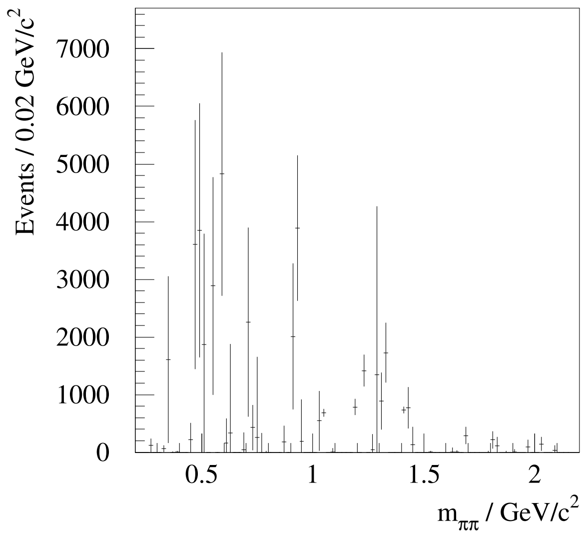

(a) D_1

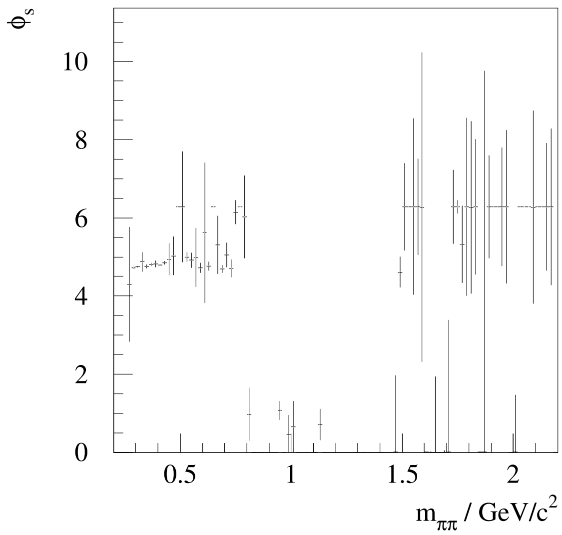

(b) ϕ_S

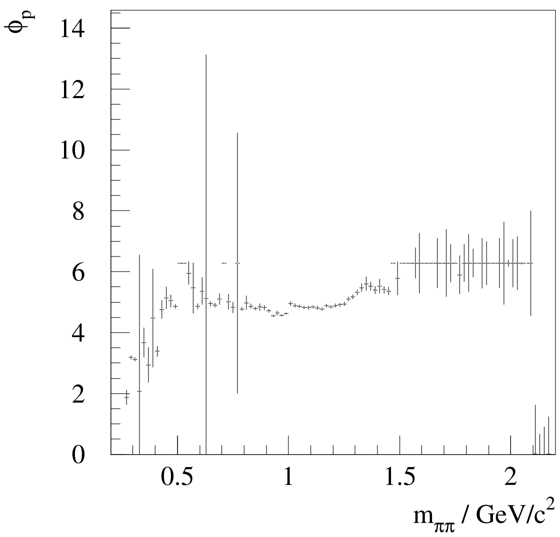

(c) ϕ_P

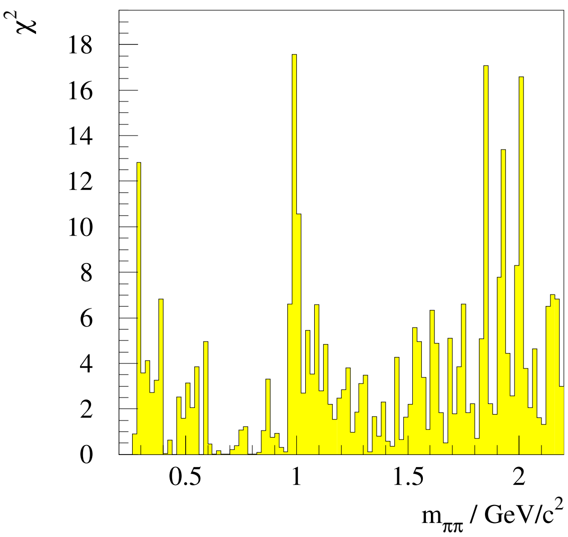

(d) χ^2

Figure 6.15: Fit parameters as a function of mass.

mass of the $f_2(1270)$ is clearly visible in figure 6.14(c). The helicity one terms in this parameterization are both relatively small.

In order to test the stability of the fit to the choice of reference phase, the analysis has been repeated using different reference phases (for example, using the S-wave as the reference phase and ϕ_P and ϕ_D as the free parameters). All cases resulted in similar fit qualities and similar values of the fitted parameters. It should be noted that a good fit cannot be obtained if the parameterization is changed so that the helicity 1 terms are fixed to zero.

6.4 Parameterization of the S-Wave

The interfering $f_0(980)$ parameterization used in the mass spectrum fitting described in chapter 4 has been applied in a fit to the S wave mass spectrum. The interference between the $f_0(980)$ and the background is taken into account by writing

$$\frac{dN}{dm} = G(m)|1 + A_{f_0(980)} F_\pi(m) e^{i\delta_1}|^2,$$

where the definitions are the same as those used in section 4.3. No other resonant states are included. The χ^2 per degree of freedom for this fit is 2.1, which is rather poor. As found for the fit to the mass spectrum, the S-wave cannot be fitted in this formalism in the 1.5 GeV/c^2 region. Instead, an interfering Breit-Wigner term is introduced in the same way as detailed in chapter 4, with mass and width fixed to the values found for the fit to the mass spectrum. This leads to a fit with χ^2 per degree of freedom of 1.28. A comparison of the fits with and without the interference term in the 1.5 GeV/c^2 region is shown in figures 6.16 a) and b). The full fit with the extra interference term is shown in figure 6.17. Using this parameterization, the

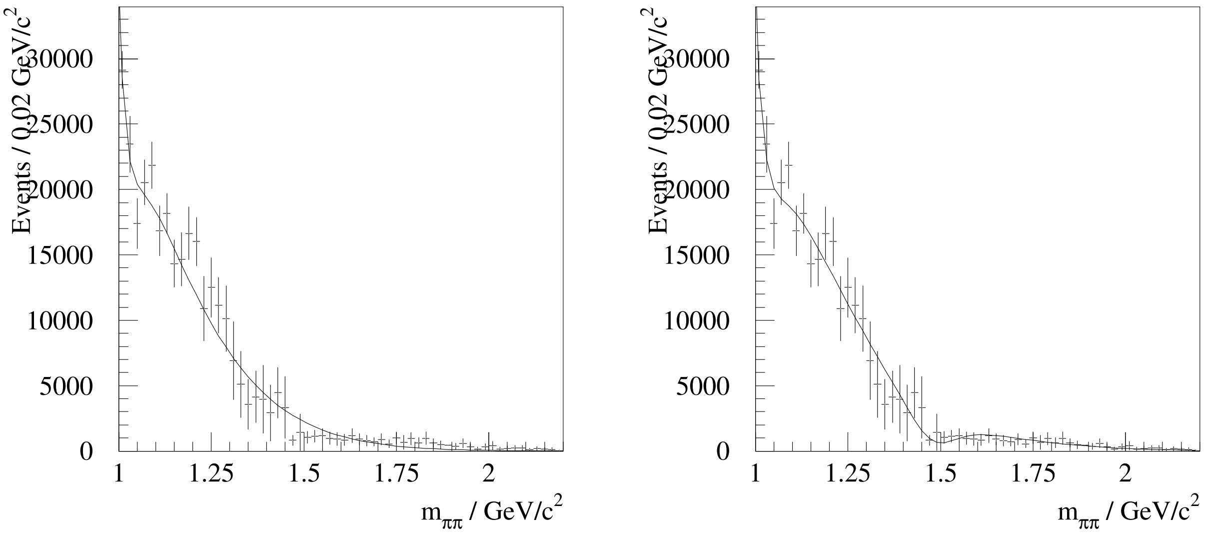

(a) Without term at 1.5 GeV/c^2

(b) With term at 1.5 GeV/c^2

Figure 6.16: Expanded view of the fit in the 1.5 GeV/c^2 region.

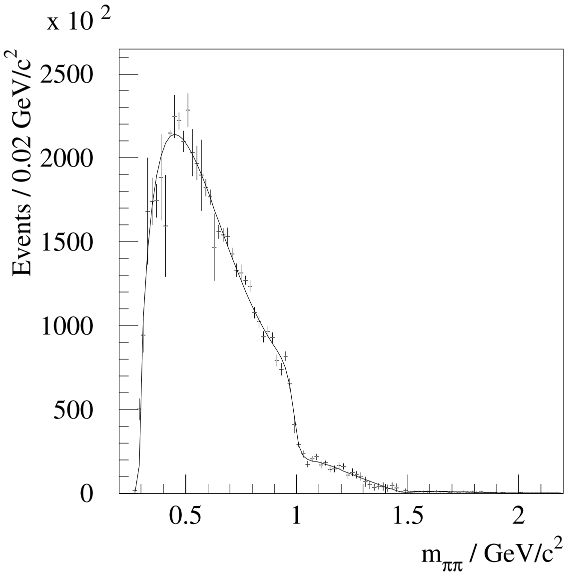

Figure 6.17: The full fit to the S-wave mass spectrum.

$f_0(980)$ parameters are

$$\begin{aligned} m_{f_0(980)} &= (0.98 \pm 0.01) \text{ GeV}/c^2 \\ g_\pi &= (0.23 \pm 0.04) \text{ GeV}/c^2 \\ g_K &= (0.1 \pm 0.1) \text{ GeV}/c^2 \\ \delta_1 &= (97 \pm 5)^\circ, \end{aligned}$$

in reasonable agreement with the mass and couplings obtained from the fit to the total mass spectrum.

A fit where the mass and width of the 1500 MeV/c^2 state are left free gives a χ^2 per degree of freedom of 1.15, with $m = 1.45 \pm 0.05$ GeV/c^2 and $\Gamma = 0.35 \pm 0.10$ GeV/c^2. There is no evidence of another scalar state around 1700 MeV/c^2 in addition to the state at 1500 MeV/c^2.

6.4.1 Other Parameterizations of the S-Wave

The WA91 S-wave mass spectrum presented above appears to be quite similar to that obtained by the AFS Collaboration, who also studied the centrally produced $\pi^+\pi^-$ system, but at a higher centre-of-mass energy of $\sqrt{s} = 63$ GeV [71]. At this energy, the exchange mechanism is dominantly DPE, and hence AFS only fitted the helicity 0 terms in S and D-waves. The AFS S-wave mass spectrum is shown in figure 6.18. The fit is from Au, Morgan and Pennington (AMP) [57]. This is a fit to the poles of the K matrix. A description of the K matrix formalism is given in [72], and only a brief discussion of the formalism is given here.

The K matrix expresses the unitarity of the S matrix for processes important in meson spectroscopy. The elements of $\mathbf{S}$ are the scattering operators for the amplitude that an initial state $|i\rangle$ will be scattered into a final state $|f\rangle$, *i.e.*,

$$S_{fi} = \langle f|S|i\rangle.$$

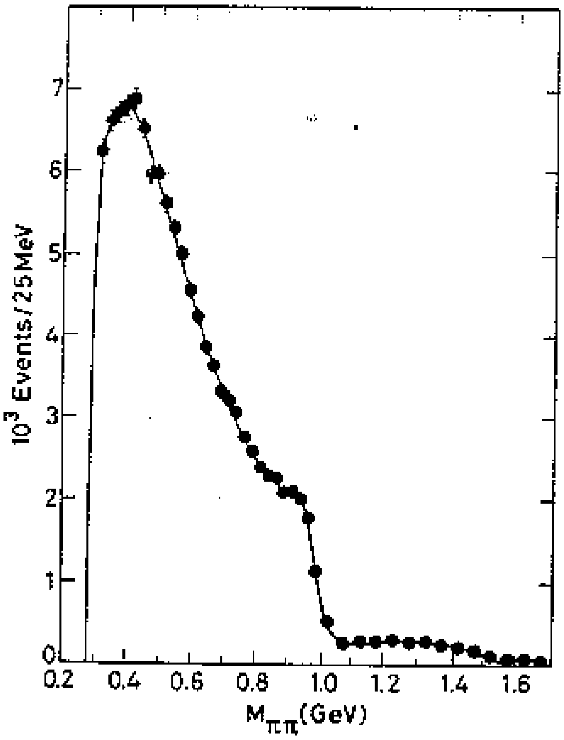

Figure 6.18: The S-wave $\pi^+\pi^-$ mass spectrum obtained by the AFS Collaboration [57].

To ensure that the initial and final states experience some interaction, the transition operator, T, is defined by

$$S = I + 2iT,$$

where I is the identity operator. Unitarity implies that

$$SS^\dagger = S^\dagger S = I$$

and then

$$T - T^\dagger = 2iT^\dagger T = 2iTT^\dagger.$$

This may be transformed to

$$(T^{-1} + iI)^\dagger = T^{-1} + iI$$

and then the K operator may be introduced as

$$K^{-1} = T^{-1} + iI.$$

From this, it may be shown [72] that

$$T = K(I - iK)^{-1} = (I - iK)^{-1}K.$$

In 2-channel problems, S, T and K become 2×2 matrices, $\mathbf{S}$, $\mathbf{T}$, $\mathbf{K}$.

The Au, Morgan and Pennington parameterization of $\mathbf{K}$ is of the form

$$K_{ij} = \frac{s - s_0}{4m_{\mathrm{K}}^2} \sum_p \frac{f_i^p f_j^p}{(s_p - s)(s_p - s_0)} + \sum_{n=0} c_{ij}^n \left(\frac{s}{4m_{\mathrm{K}}^2} - 1\right)^n,$$

where the $f_{i,j}^p$ are the couplings to each channel, and the c_{ij}^n are terms of a polynomial to represent a background. $\mathbf{T}$ is then given by $T = K(1 - i\rho K)^{-1}/(s - s_0)$, which is slightly modified from the form shown above by the factor ρ, which represents the breakup momenta to each channel. The cross section for DPE is

$$\sigma_{PP}^J(m) \sim 1/M^2(\alpha_1^{PP} T_{11} + \alpha_2^{PP} T_{21}),$$

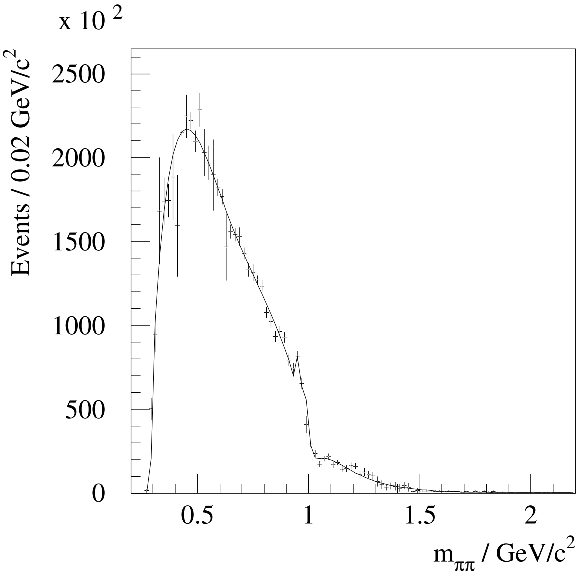

Figure 6.19: A comparison of a typical set of parameters used in the formalism due to Au, Morgan and Pennington with the data.

where the α_i's are expressed as

$$\alpha_i = \sum_{n=0} \alpha_i^n \left(\frac{s}{4m_{\mathrm{K}}^2} \right).$$

According to Au, Morgan and Pennington, these are the intrinsic couplings which describe the propensity of the production process to initiate production in channel i. [57] also shows that for central production, T_{11} is related to the observed S-wave cross section by scaling by a factor of $1/m^2$.

It is possible to use this form directly to obtain the overall shape of the WA91 $\pi^+\pi^-$ S wave, and a comparison of a typical set of parameters used in this formalism with the WA91 data is shown in figure 6.19. However, attempts to fit the mass spectrum using this parameterization have not been extensively pursued. This is because the parameterization was developed to simultaneously fit data on central production, $\pi\pi \longrightarrow \pi\pi$ scattering and $\pi\pi \longrightarrow \mathrm{K}\overline{\mathrm{K}}$ scattering. The fit shown in figure 6.18 was obtained using 24 parameters, and although the quality of the fit is certainly impressive, it is not clear how the final fitted parameters depend on the $\pi\pi$ scattering data. In particular, changing the values of the α_i's can change the shape of the fit by a large amount. Au, Morgan and Pennington claim that the elements of $\mathbf{T}$ may be determined in principle from the $\pi\pi$ scattering data, and then the central production data may be used to determine the α_i's (although they do add that the AFS results "...provide significant extra information on $[T_{ij}]$..."). Ideally, then, the WA91 central production data should be fitted simultaneously with $\pi\pi$ scattering data, which would enable us to constrain the fit by unitarity explicitly. This would be an interesting, but difficult, exercise, and instead an alternative parameterization of the K matrix has been used to fit the S-wave mass spectrum.

This parameterization is due to Anisovich *et al.* [73], and is discussed in some detail in [74, 30]. The formalism fits the background and generates a narrow $f_0(980)$ through interference between two broad K-matrix poles,

$$
\begin{aligned}
K_{11} &= \left(\frac{g_\pi^2}{M_1^2 - s} + \frac{G_\pi^2}{M_2^2 - s}\right)\frac{s - m_\pi^2/2}{s}, \\
K_{12} &= \left(\frac{g_\pi g_K}{M_1^2 - s} + \frac{G_\pi G_K}{M_2^2 - s} + f_{\pi K}\frac{1 - s_0}{s - s_0}\right)\frac{s - m_\pi^2/2}{s}, \\
K_{22} &= \left(\frac{g_K^2}{M_1^2 - s} + \frac{G_K^2}{M_2^2 - s}\right)\frac{s - m_\pi^2/2}{s}, \\
T_{11} &= \frac{K_{11} - i\rho_K(K_{22}K_{11} - K_{12}^2)}{1 - i\rho_\pi K_{11} - i\rho_K K_{22} - \rho_\pi\rho_K(K_{11}K_{22} - K_{12}^2)}.
\end{aligned}
$$

The poles of the K-matrix do not correspond directly to resonant states. In particular, it should be noted that the poles are not in themselves supposed to represent the $f_0(980)$, $f_0(1300)$ or $f_0(1500)$. Bugg, Sarantsev and Zou [30] claim that the 1300 MeV/c^2 and 1500 MeV/c^2 states can be generated in this parameterization by adding further K-matrix poles. However, the parameterization then suffers from problems with numerical convergence since the poles must generate a narrow $f_0(980)$, and so it is inappropriate to add extra poles in this way.

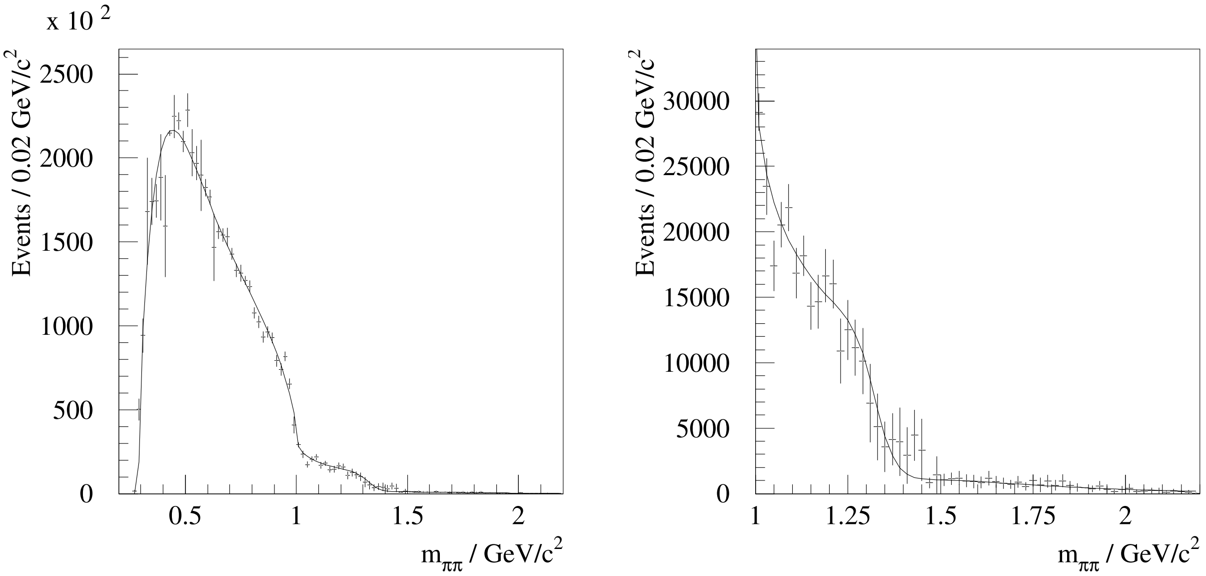

(a) Fit using the T-matrix parameterization

(b) Expanded view

Figure 6.20: Fit to the S-wave mass spectrum using the T-matrix parameterization.

Since this parameterization was not initially developed for multi-channel fits, it does not have the same problems as that discussed above for the AMP form. Using this method, the S-wave mass spectrum is fitted, and the fit shown in figure 6.20 a is obtained. An expanded view of the 1.5 GeV/c^2 region is shown in figure 6.20 b. The χ^2 per degree of freedom for this fit is ~ 1.35, giving a good fit to the data. The fit parameters are given in table 6.1. In this parameterization, the g, G couplings are allowed to be negative. It may be seen from figure 6.20 that the two poles do indeed interfere to apparently produce a narrow $f_0(980)$. However, the poles of the K matrix are merely a convenient way to parameterize a mass spectrum, and do not correspond directly to physical states. Instead, it is important to find the poles of the S matrix. Since the S matrix is related simply to the T matrix in this formalism, it is necessary to find the poles of $\mathbf{T}$. These are given by

$$1 - i\rho_\pi K_{11} - i\rho_K K_{22} - \rho_\pi \rho_K (K_{11}K_{22} - K_{12}^2) = 0.$$

Table 6.1: The parameters for the fitted $\pi^+\pi^-$ mass spectrum.

Fit Parameter	Value
M_1	(0.74± 0.01) GeV/c^2
M_2	(1.31± 0.02) GeV/c^2
g_π	(0.68± 0.01) GeV/c^2
g_K	(-0.5± 0.03) GeV/c^2
G_π	0.01± 0.01 GeV/c^2
G_K	(-0.69± 0.01) GeV/c^2
$f_{\pi K}$	0.71 ± 0.01
s_0	(-0.8±0.1) GeV^2/c^4

It is found that the sheet II pole is at $((1009 \pm 2) - i(280 \pm 2))$ MeV/c^2 and the sheet III pole at $((894 \pm 2) - i(1135 \pm 2))$ MeV/c^2, both of which are very far from the physical region (corresponding to two very broad poles for the $f_0(980)$). These are certainly not consistent with the sheet II and III poles calculated for the fit to the total mass spectrum, nor are they consistent with the results found by Bugg *et al.* of $(1005 - i36)$ MeV/c^2 on sheet II and $(983 - i112)$ MeV/c^2 on sheet III [30]. This indicates that although the parameterization has led to a good fit, the fitted parameters do not correspond to the relevant physical quantities, and suggests that a fit using only an $f_0(980)$ and interfering background in this formalism is inappropriate. Two points should be noted :

- The *caveat* concerning adding further poles directly to the K-matrix, *i.e.* this leads to poor numerical convergence.
- A problem arises similar to that mentioned in the discussion of the AMP formalism. Although the parameterization of the S-wave background is appropriate for use in fits to single channels, Bugg *et al.* add poles to the T-matrix corresponding to the $f_0(1300)$ and $f_0(1500)$ in multi-channel fits to several S-wave spectra from a variety of experiments, together with other poles to

describe resonant terms in other waves. The new poles interfere with each other and the original background and $f_0(980)$. Although these can be added in the present analysis, fitting this modified T-matrix has not been attempted extensively, since in the case of multi-channel fits data from one reaction can presumably be used to constrain the amount of interference that a particular pole gives in another data set. In the present case of a single-channel fit, however, these constraints are not available, and hence it cannot be determined if a particular fit corresponds to the physical states present. For example, the fit obtained using the T-matrix parameterization above gave a good χ^2 per degree of freedom, but the poles of the $f_0(980)$ produced by this fit were very far from the physical position of the $f_0(980)$ in the complex s plane. Adding further poles only worsens this problem.

To summarize, although the fit to the T matrix formalism without a term to describe directly the $f_0(1500)$ has a reasonable fit probability, it leads to S matrix pole postions which are inconsistent with the physical $f_0(980)$. This suggests that there are other states which affect the fit parameters, but which are difficult to include in a single-channel fit.

There are many other ways to parameterize the S-wave mass spectrum. Ishida *et al.* [75] claim that the related central $\pi^0\pi^0$ mass spectrum can be fitted using only Breit-Wigners to describe the $f_0(980)$, the $f_2(1270)$ and a very wide ($\sim$ 500 MeV/c^2) state at low mass ($\sim$ 500 MeV/c^2), and they also claim that unitarity can be applied to this method directly. Morgan and Pennington [76] have published further refinements to their previous methods, again to be used in multi-channel fits. This is supposed to enforce unitarity rigourously for all channels. The parameterizations applied above do not satisfy unitarity completely, since they are fits to only one channel from one production mechanism. It would certainly be interesting to include the WA91 data in a full analysis of several data sets coming from different reactions using a unitarized fitting procedure. The most appropriate method to do this would be to apply the T matrix formalism discussed above.

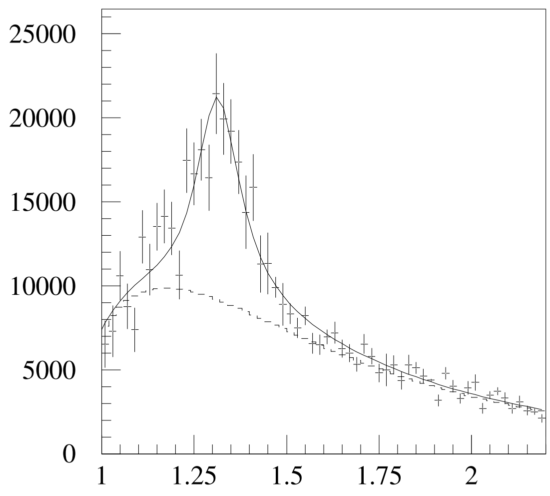

Figure 6.21: Fit to the D-wave mass spectrum. The dashed line represents the background contribution.

6.5 Parameterization of the D-Wave

The D wave mass spectrum has been fitted in the region $1.0 < m_{\pi^+\pi^-} < 2.2$ GeV/c^2 using a relativistic spin-2 Breit-Wigner to describe the $f_2(1270)$ and non-interfering background of the form $(m - m_{th})^{\alpha} e^{\beta m + \gamma m^2}$. This gives the fit shown in figure 6.21, with parameters for the $f_2(1270)$,

$$\begin{aligned} m_{f_2} &= 1.31 \pm 0.02 \text{ GeV}/c^2 \\ \Gamma_{f_2} &= 0.15 \pm 0.04 \text{ GeV}/c^2, \end{aligned}$$

which are to be compared with the Particle Data Group values $m = 1275 \pm 5$ MeV/c^2 and $\Gamma = 185 \pm 20$ MeV/c^2 [4]. The χ^2 per degree of freedom for this fit is ~ 1.67.

6.6 Conclusions

The angular distributions from the $\pi^+\pi^-$ mass spectrum have been acceptance corrected, and these have been used to calculate the moments. Taking into account the effect of the $\omega(783)$ reflection coming from the $\pi^+\pi^-\pi^0$ channel, the moments have been fitted according to the parameterization developed in chapter 5. This leads to reasonable fit qualities in most mass bins, and allows a study the variation of each partial wave with mass to be performed. Below 1 GeV/c^2, the $\pi^+\pi^-$ channel is dominated by S wave, with a smaller amount of P wave. Above 1 GeV/c^2, the D wave $\mathrm{f}_2(1270)$ state is clearly seen.

Two parameterizations have been used to fit the S-wave mass spectrum. If the same parameterization is used as that for the fit to the total mass spectrum, it is found that the fit quality can be improved considerably by the inclusion of a state interfering with the S-wave background at around 1.5 GeV/c^2, with a width of around 200 MeV/c^2. A fit to poles of the K-matrix finds that if no other states are included besides the $\mathrm{f}_0(980)$ interfering with the background, the poles of the $\mathrm{f}_0(980)$ in the complex s plane are inconsistent with the physical pole positions, suggesting that further poles may need to be added in this formalism. It is not easy to do this in a way which gives reasonable fit convergence, although this problem could possibly be overcome by performing a unitarized multi-channel fit, at least to the centrally produced $\pi\pi$ and $\mathrm{K\overline{K}}$ systems. It would also be interesting to include data from other reactions, such as $\pi\pi \longrightarrow \pi\pi$ or $\pi\pi \longrightarrow \mathrm{K\overline{K}}$ scattering.

Chapter 7

Study of Trigger Types in the 1994 $\pi^+\pi^-$ Channel

7.1 Introduction

Data were taken by the WA91 collaboration in 1994 at the same incident beam momentum as 1992 of 450 GeV/c, equivalent to a $\sqrt{s}$ of 28 GeV. The experimental layout for the 1994 run is shown in figure 7.1. The most important difference between the 1992 and 1994 runs is the inclusion of the two Čerenkov detectors in 1994; these were used in order to give access to channels such as $\mathrm{K\overline{K}}$. The 1994 trigger for $\pi^+\pi^-$ events is essentially the same as the 1992 trigger. However, improvements were made in the conditions for triggering on events with slow particles in the right-hand slow detection system (*i.e.*, box right, C right MWPCs and SPC(R)). This resulted in improved statistics in the RL and RR channels. Furthermore, the elastic veto in the LR and RL channels was made easier to interpret by requiring that in these cases a hit was recorded in the downstream hodoscope HY1, leading to further improvements in the statistics for RL and LR triggers.

A $\pi^+\pi^-$ mass spectrum was obtained from these data using similar cuts to those

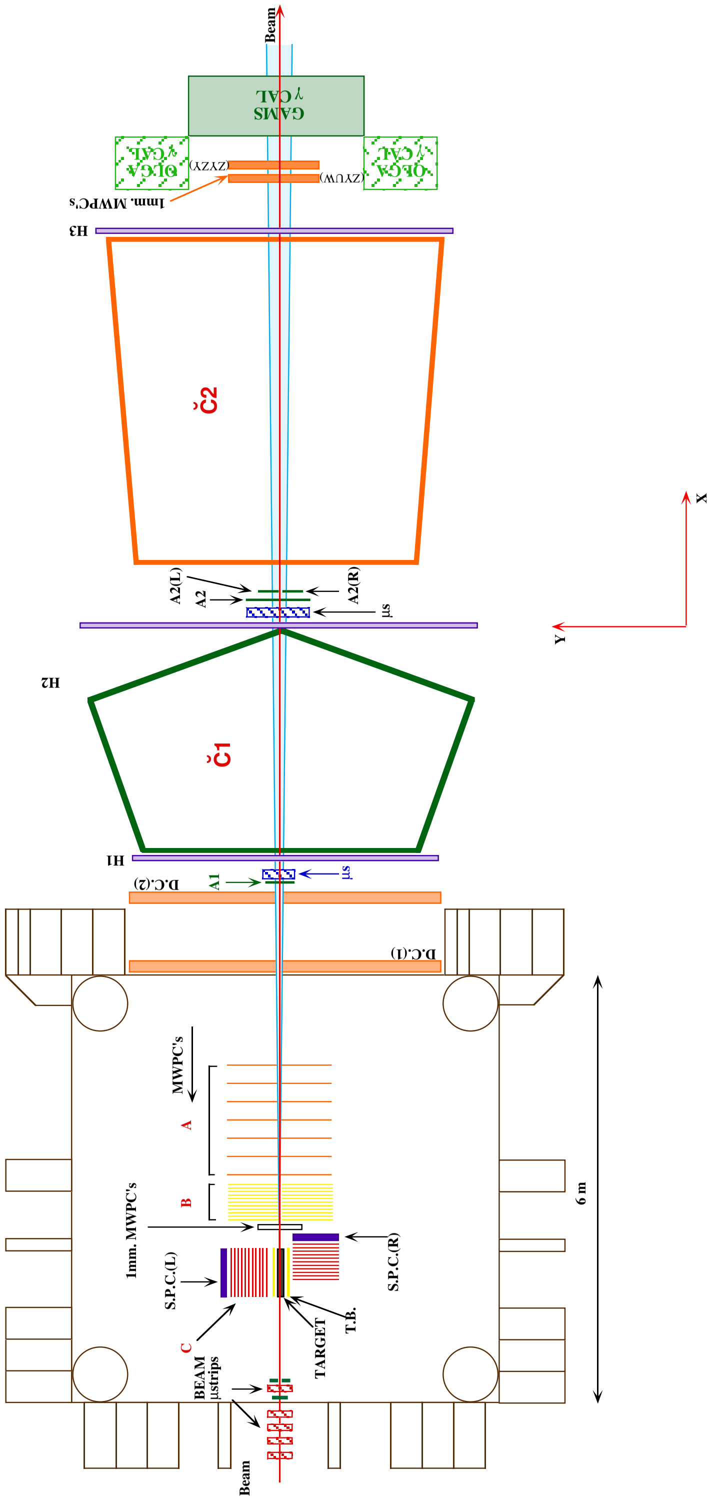

Figure 7.1: WA91 1994 experimental layout.

used in the analysis of the 1992 data, that is reactions of the type

$$\mathrm{pp} \longrightarrow \mathrm{p}_f\ (\pi^+\pi^-)\ \mathrm{p}_s\ ,$$

where the subscripts f and s refer to the fastest and slowest particles in the laboratory frame respectively, were selected from the sample of four-prong events by requiring

$$\begin{aligned} |\text{missing } p_x| &< 14.0\ \mathrm{GeV}/c, \\ |\text{missing } p_y| &< 0.16\ \mathrm{GeV}/c, \\ |\text{missing } p_z| &< 0.08\ \mathrm{GeV}/c, \end{aligned}$$

where $|\text{missing } p_i|$ is defined by

$$\text{missing } p_i = p_{i_b} - p_{i_f} - p_{i_s} - p_{i_{\pi+}} - p_{i_{\pi-}},$$

and the subscript b refers to the incident beam track,

$$-0.3\ \mathrm{GeV}^2/c^4 < (\text{Ehrlich Mass})^2 \leq 0.16\ \mathrm{GeV}^2/c^4,$$

and finally

$$\begin{aligned} m_{\mathrm{p_f}\pi^+} &> 1.5\ \mathrm{GeV}/c^2, \\ m_{\mathrm{p_f}\pi^-} &> 1.5\ \mathrm{GeV}/c^2, \\ m_{\mathrm{p_s}\pi^+} &> 1.5\ \mathrm{GeV}/c^2, \\ m_{\mathrm{p_s}\pi^-} &> 1.5\ \mathrm{GeV}/c^2, \end{aligned}$$

in order to reduce the diffractive contributions to the pπ channels. Plots of the missing momentum components, the Ehrlich Mass and the pπ mass spectra are shown in figures 7.2, 7.3 and 7.4, compared with the same variables after the cuts.

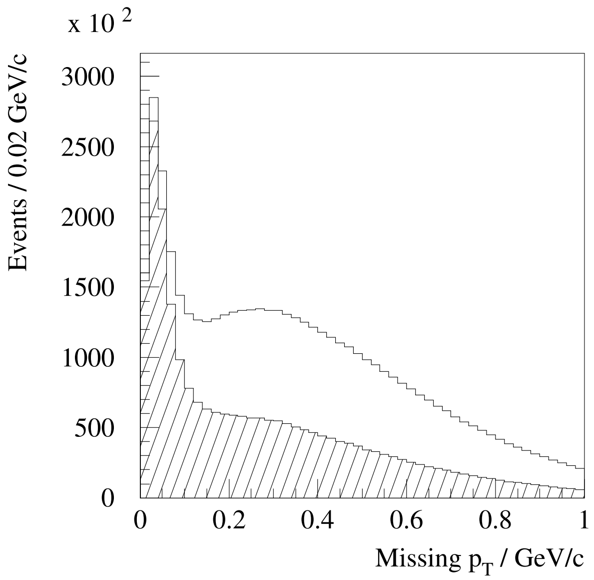

(a) Missing p_T

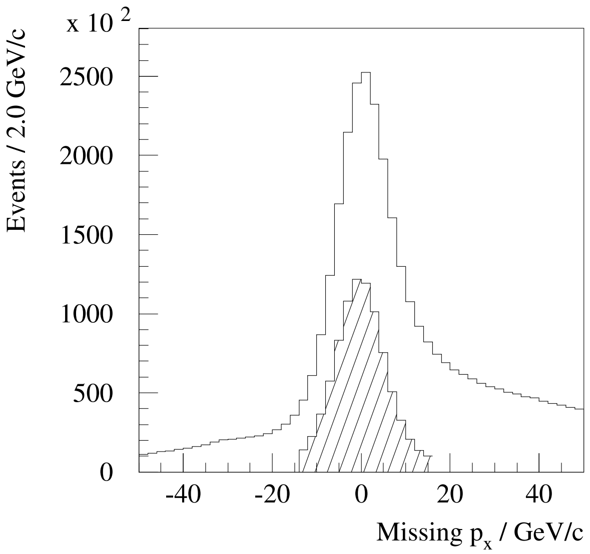

(b) Missing p_x

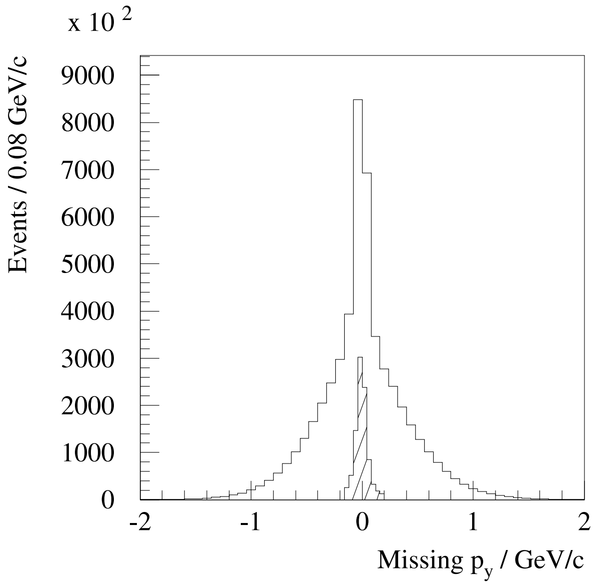

(c) Missing p_y

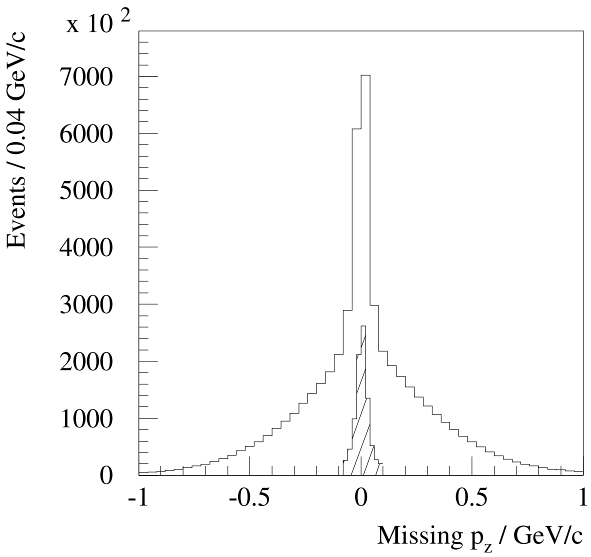

(d) Missing p_z

Figure 7.2: Missing momentum components. The shaded areas show the events selected by the cuts described in the text. a) Missing p_T with p_x cut, b) missing p_x with p_T cut, c) missing p_y, d) missing p_z.

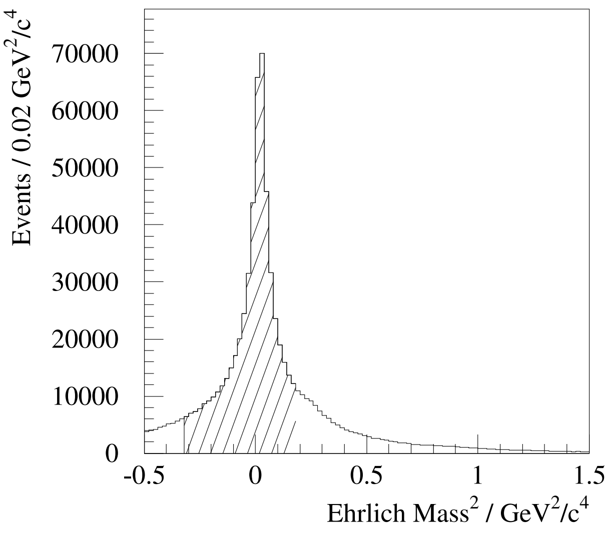

Figure 7.3: Ehrlich Mass. The shaded area shows the events selected by the cuts described in the text.

A comparison between the 1992 and 1994 $\pi^+\pi^-$ mass spectra obtained after these cuts is shown in figure 7.5, where an enhancement of the $\rho(770)$ and $f_2(1270)$ signals is observed in the 1994 sample. In order to understand this, it is important to note that the 1992 data are essentially all LL triggers; as mentioned above an important improvement in the 1994 data was the increase in statistics for all trigger types. This allows us to divide the 1994 data into LL, RR, RL and LR trigger types with enough events in each to allow separate analyses to be done. If this distinction is made, and the $\pi^+\pi^-$ mass spectrum for the 1994 data is replotted as a function of trigger type, the excess $\rho^0(770)$ and $f_2(1270)$ production in the 1994 data is seen to be due to the RL and LR triggers, as shown in figure 7.6.

7.2 Trigger Effects

At least one of the pions in the LR and RL triggers is required to hit HY1, and it may be that this has an effect on the mass distributions for these trigger types.

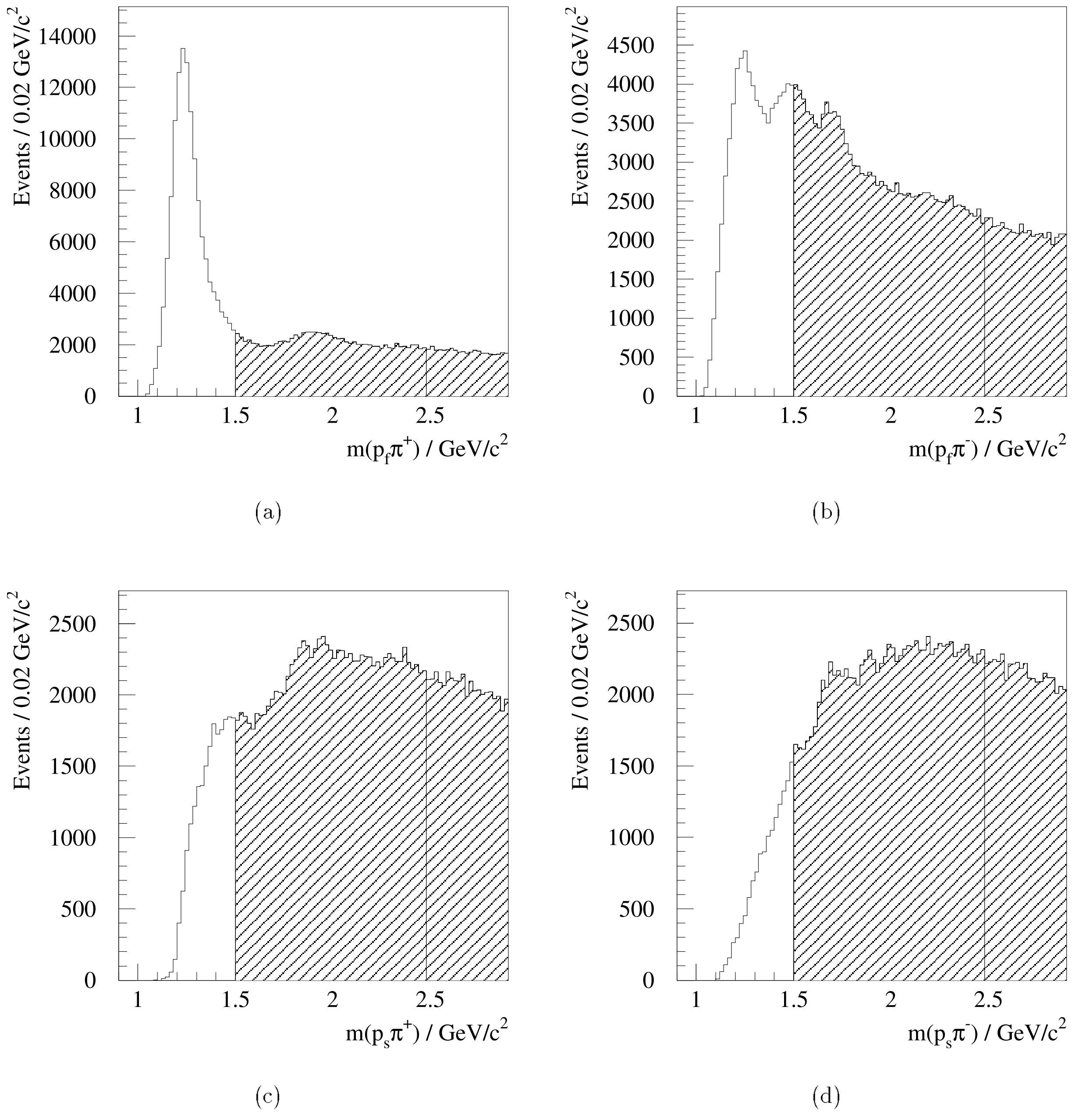

Figure 7.4: $p\pi$ mass spectra. The shaded areas show the events selected by the cuts described in the text.

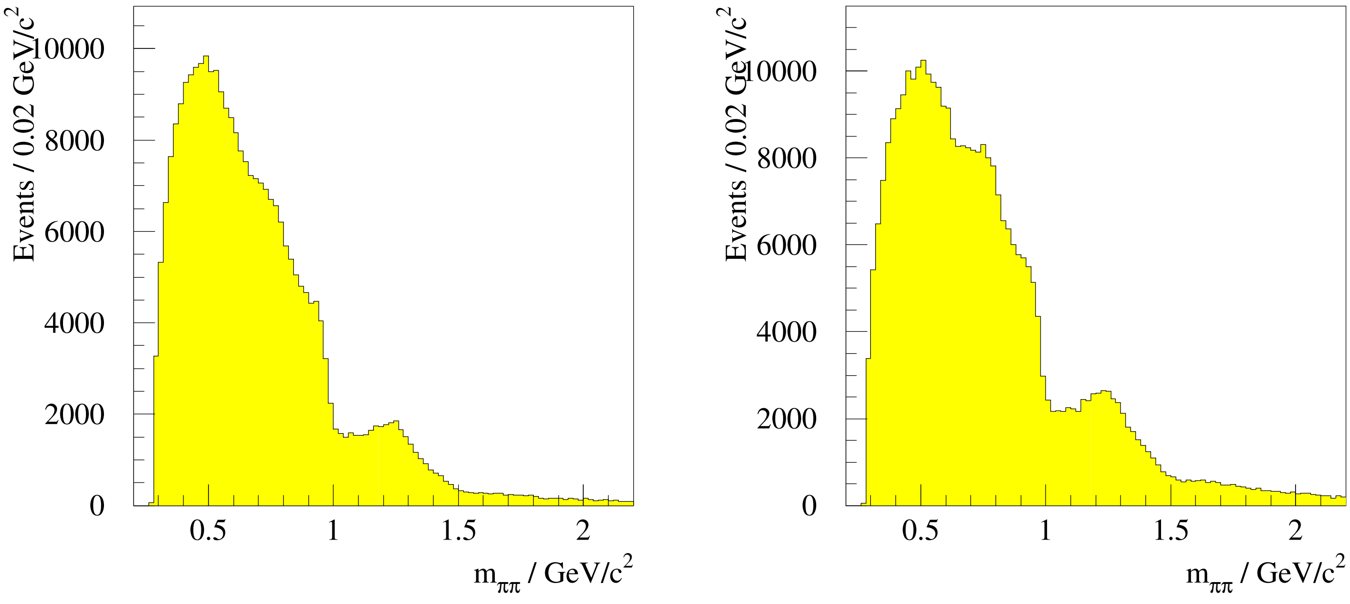

(a) 1992 data (b) 1994 data

Figure 7.5: $\pi^+\pi^-$ Mass Spectra.

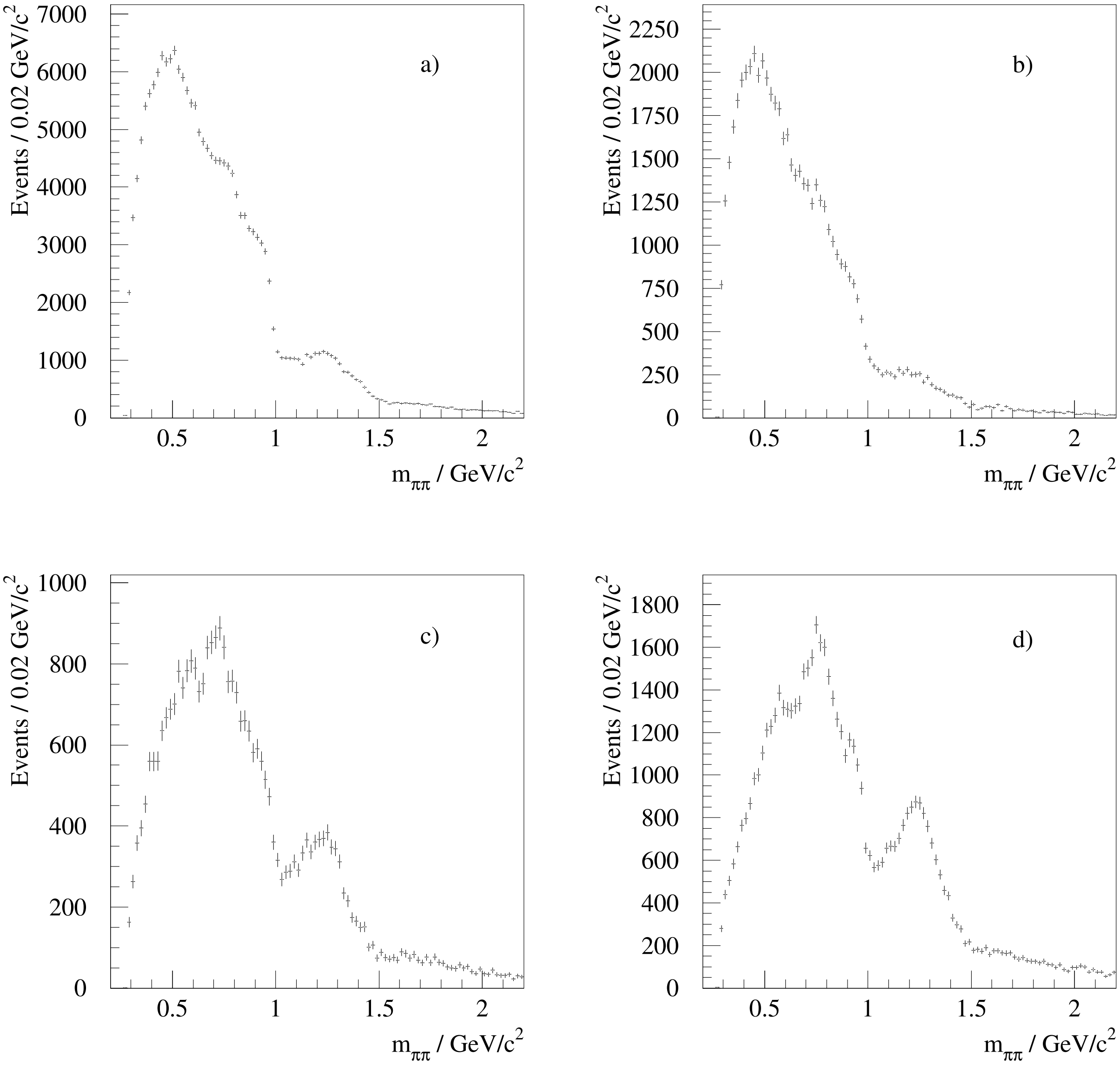

Figure 7.6: $\pi^+\pi^-$ mass spectra for given trigger type a) LL, b) RR, c) RL and d) LR.

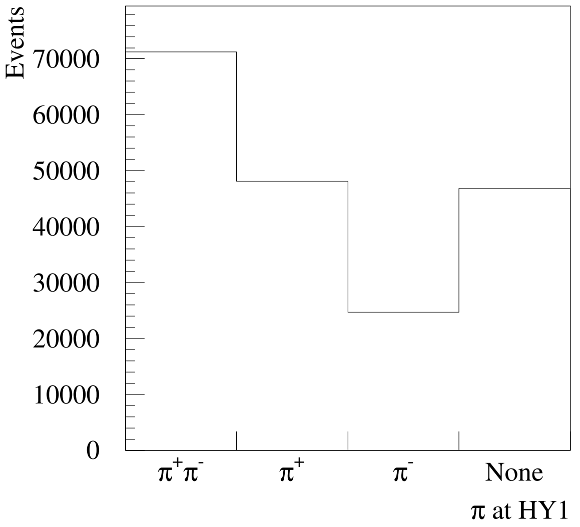

(a) LL

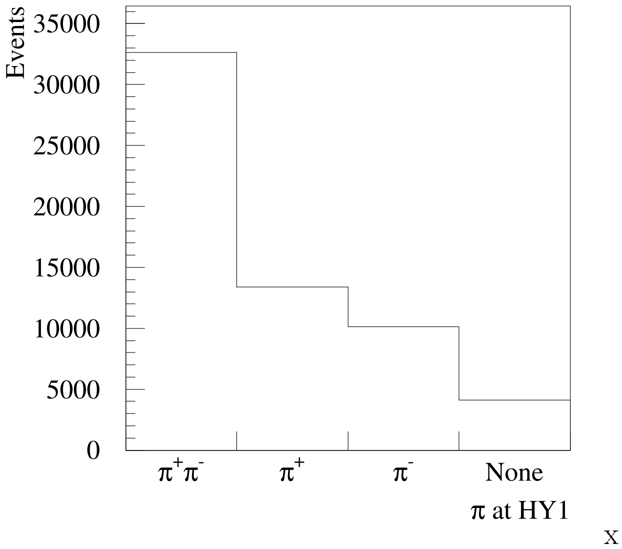

(b) LR

Figure 7.7: π hits at hodoscope 1.

By tracing data from the interaction vertex to the hodoscope plane, it can be calculated how often 0, 1 or 2 pions reach the hodoscope. These relative proportions for LL and LR events are shown in figure 7.7, where it may be seen that it is more likely for both pions to reach the hodoscope plane in LR events than in LL. The small proportion of events in the LR triggers where no pions apparently reach the HY1 plane are due to tracing errors and hodoscope noise, and it is found that of these events, $\sim 95\%$ are in fact associated with a signal in the hodoscope. Plots of the mass spectra as a function of number of pions tracing to the hodoscope are shown in figure 7.8 for both LR and LL events. It is clear that requiring the same trigger condition on the LL events as on the LR (*i.e.*, that at least one pion must reach HY1) does not produce a good agreement between the forms of the two mass spectra.

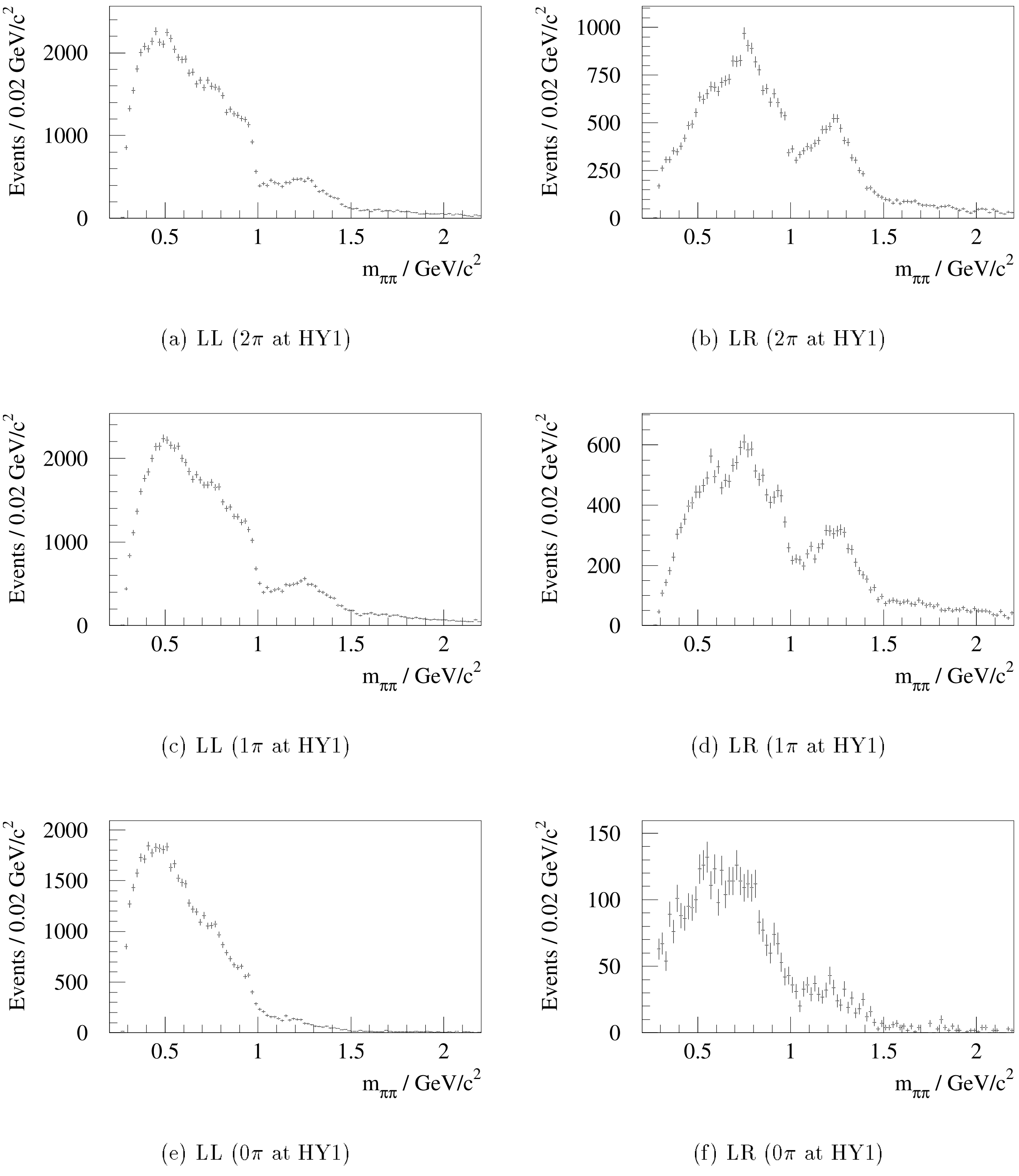

(a) LL (2π at HY1)

(b) LR (2π at HY1)

(c) LL (1π at HY1)

(d) LR (1π at HY1)

(e) LL (0π at HY1)

(f) LR (0π at HY1)

Figure 7.8: Mass spectra for triggered LL and LR events where 2, 1 or 0 π tracks reach HY1.

7.3 Trigger Classification of Events

In practice, it has been found that fast tracks are often tagged by the trigger in a way which does not correspond to the physical directions taken by the fast and slow tracks from the interaction vertex. To see why this happens, consider some simple examples. First recall that the y-direction in the Ω coordinate system is in the sense that positive y lies to the left of the x-axis. Now consider an event where both the fast and slow protons are produced with $p_y > 0$ GeV/c (*i.e.* travelling to the left). The slow proton will always trigger left, because there is good spatial separation of the slow left and slow right trigger elements. The fast proton will also trigger left (that is it will hit A2L), since positively charged particles bend to the left in the Ω magnetic field. Thus an event where both the fast and the slow particles are produced with $p_y > 0$ GeV/c must, if it triggers at all, trigger LL, as shown in figure 7.9 a.

However, now consider the case where the slow proton is again produced with $p_y > 0$ GeV/c, but the fast proton has $p_y < 0$ GeV/c, that is to say a fast right. Again, the slow proton will trigger left, but now the fast proton, depending on its momentum, may in fact bend round in the field to such an extent that it crosses the $p_x = 450$ GeV/c line (*i.e.*, $p_y = 0$) and hits A2L. This means that an event which should be recorded as being LR, can trigger LL. This is illustrated in figure 7.9 b.

It is convenient at this stage to introduce the variable $p_{y_{rel}}$. This is defined to be the p_y of the fast track relative to the p_y of the beam, *i.e.*,

$$p_{y_{rel}} = p_{y_f} - p_{y_b},$$

where p_{y_f} and p_{y_b} refer to the y-component of the fast track and beam momentum respectively (note that both are in general small). This variable enables us to define the 4 types of events independently of how they actually triggered. (Note again that it is easy to determine whether the slow proton is of the left or right type, since the

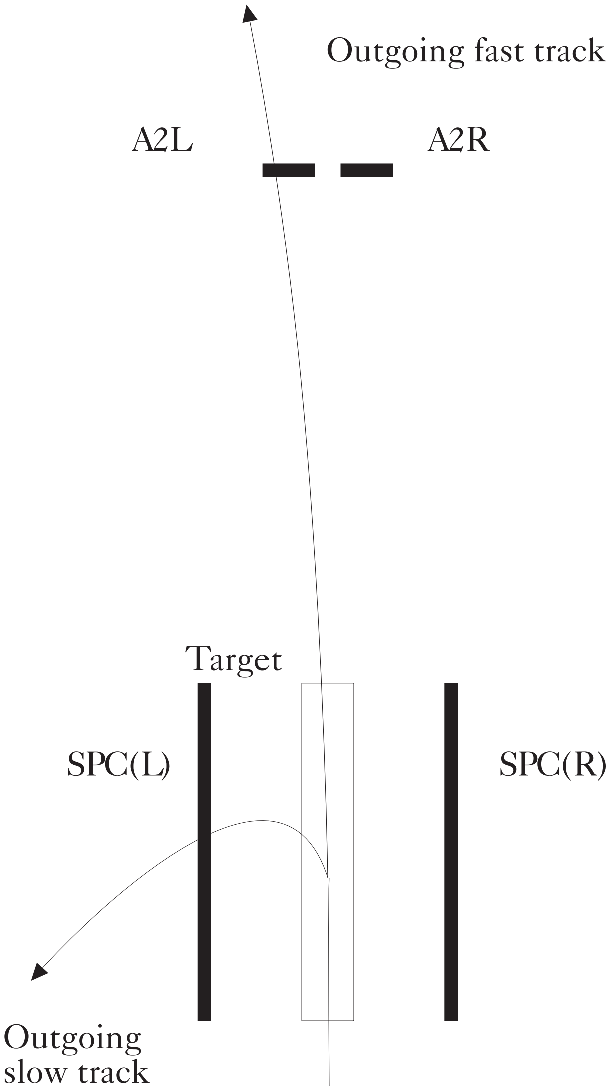

(a) True LL event, triggered LL

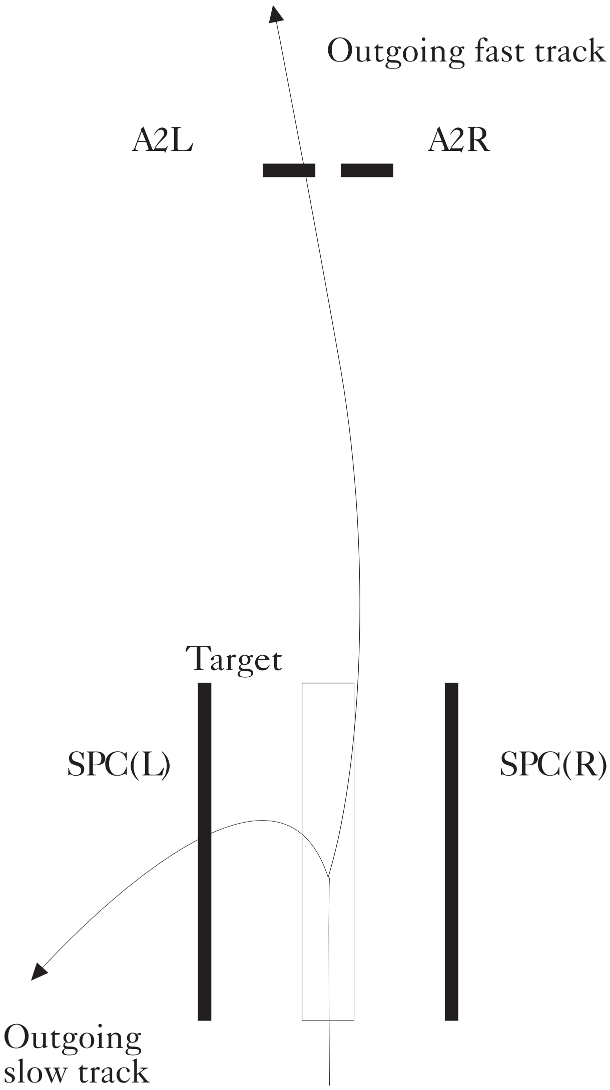

(b) True LR event, triggered LL

Figure 7.9: Difference between real and mismatch LL events.

two parts of the slow proton detection system are well separated spatially.) Using $p_{y_{rel}}$, it may be determined how often a "true" event of a particular type triggers as being a different classification. It is found that for RR and LR triggers, mismatching of the trigger type occurs around 30% of the time. Therefore, $p_{y_{rel}}$ should be used to define the trigger classification, and the fast trigger system should not be relied on to perform this task. Using this new definition of the trigger types, the $\pi^+\pi^-$ mass spectra may be re-examined. These are presented in figure 7.10, again for the cases where two πs, one π or no πs trace to HY1. Figure 7.10 clearly shows that even if only true LL and LR events are considered, then using the same trigger conditions on HY1, there is still an excess of $\rho^0(770)$ and $f_2(1270)$ production in the LR case. Indeed, by comparing figure 7.10 with figure 7.8, it is seen that the small $\rho^0(770)$ signal present in the triggered LL events where at least one pion traces to HY1 has been reduced in the real LL events defined by $p_{y_{rel}}$. This suggests that the $\rho^0(770)$ in triggered LL is due predominantly to real LR events that have been incorrectly classified by the fast trigger system. In conclusion, the enhancements in the $\rho^0(770)$ and $f_2(1270)$ mass regions are not due to trigger effects.

7.4 4-Momentum Transfer Dependence

In central production, it has been observed by the WA76 collaboration [43] that the amount of $\rho^0(770)$ production varies with the 4-momentum transfer at the vertices, and specifically that the $\rho^0(770)$ signal to background ratio is larger at higher t in the $\pi^+\pi^-$ channel. Therefore, it is important to test whether the LL/RR triggers are biased to low t, and equivalently whether LR/RL triggers are biased to high t, thus selecting DPE or Reggeon-Reggeon/Reggeon-Pomeron Exchange respectively.

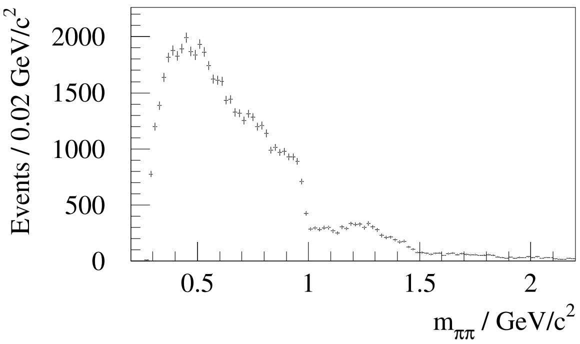

(a) Real LL (2π at HY1)

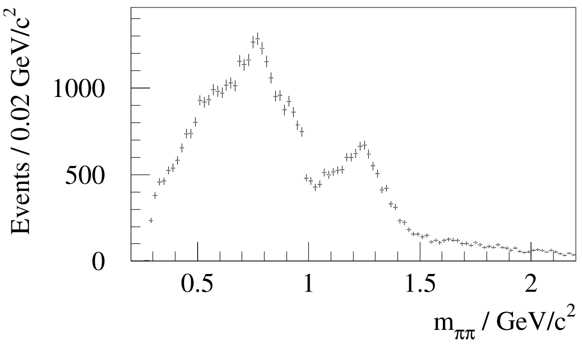

(b) Real LR (2π at HY1)

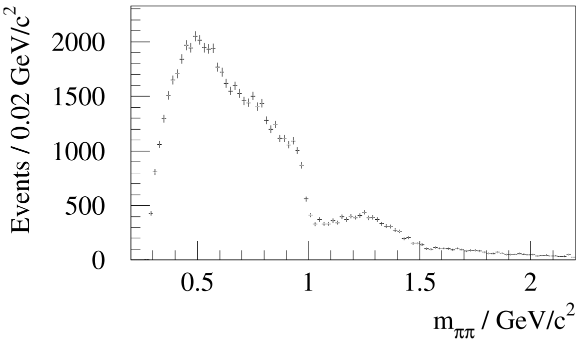

(c) Real LL (1π at HY1)

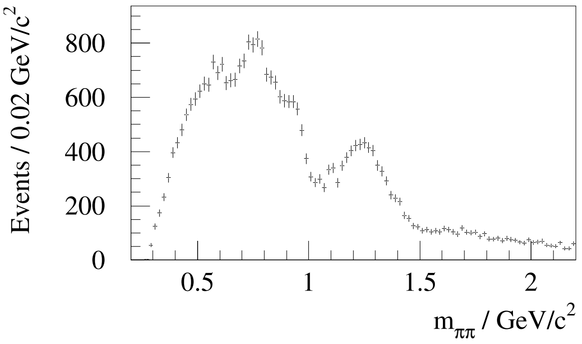

(d) Real LR (1π at HY1)

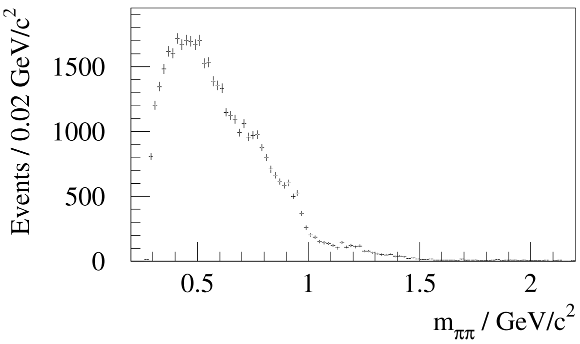

(e) Real LL (0π at HY1)

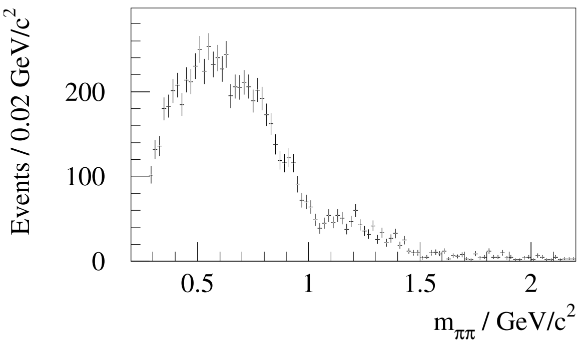

(f) Real LR (0π at HY1)

Figure 7.10: Mass spectra for real LL and LR events where 2, 1 or 0 π tracks reach HY1.

7.4.1 Monte Carlo Sample

In order to do this, a set of simulated data are generated under the assumption that there is no correlation between the fast and slow vertices, as expected for DPE, using the event generator described in section 6.1. A new set of acceptance tables is made using the 1994 positions of the detectors used in the trigger, including a table to describe the slow right system. For the 1994 run, the slow trigger was changed slightly so that slow lefts were required to trace through TB(1), CL(7), CL(10) and SPC(L), and slow rights through TB(2), CR(8), CR(10) and SPC(R) (*cf* section 6.1).

In the reconstruction of slow rights, it was found that tracks may have satisfied the trigger conditions, but were not in fact reconstructable by TRIDENT since they did not pass through enough planes of the C chambers (see figure 3.3). However, statistics for such events were improved by reconstructing the z coordinate in the B chambers where possible. This has been incorporated into the acceptance tables by requiring slow right tracks to satisfy the usual trigger conditions described above, and at the same time requiring that they either trace through five C chambers, or that they trace into the B chambers, that is,

(TB(2) AND CR(8) AND CR(10) AND SPC(R)) AND ((Traces through 5 C chambers) OR (Traces into B chambers)).

It has not been found necessary to include the slab efficiency as a function of slow particle momentum correction used for SPC(L) in the case of the slow right system, since the efficiencies as a function of momentum are flatter, and make little difference to the final results other than an overall loss in statistics. However, in TRIDENT it was found necessary to introduce an offset in the position of the right C chambers in order to improve the quality of the Ehrlich Mass spectrum for the 1994 data. This has the effect of underestimating the p_x of slow rights for very low p_x. Furthermore, the track reconstruction for slow rights attempts to fit the tracks

Table 7.1: Values of the slope parameter α for t in the Monte Carlo input.

Trigger	α / GeV^{-2}
Fast	8.0 ± 0.1
Slow	8.3 ± 0.1

to a circle. While this is appropriate for tracks which pass through the chambers close to the target region (where the field is approximately uniform), it gives rise to problems in the reconstruction of tracks which pass through the chambers at large y, since the field in this region is no longer uniform. Ideally, both these effects should be simulated in full, for example using GEANT [77]. However, this would require an extremely detailed study, and in order to save time all events with a slow right with $p_x < 0.075$ GeV/c and all those which pass through the chambers at $y > 65$ cm have been removed.

In order to examine the t-dependence, the $\rho^0(770)$ mass region in the $\pi^+\pi^-$ system is selected, that is the cut $0.7\ \text{GeV}/c^2 \leq m_{\pi^+\pi^-} < 0.9\ \text{GeV}/c^2$ is applied. Shown in figures 7.11 and 7.12 are the t_f and t_s distributions for the data before acceptance correction, in figure 7.13 the t distributions used as input to the Monte Carlo, and in figures 7.14 and 7.15 the t-distributions of the Monte Carlo data after the acceptance tables have been applied. Also shown are fits of the form $Ae^{-\alpha t}$ in the region $0.1\ \text{GeV}^2 \leq t < 0.6\ \text{GeV}^2$. Values of the slope parameter α for each of the plots is given in tables 7.1 and 7.2, where the errors are statistical only. For fits to the raw data, χ^2 per degree of freedom is typically ~ 1.7, while for the fits to the simulated data χ^2 per degree of freedom is much worse, typically ~ 10. This may be expected, since at very high statistics the acceptance will presumably change the slope from being a pure exponential. However, the slope can still be assumed to give some indication of how the data vary with t. By comparing the values of α in the data against those produced by Monte Carlo, it may be seen that they are not too dissimilar for the LL and RR cases, but the Monte Carlo predicts rather higher (more negative) values of α compared with the data for the LR and RL cases. This

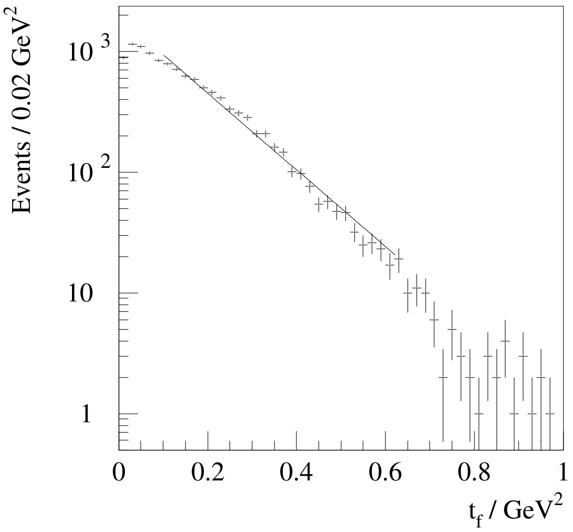

(a) LL raw data t_f

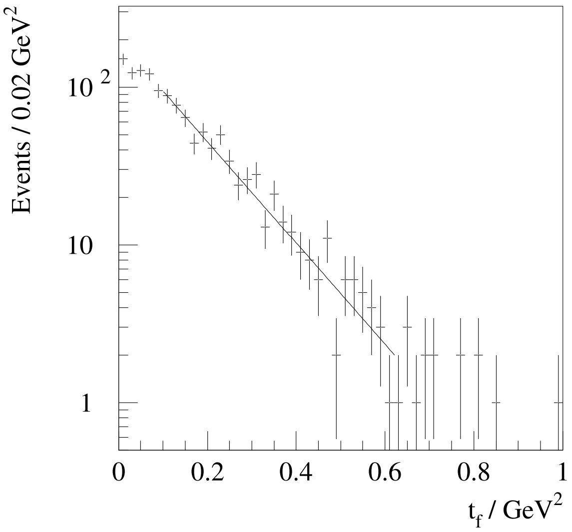

(b) RR raw data t_f

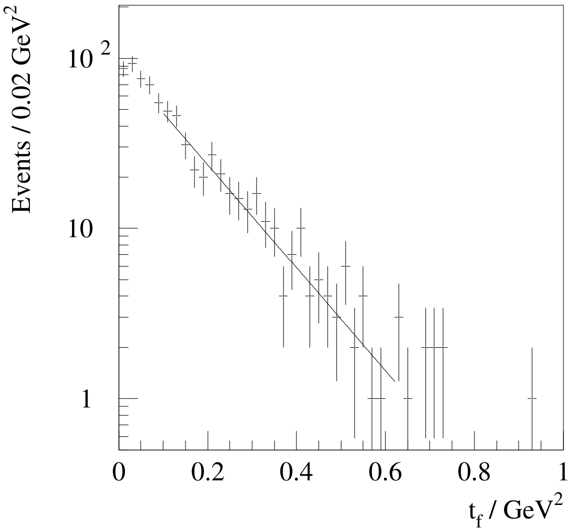

(c) RL raw data t_f

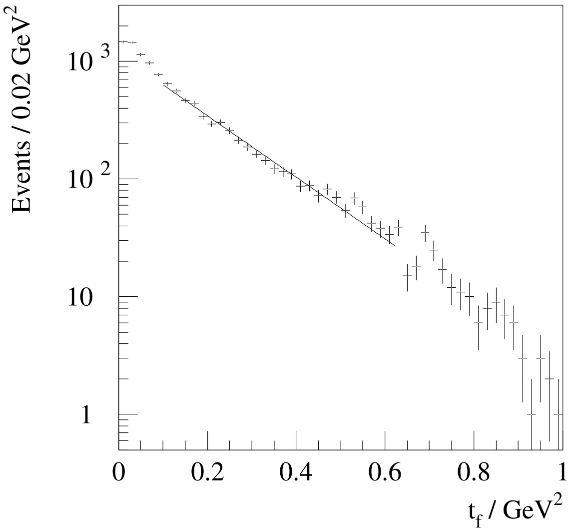

(d) LR raw data t_f

Figure 7.11: t_f distributions for the uncorrected data.

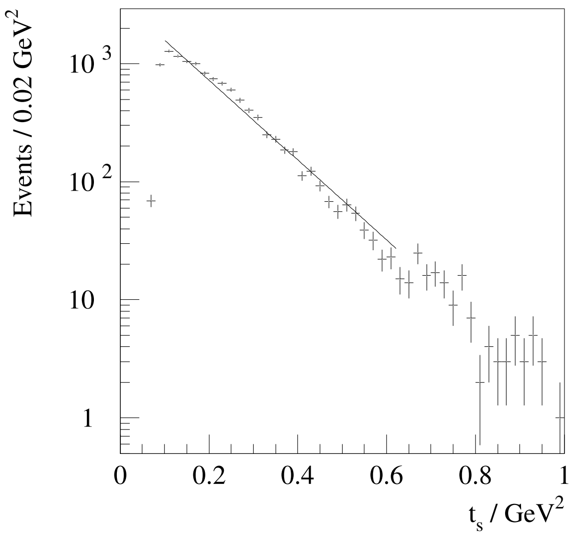

(a) LL raw data t_s

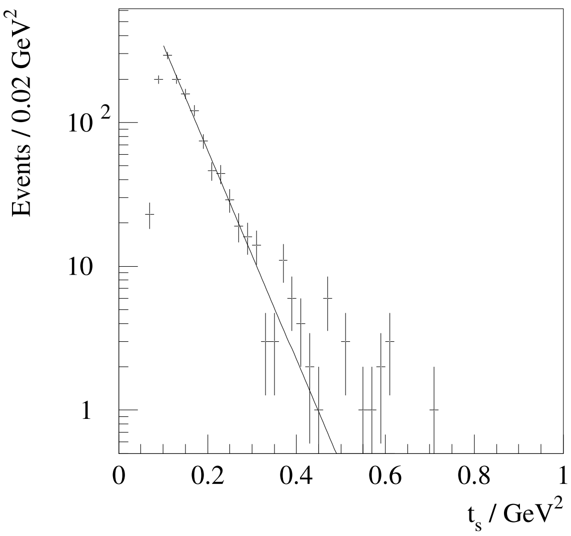

(b) RR raw data t_s

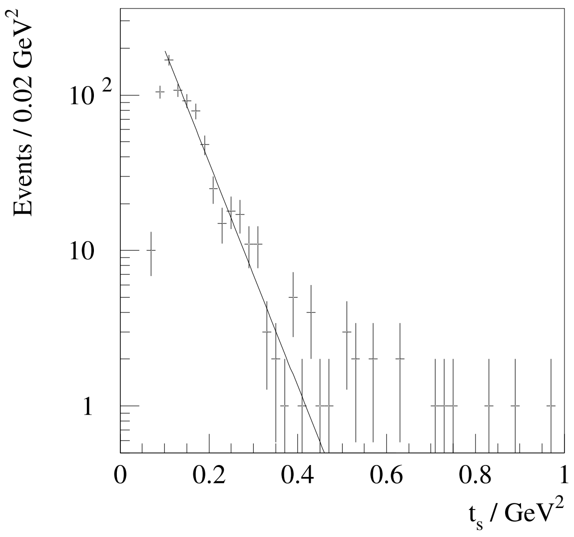

(c) RL raw data t_s

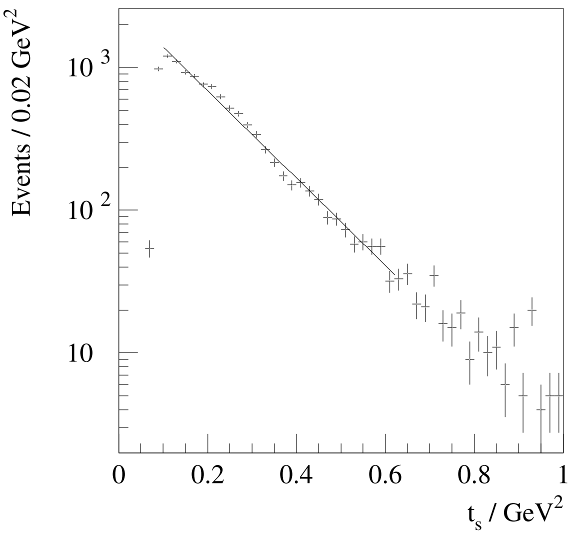

(d) LR raw data t_s

Figure 7.12: t_s distributions for the uncorrected data.

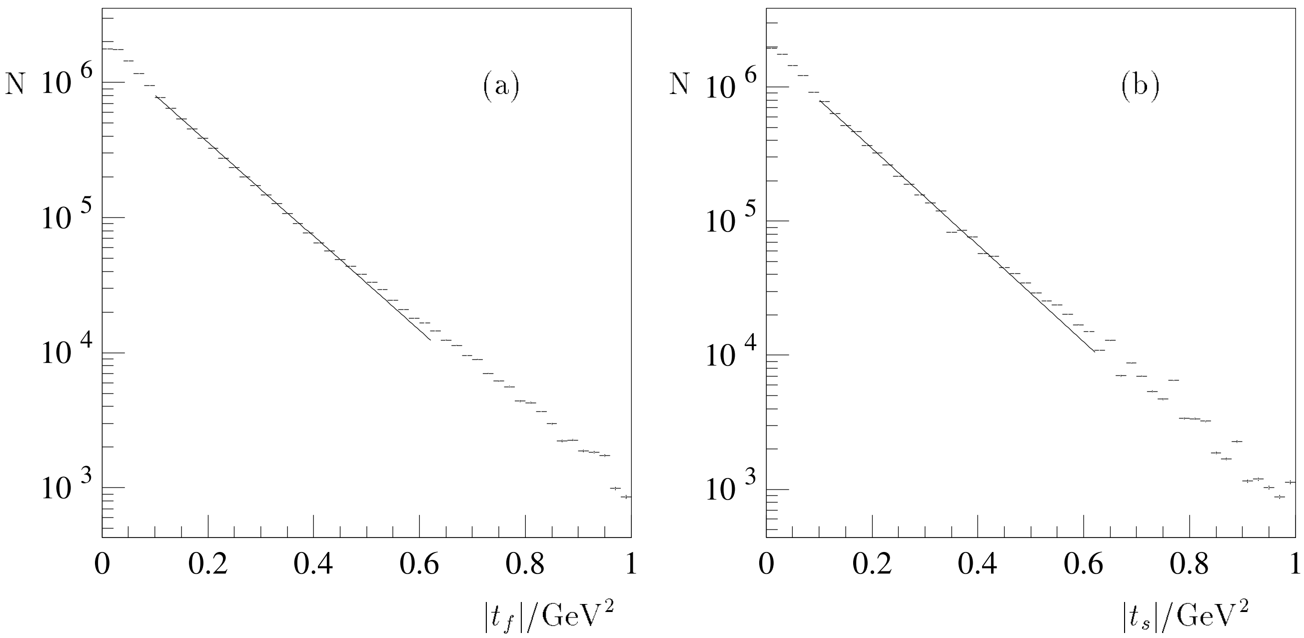

Figure 7.13: Input $|t|$ distributions generated by the Monte Carlo. (a) $|t_f|$ and (b) $|t_s|$.

Table 7.2: Values of the slope parameter α for t in the raw data.

Trigger	Uncorrected Data α / GeV^{-2}	Monte Carlo After Acceptance α / GeV^{-2}
LL fast	7.3 ± 0.1	7.62 ± 0.12
LL slow	7.80 ± 0.15	8.30 ± 0.10
RR fast	7.3 ± 0.3	7.90 ± 0.13
RR slow	11.8 ± 0.3	10.90 ± 0.11
LR fast	6.0 ± 0.1	7.95 ± 0.10
LR slow	7.1 ± 0.1	8.19 ± 0.05
RL fast	6.4 ± 0.3	7.60 ± 0.05
RL slow	11.7 ± 0.3	10.95 ± 0.08

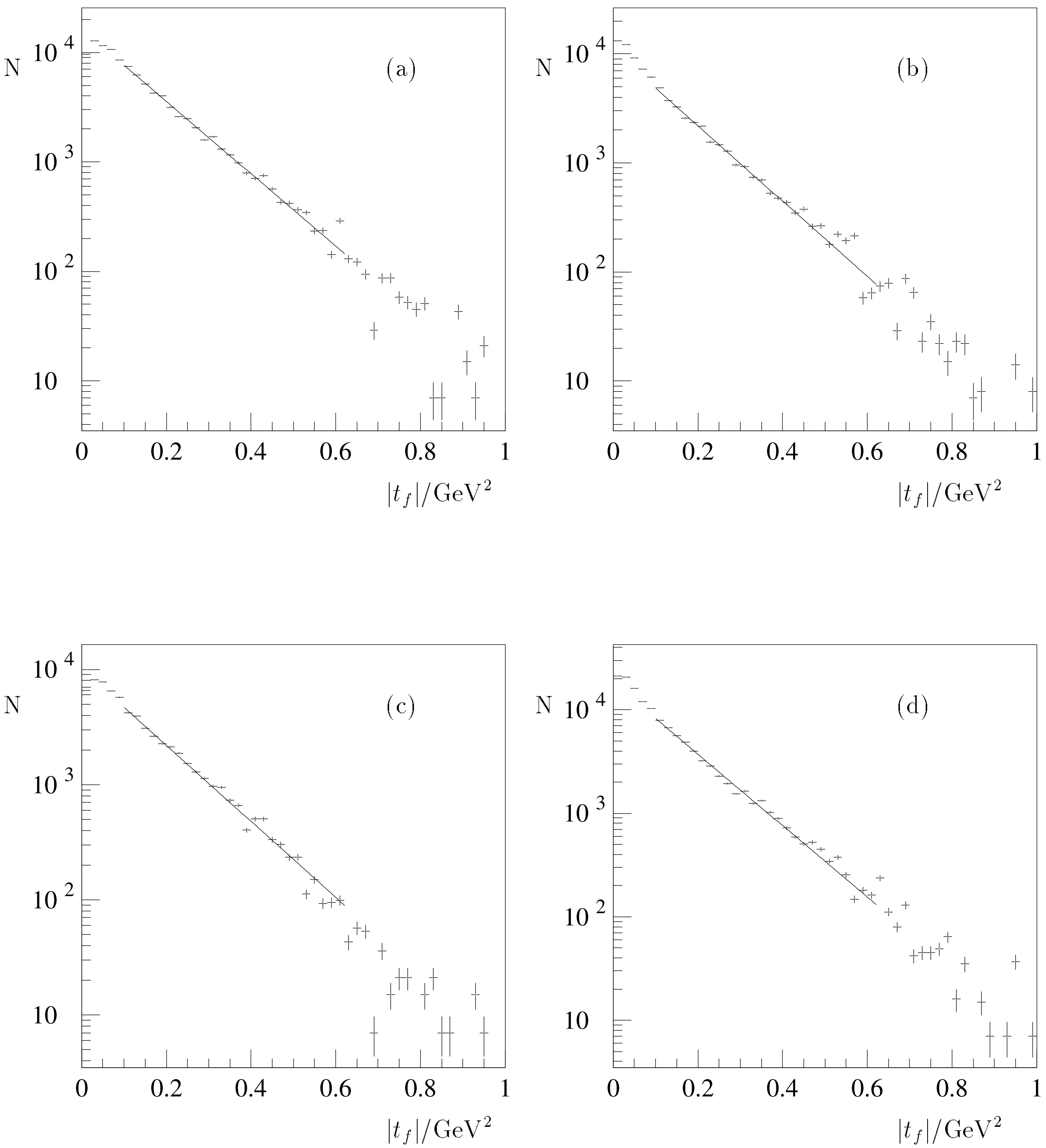

Figure 7.14: $|t_f|$ distributions from the Monte Carlo after acceptance. a)LL, b) RR, c) RL, d) LR.

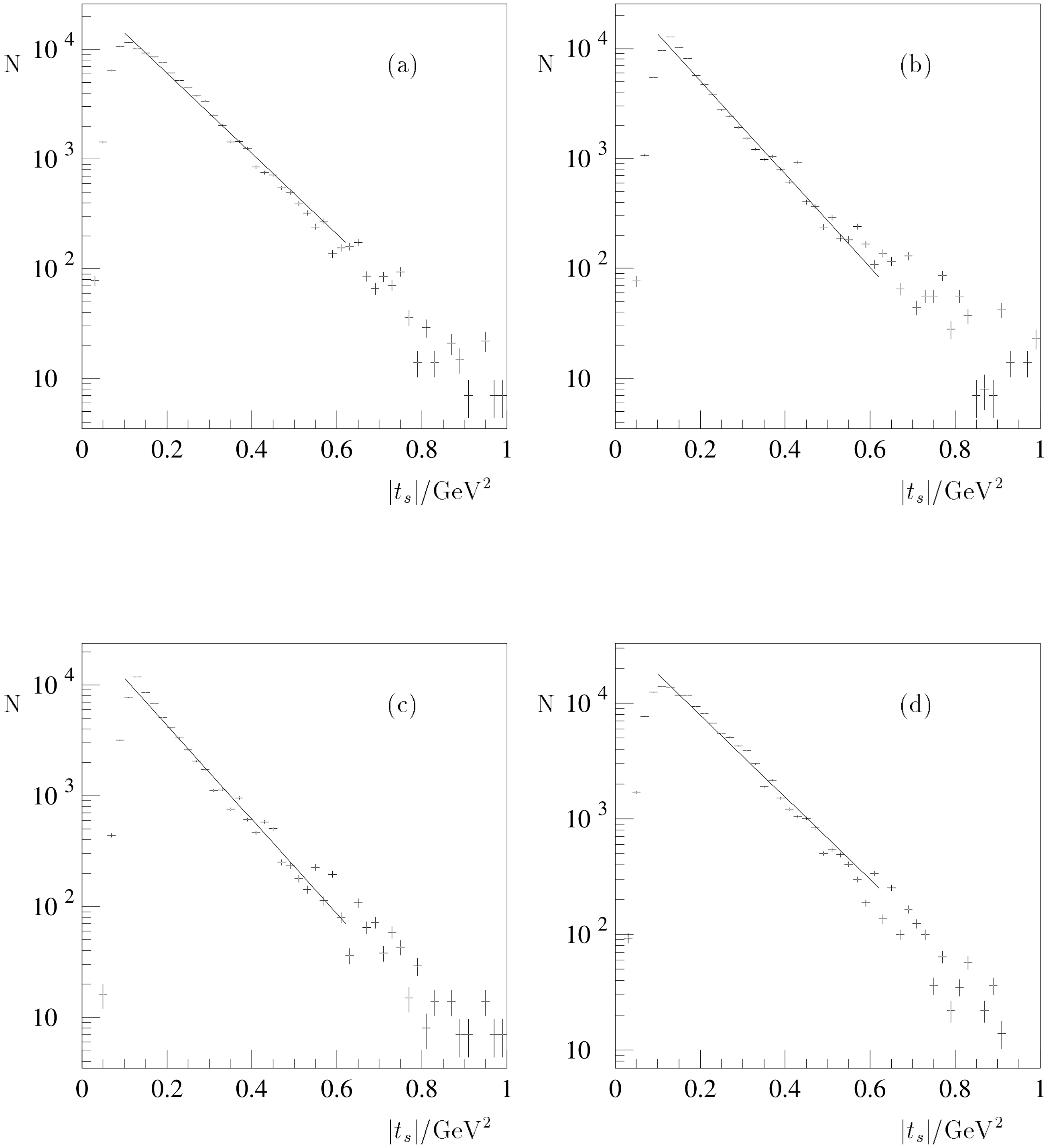

Figure 7.15: $|t_s|$ distributions from the Monte Carlo after acceptance. a)LL, b) RR, c) RL, d) LR.

Table 7.3: Values of the slope parameter α for LL and LR in the corrected data.

Trigger	α / GeV^{-2}
LL fast	-8.0 ± 0.1
LL slow	-8.0 ± 0.1
LR fast	-7.3 ± 0.1
LR slow	-7.4 ± 0.1

suggests that the assumption that there is no correlation between the vertices is incorrect.

A set of correction curves are made by dividing the Monte Carlo data after acceptance by the Monte Carlo input data. These curves (unsmoothed) are shown in figures 7.16 and 7.17. Using these curves, the data t-distributions are corrected on an "event-by-event" basis, that is each event in the data is weighted by the inverse of the relevant acceptance for that event. The fitted t-distributions for the corrected data are shown in figures 7.18 and 7.19. Values of the slope parameter α for the LL and LR corrected data are given in tables 7.3. To find these values of α, a maximum likelihood method was used. Specifically, the function to be maximised was given by

$$\ln \mathcal{L}(t_1, \ldots, t_N; \alpha) = -\sum_{i=1}^{N} W_i \ln(\mathcal{F}(t_1, \ldots, t_N; \alpha),$$

with

$$\mathcal{F}(t_1 \ldots t_N; \alpha) = N \alpha e^{\alpha(t-t_0)},$$

N being the total number of events and t_0 being the lower limit in t from where the fit begins. Maximising $\ln \mathcal{L}$ as a function of α gives an estimate of the value of α which makes this interpretation of the data most likely. This method is particularly applicable to functions which vary rapidly over the parameter space being considered (such as steep exponentials) as no information is lost through binning. However, it

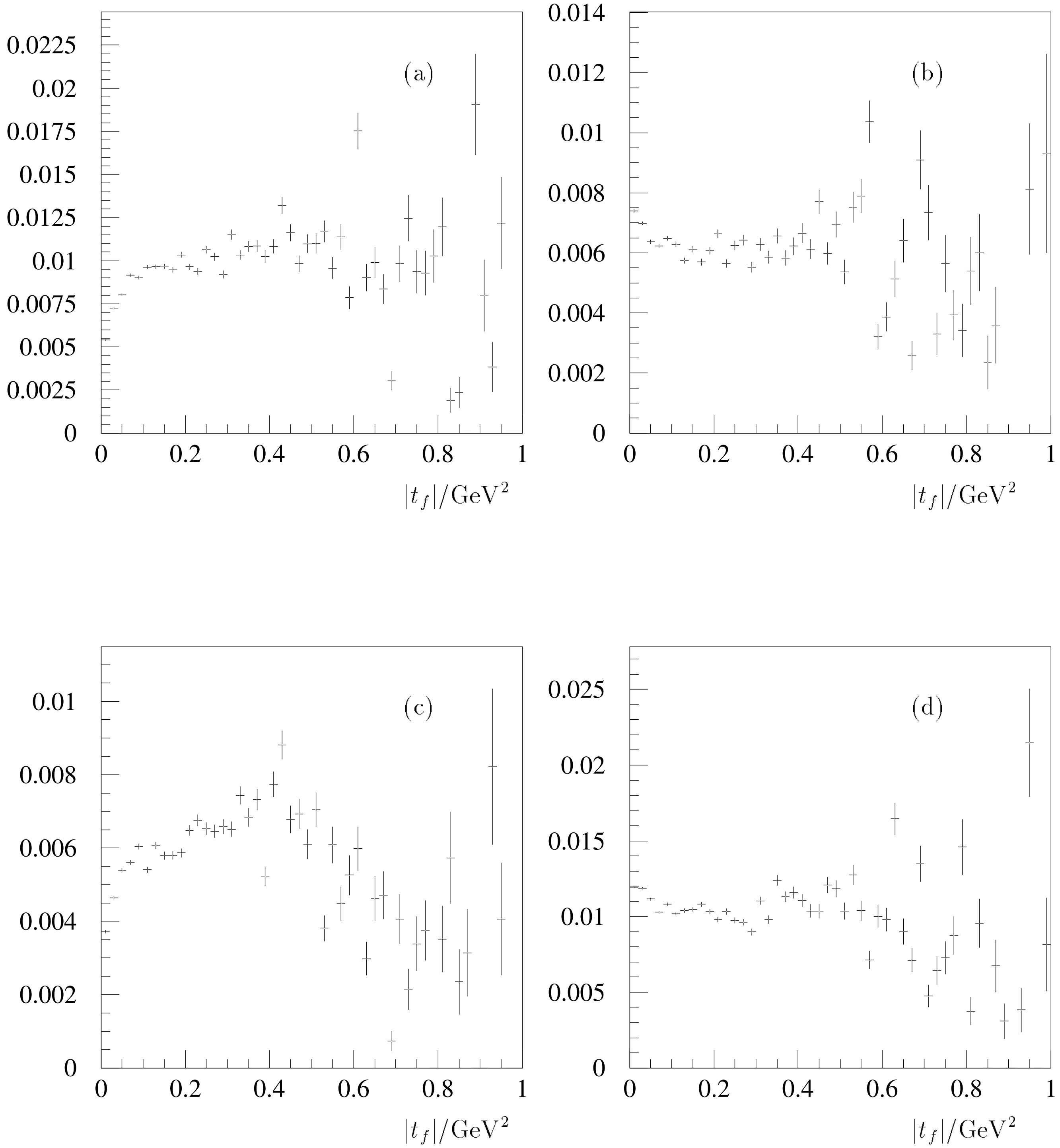

Figure 7.16: $|t_f|$ correction curves. a) LL, b) RR, c) RL, d) LR.

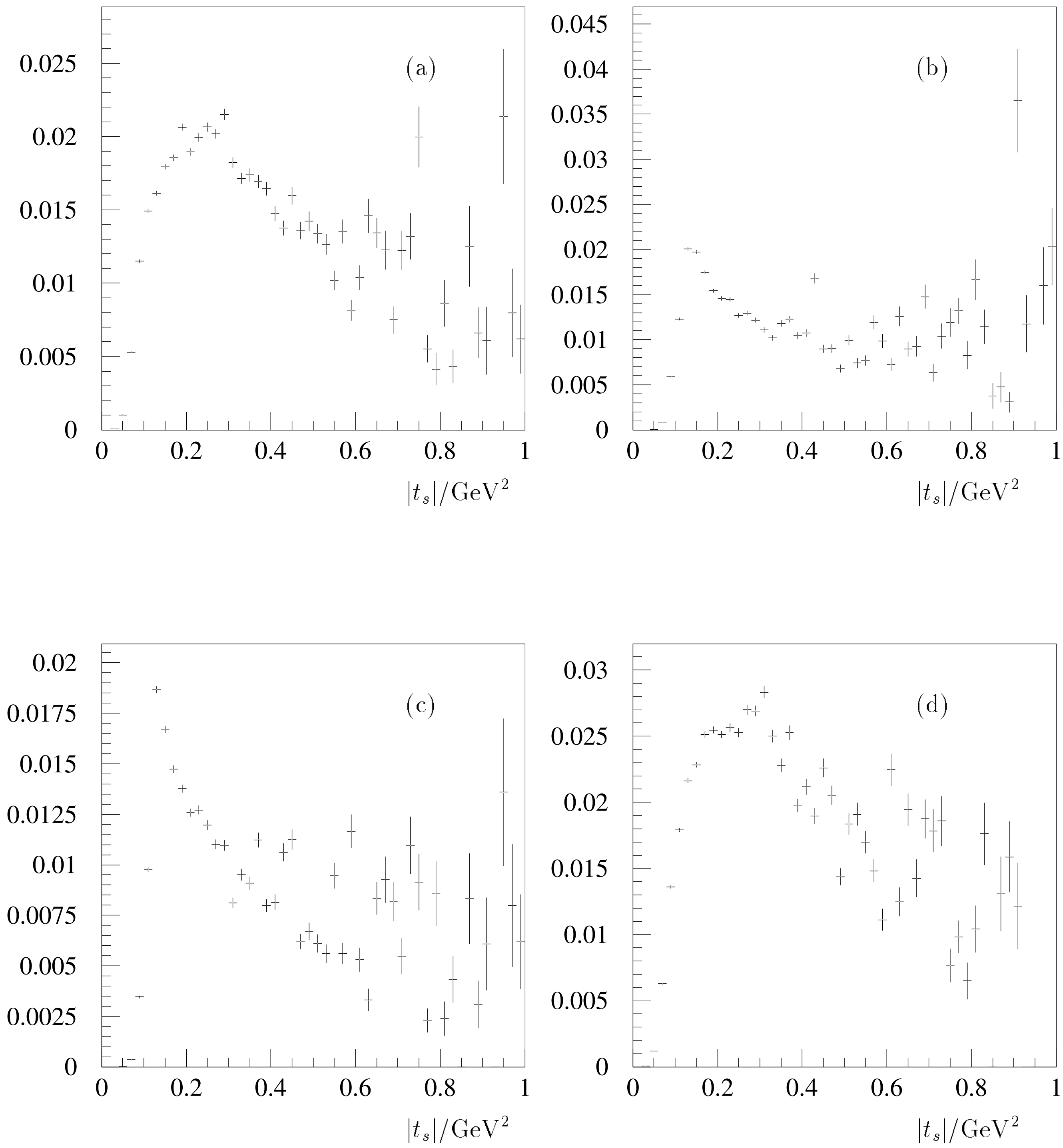

Figure 7.17: $|t_s|$ correction curves. a) LL, b) RR, c) RL, d) LR.

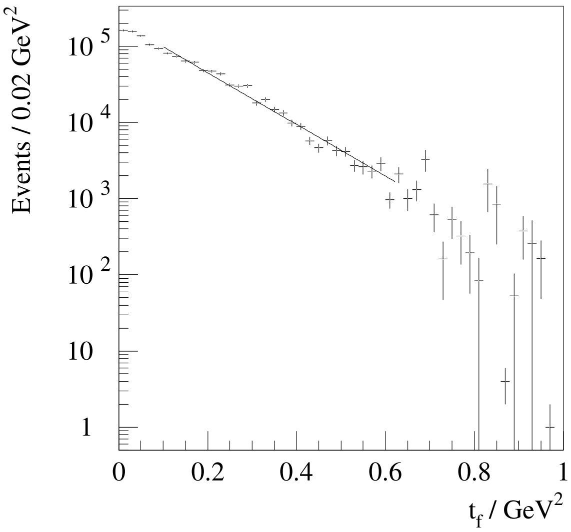

(a) LL corrected data t_f

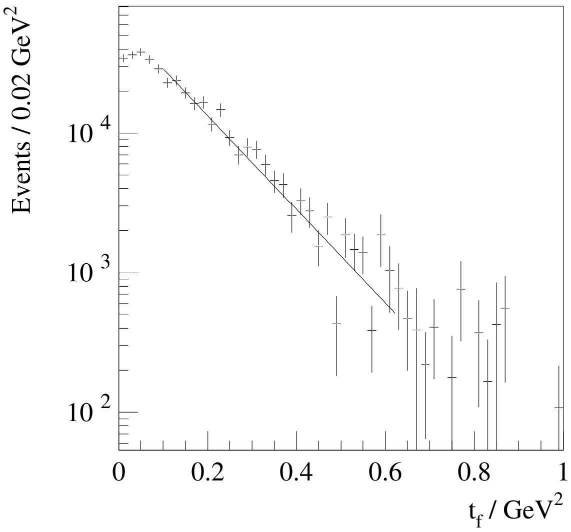

(b) RR corrected data t_f

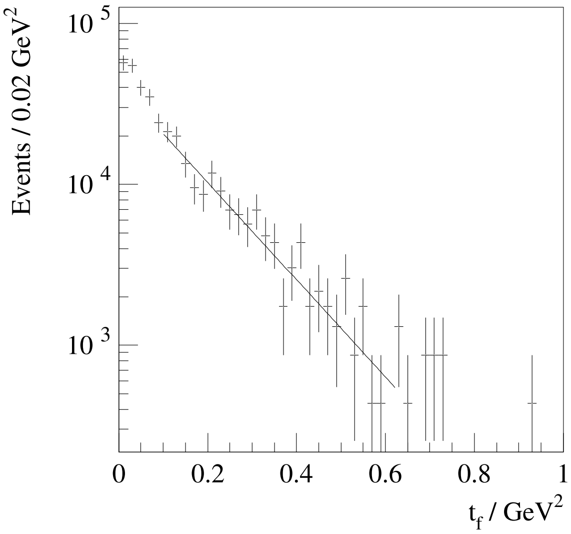

(c) RL corrected data t_f

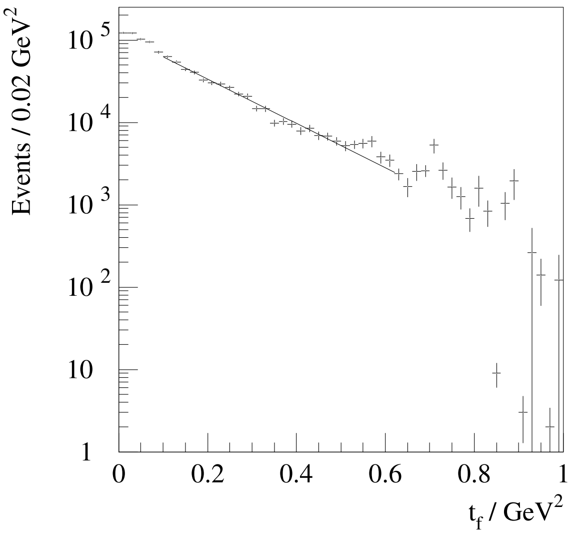

(d) LR corrected data t_f

Figure 7.18: t_f distributions for the corrected data.

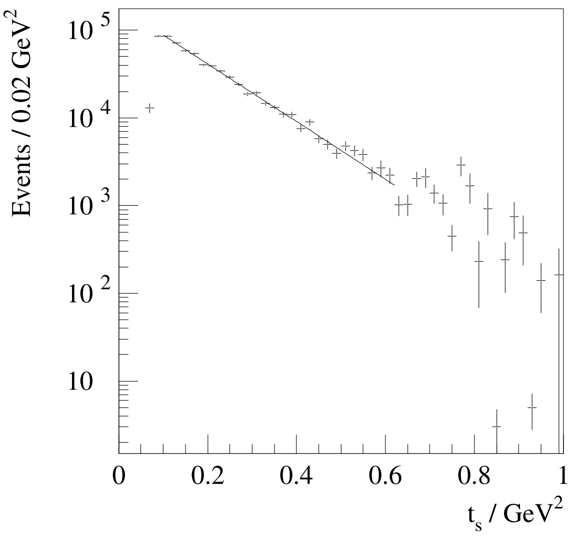

(a) LL corrected data t_s

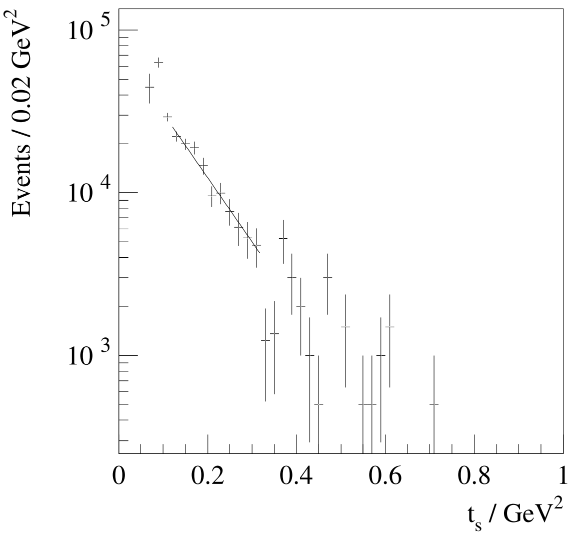

(b) RR corrected data t_s

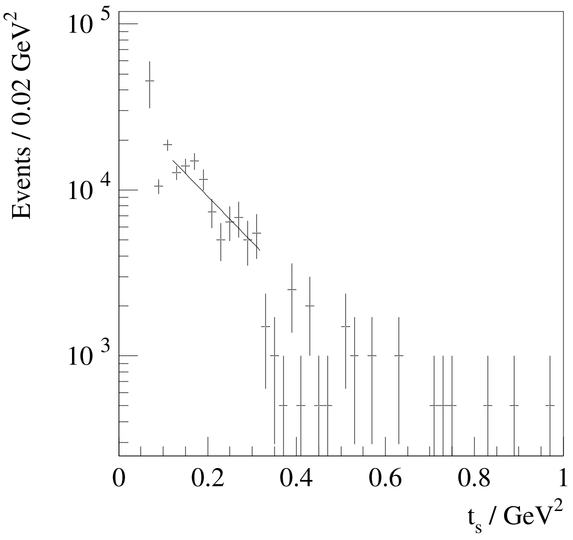

(c) RL corrected data t_s

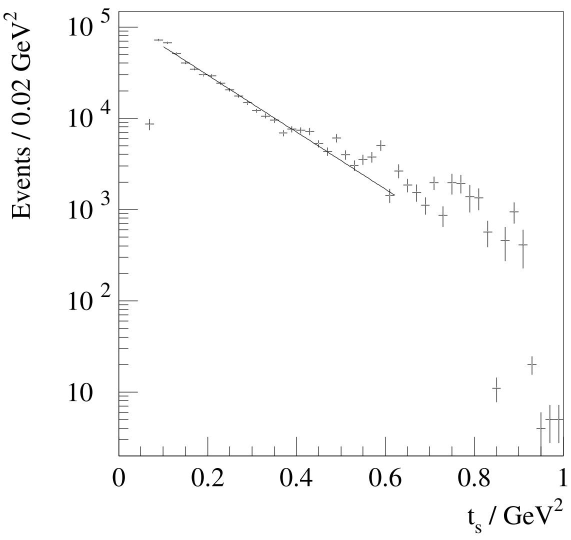

(d) LR corrected data t_s

Figure 7.19: t_s distributions for the corrected data.

Table 7.4: Values of the slope parameter α for RR and RL in the corrected data.

Trigger	α / GeV^{-2}
RR fast	-7.7 ± 0.2
RR slow	-9.0 ± 0.7
RL fast	-6.9 ± 0.5
RL slow	-6.0 ± 1.0

Table 7.5: Values of the slope parameter α for LL and LR in the $f_2(1270)$ mass region.

Trigger	α / GeV^{-2}
LL fast	-6.0 ± 0.2
LL slow	-6.0 ± 0.2
LR fast	-5.4 ± 0.2
LR slow	-5.6 ± 0.2

has the disadvantage that it does not provide "goodness-of-fit" information, as may be obtained from a minimum χ^2 fit. The quality of the fit may in part be estimated by an examination of the plots, where it is observed that the data and the fit are very similar over the t range being fitted. In fact, χ^2 fits have also been performed, which gave very similar results with reasonable fit qualities.

Fits to the RR and RL data give the results shown in table 7.4. Since the uncorrected data are poor in the region $|t| > 0.3$ GeV^2 for the RR and RL slow slopes, values of $|t|$ above this value are not fitted in the corrected slopes. It may be seen that both the RR slopes and both the RL slopes are in reasonable agreement with the equivalent slopes for LL and LR respectively, although the errors are relatively large, particularly for the slow slopes.

The same analysis for LL and LR triggers has been performed in the mass region $1.1 \leq m_{\pi^+\pi^-} < 1.4$ GeV/c^2, corresponding to the mass around the $f_2(1270)$. This gives the acceptance corrected slopes for LL and LR shown in table 7.5. The data are compared with the same slopes in the $\rho(770)$ mass region discussed above in figure 7.20 [78]. Some variation of the $|t|$ slopes with mass is observed, since the slopes in the $f_2(1270)$ mass region are rather shallower than those in the $\rho^0(770)$ mass region.

7.5 Comparison With Other Channels

Shown in figure 7.21 are mass spectra for K^+K^- and $\pi^+\pi^-\pi^+\pi^-$ taken during the same run of WA91 [78]. The K^+K^- mass spectra are shown in figures 7.21 *a* and *b*. The $f_2'(1525)$ is a well known $q\overline{q}$ state, and is seen with a considerably stronger signal in the LR case. Interestingly, the $\theta/f_J(1710)$ signal in K^+K^- is dominant in the LL mass spectrum. The $\pi^+\pi^-\pi^+\pi^-$ mass spectra shown in figures 7.21 *c* and *d* show a clear enhancement of the $q\overline{q}$ state $f_1(1285)$ in LR triggers.

7.6 Comparison With Other Experiments

The SFM Collaboration also observed that the directions taken by the outgoing fastest and slowest particles in central interactions are correlated with the centrally produced states [79]. They studied the central $\pi^+\pi^-$ channel at an energy of $\sqrt{s} = 62$ GeV, and calculated the azimuthal angle ($\Delta\phi$) between the two outgoing protons in the transverse momentum plane in the centre-of-mass, determining the ratio

$$R = (N_G - N_L)/(N_G + N_L),$$

as a function of $m_{\pi^+\pi^-}$, where $N_G(N_L)$ is the number of events with $\Delta\phi$ greater (less) than 90°. This is shown in figure 7.22, together with a model which does not suppose there is any correlation between the resonances produced and $\Delta\phi$. At this energy, there is no evidence for $\rho^0(770)$ production, but the SFM Collaboration observed an enhancement of $f_2(1270)$ production in the $\pi^+\pi^-$ channel in cases where the fastest and slowest particles in the laboratory frame have a "back-to-back"

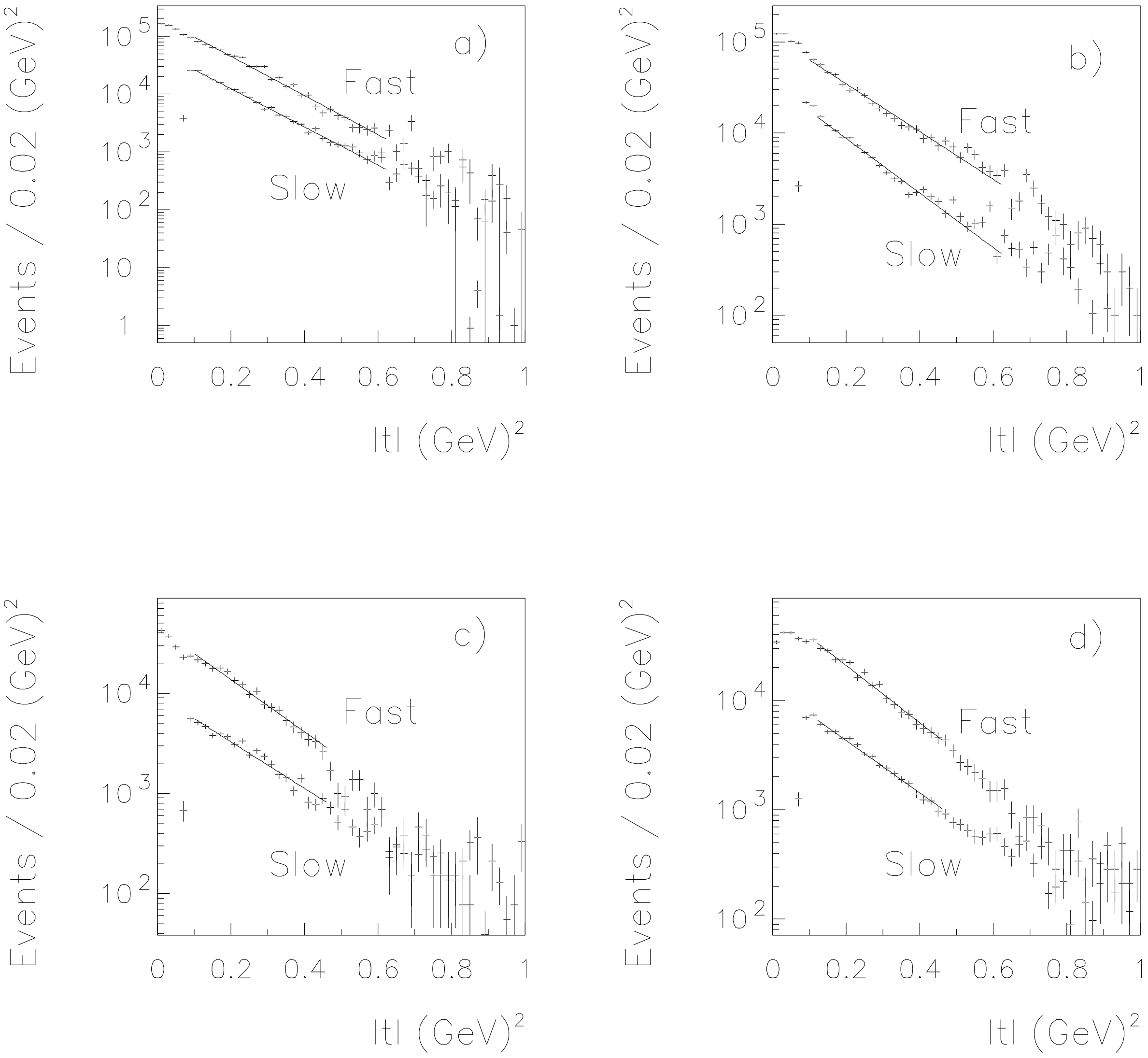

Figure 7.20: Acceptance corrected $|t_f|$ and $|t_s|$ distributions for a) LL and b) LR in the $\rho^0(770)$ mass region, and c) LL and d) LR for the $f_2(1270)$ mass region. The $|t_s|$ distributions have been scaled down for comparison with the $|t_f|$ distributions (from [78]).

configuration of their momenta. This is consistent with the enhancement of $f_2(1270)$ production in the WA91 data in LR and RL triggers, but using a more complex model of DPE involving two-gluon exchange, the SFM Collaboration concluded that this may suggest that the $f_2(1270)$ has a large glueball content. This does not seem consistent with the WA91 observation that there is also an enhancement of the $\rho^0(770)$ signal in LR and RL triggers at $\sqrt{s} = 28$ GeV, since the $\rho^0(770)$ is well understood as having a quark-like rather than a glueball nature.

7.7 Conclusions

It has been shown that for the centrally produced $\pi^+\pi^-$ system, there is a strong correlation between the resonances produced and the azimuthal angle between the outgoing protons. Specifically, more $\rho(770)$ and $f_2(1270)$ production is seen in the LR and RL triggers (where the outgoing protons are "back-to-back" in the p_T plane) than in the LL and RR triggers. This is not attributable to trigger or acceptance effects. In the K^+K^- channel, a significant enhancement is seen in the amount of $f_2'(1525)$ production in the LR and RL triggers, but the $\theta/f_J(1710)$ is seen predominantly in the LL and RR triggers. In the $\pi^+\pi^-\pi^+\pi^-$ channel, the $f_1(1285)$ is seen to be enhanced in the LR and RL channels.

These observations would not be expected in simple models of DPE, and lead to the conclusion that different exchange mechanisms contribute to different trigger types. This suggests that the exchange vertices may not factorize simply, although further work is needed to establish the origin of this effect.

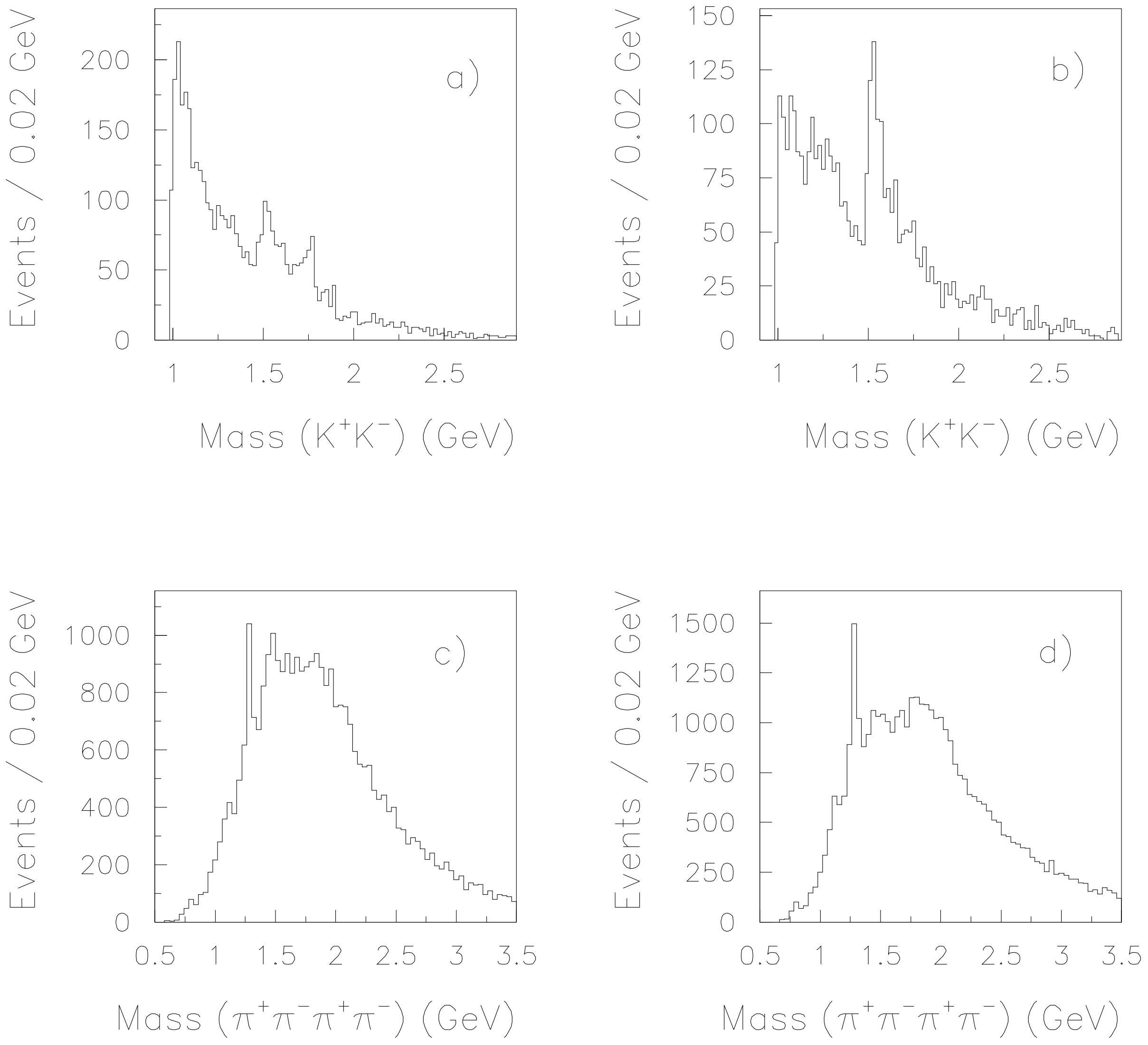

Figure 7.21: Mass spectra for a) K^+K^- LL, b) K^+K^- LR, c) $\pi^+\pi^-\pi^+\pi^-$ LL and d) $\pi^+\pi^-\pi^+\pi^-$ LR (from [78]).

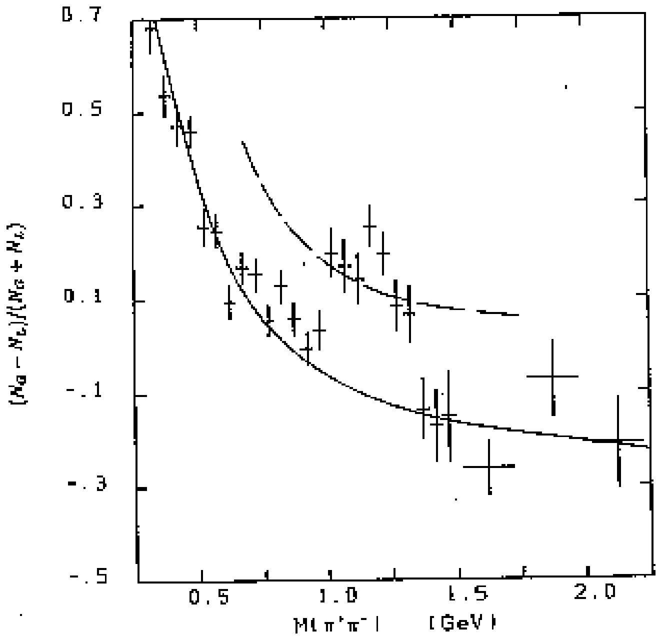

Figure 7.22: Distribution of $R = (N_G - N_L)/(N_G + N_L)$ as a function of $m_{\pi^+\pi^-}$. The solid curve shows the prediction of a standard DPE model, the dashed curve is the result of a simulation of two-gluon exchange from a simple kinematical model (from [79]).

Chapter 8

Conclusions

Quantum Chromodynamics predicts the existence of a hadronic spectrum beyond that composed of $q\overline{q}$ and qqq states. Such "new" states are predicted to have characteristics that may make them possible to observe and identify as incompatible with a $q\overline{q}$ or qqq classification. There are several reaction mechanisms which are thought to be "glue-rich," and recent evidence suggests that the lowest-lying gg state may have been observed in such processes, with a mass of $\sim$ 1500 MeV/c^2 and a width of $\sim$ 200 MeV/c^2.

A detailed analysis of the centrally produced $\pi^+\pi^-$ system using data taken by the WA91 Collaboration during 1992 and 1994 at a beam momentum of 450 GeV/c has been presented. In a fit to the mass spectrum, it has been shown that using a formalism which fits resonances parameterized by Breit-Wigner shapes and an interfering S-wave background, a state at around 1500 MeV/c^2 with a width of $\sim$ 200 MeV/c^2 must be included. A method of parameterizing the angular distribution has been developed, which allows us to perform a fit to the moments of the reaction and extract the partial waves. A fit using the same formalism as that used for the total mass spectrum also finds it necessary to include the state at 1500 MeV/c^2. A fit to the poles of a parameterization of the K matrix using only a background and interfering $f_0(980)$ term cannot reproduce the physical S-matrix poles of the $f_0(980)$, suggesting that further poles (possibly corresponding to the $f_0(1500)$) need to be added in this formalism.

A detailed study of resonance production as a function of trigger type has also been presented. An interesting effect has been observed, namely that the exchange mechanism is correlated with the trigger type, suggesting that the exchange vertices cannot be factorized. This is not expected in simple models of DPE.

8.1 Suggestions For Further Study

With regard to the status of the $f_0(1500)$, it would certainly be interesting to fit the WA91 data together with data from other central production experiments and $\pi\pi$ scattering. This would allow a fully unitarized model to be used in the fitting procedure, and may help in deciding what the contribution of the $f_0(1500)$ to the $\pi^+\pi^-$ channel is. Since there is evidence that this state may be associated with the lowest lying glueball, it is important to refine the current understanding of its properties. Furthermore, in the Amsler-Close picture [45], if this state is the lowest scalar glueball, there should be another scalar state at around 1700 MeV/c^2. In the K^+K^- channel of WA91 data, a state at around this mass is clearly seen, which has been identified as the $f_J(1710)$, and it would be enlightening to perform a partial wave analysis of this channel to find the quantum numbers of this state. This can now be done using the PWA formalism and fitting procedure developed in the present work.

It has been shown that the trigger type effect discussed in chapter 7 is not attributable to the trigger or to experimental acceptance, and hence is presumably due to a physical effect. However, there is no clear idea of the its cause, and it is necessary to develop an explanation of this effect. The suggestion that the exchange vertices do not factorize has implications for all "central production-like" experiments.

Sadly, the advent of the LHC has led to the demise of the LEAR and SPS programmes at CERN, and the immediate future for hadron spectroscopy appears rather bleak. This is indeed unfortunate, since in this thesis evidence has been presented that non-perturbative QCD and the nature of parton confinement is far from being well understood. There has been some discussion concerning the setting up of a new CERN hadron spectroscopy experiment (see, *e.g.*, [80]), but the status of this at the time of writing is still subject to funding. Facilities at KEK, SLAC, Beijing and IHEP may become increasingly important in this field.

However, for the time being, there is still much analysis work to be done. The final run of the WA102 experiment has recently been completed, having taken data over a four month period in 1996, and it is to be hoped that this data, along with further analysis coming from LEAR and other experiments, will help to clarify the situation.

Appendix A

Useful Formulæ

A.1 Interaction Length

Consider a target with cross-sectional area A_t, length Δl and density ρ. If the flux per unit area of beam particles is n_b per second, then the number of interactions per second, n_i, will be

$$n_i = \frac{n_b n_n A_n}{A_t},$$

where n_n is the number of nuclei in the target and A_n is the cross sectional area of one nucleus. Then

$$n_i = \frac{n_b (N_0/A) m_t \sigma_T}{A_t},$$

where N_0 is Avogadro's Number, A is the atomic weight and σ_T is the total cross-section for interaction. This gives

$$n_i = \frac{n_b N_0 \rho \Delta l \sigma_T}{A},$$

or the change in n_b, Δn_b, in a small length, Δl, is

$$\Delta n_b = -\frac{n_b N_0 \rho \Delta l \sigma_T}{A}.$$

Defining

$$L = \frac{A}{N_0 \rho \sigma_T},$$

then as $\Delta n_b \to dn_b$, $\Delta l \to dl$,

$$\int \frac{dn_b}{n_b} = -\int \frac{dl}{L},$$

which has the solution

$$n_b = n_{b_0} e^{-l/L}.$$

For the hydrogen target used by WA91, $l/L \sim 15\%$.

A.2 Ehrlich Mass

Consider the diagram shown in figure A.1.

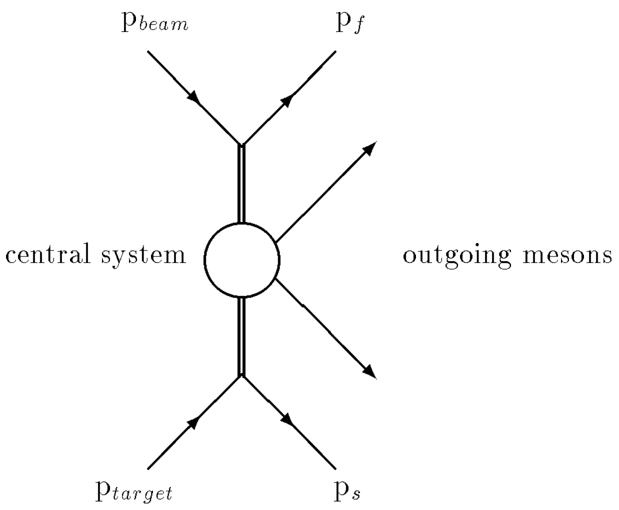

Figure A.1: The central production mechanism in the centre-of-mass frame

The Ehrlich Mass Squared [53] for this reaction is defined in the following way. Let E_b, E_t, E_f, E_s, E_+ and E_- refer to the energies of the beam, target, fast, slow, positive central and negative central particles respectively, and p_b, p_t, p_f, p_s, p_+ and p_- refer to their respective momenta. Then by conservation of energy,

$$E_b + m_{\mathrm{p}} = E_f + E_s + E_+ + E_-,$$

where m_{p} refers to the mass of the proton. Therefore,

$$\begin{aligned}(E_b - E_f - E_s + m_{\mathrm{p}})^2 &= (E_+ + E_-)^2 \\ &= E_+^2 + E_-^2 + 2E_+E_- \\ &= m_+^2 + p_+^2 + m_-^2 + p_-^2 + 2(m_+^2 m_-^2 + m_+^2 p_-^2 + m_-^2 p_+^2 + p_+^2 p_-^2)^{\frac{1}{2}}.\end{aligned}$$

Now $m_+ = m_- = m$, and hence

$$(E_b - E_f - E_s + m_{\mathrm{p}})^2 = 2m^2 + p_+^2 + p_-^2 + 2(m^4 + m^2(p_-^2 + p_+^2) + p_+^2 p_-^2)^{\frac{1}{2}}.$$

Then

$$[(E_b - E_f - E_s + m_{\mathrm{p}})^2 - p_+^2 - p_-^2]^2 = 4[m^4 + 2m^2(m^4 + m^2(p_-^2 + p_+^2) + p_+^2 p_-^2)^{\frac{1}{2}} + m^4 + m^2(p_-^2 + p_+^2) + p_+^2 p_-^2)],$$

and hence

$$[(E_b - E_f - E_s + m_{\mathrm{p}})^2 - p_+^2 - p_-^2]^2 - [2p_+p_-]^2 = 4m^2[2m^2 + 2(m^4 + m^2(p_-^2 + p_+^2) + p_+^2 p_-^2)^{\frac{1}{2}} + p_+^2 + p_-^2)].$$

Using

$$(E_+ + E_-)^2 = 2m^2 + p_+^2 + p_-^2 + 2(p_+^2 p_-^2 + m^2(p_+^2 + p_-^2) + m^4)^{\frac{1}{2}},$$

gives

$$
\begin{aligned}
[(E_b - E_f - E_s + m_{\mathrm{p}})^2 - p_+^2 - p_-^2]^2 - [2p_+p_-]^2 &= 4m^2(E_+ + E_-)^2 \\
&= 4m^2(E_b - E_f - E_s)^2,
\end{aligned}
$$

and therefore

$$
m^2 = \frac{[(E_b - E_f - E_s)^2 - p_+^2 - p_-^2]^2 - [2p_+p_-]^2}{4[E_b - E_f - E_s]^2}.
$$

A plot of m^2 for all events of the type shown in figure A.1 will thus show peaks at the square of the mass of the central particles, and reactions with different central particles can thus be separated by cutting on these peaks. Using this method results in events with large errors being eliminated, and furthermore allows an estimate of the experimental mass resolution.

Bibliography

[1] R.N. Cahn and G. Goldhaber *The Experimental Foundations of Particle Physics*, Cambridge University Press (1989).

[2] F. Halzen and A.D. Martin, *Quarks and Leptons: An Introductory Course in Modern Particle Physics*, John Wiley and Sons (1984).

[3] D.H. Perkins, *Introduction to High Energy Physics*, Addison–Wesley Publishing Company, Third Edition (1987).

[4] Particle Data Group, Phys. Rev. **D 50** (1994).

[5] T. Barnes, *Theoretical Aspects of Light Meson Spectroscopy* in *Hadron Spectroscopy and the Confinement Problem*, Ed. D.V. Bugg, PlenumPress (1996).

[6] D. Weingarten, Nucl. Phys. **B34** (Proc. Supp.) (1994) 29.

[7] G. Bali et al., Phys. Lett. **B309** (1993) 378.

[8] *Proceedings of the 6th International Conference on Hadron Spectroscopy* Ed. M.C. Birse, G.D. Lafferty and J.A. McGovern, World Scientific Publishing Co. Pte. Ltd. (1996).

[9] A. Palano, *The Search For Gluonic Matter*, **CERN-EP/87-92** (1987).

[10] S. Okuba, Phys. Lett. **5** (1963) 165;

G. Zweig, **CERN-TH/401, 402, 412** (1964);

J. Iizuka, Prog. Theor. Phys. Suppl. **37–38** (1966) 21.

[11] M.A. Faessler, *The Crystal Barrel Spectrometer* in *Proceedings of the 6th International Conference on Hadron Spectroscopy* Ed. M.C. Birse, G.D. Lafferty and J.A. McGovern, World Scientific Publishing Co. Pte. Ltd. (1996).

[12] H. Muirhead, *Notes on Elementary Particle Physics*, Pergamom Press Ltd., Oxford (1971).

[13] P.D.B. Collins and A.D. Martin *Hadron Interactions,* Adam Hilger Ltd. (1984).

[14] A. Donnachie and P. Landshoff, Phys. Lett. **B296**(1992) 297.

[15] A. Brandt et al., Phys. Lett. **B211** (1988) 239.

A. Brandt et al., Phys. Lett. **B297** (1992) 417.

[16] T. Greenshaw, *Pomeron Structure* in *Proceedings of the 6th International Conference on Hadron Spectroscopy* Ed. M.C. Birse, G.D. Lafferty and J.A. McGovern, World Scientific Publishing Co. Pte. Ltd. (1996).

[17] P.R. Newman, *A Study of the Dynamics of Diffractive Photoproduction at HERA*, PhD Thesis, Birmingham (1996).

[18] T. Ahmed et al., Phys. Lett. **B348** (1995) 681.

[19] G. Ingelman and P.E. Schlein, Phys. Lett. **B152** (1985) 256.

[20] S.N. Ganguli and D.P. Roy, Phys. Rep. **67** (1980) 203.

[21] T.A. Armstrong et al., Phys. Lett. **B228** (1989) 536.

[22] A. Kirk, private communication.

[23] M.R. Pennington, *Hadron '95 - Summary : Part 1* in *Proceedings of the 6th International Conference on Hadron Spectroscopy* Ed. M.C. Birse, G.D. Lafferty and J.A. McGovern, World Scientific Publishing Co. Pte. Ltd. (1996).

[24] D. Aston et al., Nucl. Phys. **B 296** (1988) 493.

[25] T.A. Armstrong et al., Z. Phys. **C 52** (1991) 389.

[26] C. Amsler et al., Phys. Lett. **B 291** (1992) 347.

[27] J. Weinstein and N. Isgur, Phys. Rev. **D41** (1990) 2236.

[28] S. Resag, in *Proceedings of the 6th International Conference on Hadron Spectroscopy* Ed. M.C. Birse, G.D. Lafferty and J.A. McGovern, World Scientific Publishing Co. Pte. Ltd. (1996).

[29] D. Morgan and M. Pennington, Phys. Rep. **D48** (1993) 1185.

[30] D.V. Bugg, A.V. Sarantsev and B.S. Zou, Nucl. Phys. **B471** (1996) 59.

[31] V.V. Anisovich et al., Phys. Lett. **B323** (1994) 233.

[32] C. Amsler et al., Phys. Lett. **B291** (1992) 347.

[33] C. Amsler et al., Phys. Lett. **B340** (1995) 259.

[34] C. Amsler et al., Phys. Lett. **B333** (1994) 277.

[35] C. Amsler et al., Phys. Lett. **B380** (1996) 453.

[36] T.H. Burnett, *Physics of* 0^{++} *and* 2^{++} *Mesons* in *Hadron Spectroscopy and the Confinement Problem*, Ed. D.V. Bugg, Plenum Press (1996).

[37] D.V. Bugg et al., Phys. Lett. **B353** (1995) 378.

[38] D. Alde at al., Nucl. Phys. **B269** (1986) 485.

[39] M. Boutemeur, *GAMS Experiments and Results* in *Hadron Spectroscopy and the Confinement Problem*, Ed. D.V. Bugg, Plenum Press (1996).

[40] D. Alde et al., Phys. Lett. **B201** (1988) 160.

[41] S. Abatzis et al., Phys. Lett. **B324** (1994) 509.

[42] F. Antinori et al., Phys. Lett. **B353** (1995) 589.

[43] T.A. Armstrong et al., Zeit. Phys. **C51** (1991) 351.

[44] G. Vassiliadis et al., *Hadron '95 - Summary : Part 1* in *Proceedings of the 6th International Conference on Hadron Spectroscopy* Ed. M.C. Birse, G.D. Lafferty and J.A. McGovern, World Scientific Publishing Co. Pte. Ltd. (1996).

[45] C. Amsler and F.E. Close, Phys. Lett. **B353** (1995) 385;
"Is $f_0(1500)$ a Scalar Glueball?" hep-ph/9507326.

[46] L. Gray et al., Phys. Rev. **D27** (1983) 307.

[47] N.A. Törnqvist, Zeit. Phys. **C68** (1995) 647;
N.A. Törnqvist, Phys. Rev. Lett. **49** (1982) 624;
N.A. Törnqvist and M. Roos, "Resurrection of the Sigma Meson", Helsinki Preprint HU-SEFT-R-1995-15.

[48] L.P. Chen et al., *Proc. Hadron '91*, **SLAC PUB 5669** (1991).

[49] D.E. Plane, The West Area Beams, **CERN/SPS/83–22** (1983).

[50] R. Fernow, *Introduction to Experimental Particle Physics*, Cambridge University Press (1986).

[51] C.W. Fabjan, *Detectors for Elementary Particle Physics*, Proc. 1993 European School of High Energy Physics, Zakopane, Poland **CERN-PPE/94-61** (1994).

[52] S. Clewer, *Analysis of the Central $K^0_S K^{\pm}\pi^{\mp}$ System and Determination of the f_1(1285) Branching Ratio at 450 GeV/c*, PhD Thesis, Birmingham (1994).

[53] R. Ehrlich et al., Phys. Rev. Lett. **20** (1968) 686.

[54] J.D. Jackson, Nuov. Cim. **34** (1964) 6692.

[55] S.M. Flatté, Phys. Lett. **B63** (1976) 224.

[56] F. James, MINUIT, CERN Computer Centre Program Library Long Write-Up **D506** (1992).

[57] K.L. Au, D. Morgan and M.R. Pennington, Phys. Rev **D35** (1987) 1633.

[58] L.I. Schiff, *Quantum Mechanics (3rd ed.)*, McGraw-Hill (1968).

[59] S.U. Chung, "Spin Formalisms," CERN Yellow Report,CERN 71-8 (1971).

[60] A. Kirk, K.L. Norman, V. Romanovsky and O. Villalobos Baillie (*to be submitted*).

[61] K. Gottfried and J.D. Jackson, Nuov. Cim. **33** (1964) 309.

[62] W.M. Gibson and B.R. Pollard, "Symmetry Principles in Elementary Particle Physics," Cambridge University Press (1976).

[63] A.R. Edmonds, "Angular Momentum In Quantum Mechanics," Princeton University Press, 3rd Printing with corrections (1974).

[64] M. Jacob and G.C. Wick, Ann. Phys. **7** (1959) 404.

[65] A.D. Martin and C. Nef, Nucl. Phys. **B181** (1981) 61.

[66] P. Estabrooks and A.D. Martin, Nucl. Phys. **B95** (1975) 322.

[67] E. Barrelet, Nuov. Cim. **8A** (1972) 331.

[68] J. Pumplin and F.S. Henvey, Nucl. Phys. **B117** (1976) 377.

[69] F. James, "FOWL - a General Monte-Carlo Phase Space Program," CERN Computer Centre Program Library Long Write-Up **W505** (1977).

[70] R. Brun et al., "HBOOK," CERN Computer Centre Program Library Long Write-Up **Y250** (1994).

[71] P.C. Cecil *A Search for Centrally Produced Glueballs in Proton-Proton Interactions*, PhD Thesis, Cambridge (1994).

[72] S.U. Chung et al., Annalen der Physik **4** (1995) 404.

[73] V.V. Anisovich et al., Phys. Lett. **B355** (1995) 363.

[74] V.V. Anisovich, *Elements of Scattering Theory* in *Hadron Spectroscopy and the Confinement Problem*, Ed. D.V. Bugg, Plenum Press (1996).

[75] T. Ishida et al., *Study of the $\pi^0\pi^0$ System Below 1 GeV Region in the pp Central Collision Reaction at 450 GeV/c* in *Proceedings of the 6th International Conference on Hadron Spectroscopy* Ed. M.C. Birse, G.D. Lafferty and J.A. McGovern, World Scientific Publishing Co. Pte. Ltd. (1996).

[76] D. Morgan and M.R. Pennington, Phys. Rev. **D48** (1993) 1185.

[77] S. Giani et al., "GEANT," CERN Computer Centre Program Library Long Write-Up **Q123** (1996).

[78] D. Barberis et al., *submitted to Phys. Lett.*

[79] A. Breakstone et al., Z. Phys. **C48** (1990) 569.

[80] J.K. Bienlein and A. Kirk, *How Much Hadron Spectroscopy Is Still Needed?* in *Proceedings of the 6th International Conference on Hadron Spectroscopy* Ed. M.C. Birse, G.D. Lafferty and J.A. McGovern, World Scientific Publishing Co. Pte. Ltd. (1996).